Theoretical Study on the Design of Photofunctional Molecular Aggregates and Molecule−Plasmon Systems

January 2021

Takafumi Shiraogawa

The Graduate University for Advanced Studies, SOKENDAI

School of Physical Sciences

Department of Structural Molecular Science

Table of Contents

Chapter 1

General Introduction

In functional molecular science, various studies have been carried out on physical properties resulting from the formation of molecular composite systems and interactions between molecules and inorganic nanostructures. Recently, it is becoming possible to create various composite systems with controlled structures and constituents of molecular aggregates and inorganic nanostructures. In particular, in developments of photofunctional materials, it is important to design the composite systems with desired photofunctions. However, it is not easy to obtain the appropriate design guidelines.

Theoretical and computational chemistry methods are widely used in analysis and prediction of various chemical phenomena with developments of the theories, computational algorithms, computer programs, and computers. The study of complex chemical systems is one of the topics of theoretical and computational chemistry.

This thesis aims to devise design approaches for photofunctional composite systems containing molecules based on the theoretical descriptions. The author has conducted theoretical and computational studies on development of an analysis method of optical properties of photofunctional molecular aggregates and its application to the design. In addition, developments and applications of inverse design methods for photofunctional molecular aggregates and both the molecule−metal nanostructure composite system and incident electric field have been carried out.

Chapter 2 presents the study on the development and application of an analysis method of optical properties of chromophore aggregates. Molecular aggregates composed of organic chromophores have optical properties that differ from those of individual molecules because of intermolecular interactions. In this study, the author developed a

Frenkel exciton decomposition analysis (FEDA) method to analyze absorption, emission, circular dichroism (CD), and circularly polarized luminescence (CPL) of multichromophoric systems and applied it to through-space conjugated oligomers. This method is used for the decomposition analysis of the optical spectra of a multichromophoric system into the constituent chromophore contributions. In the FEDA, the absorption and emission spectra can be decomposed into the molecular intrinsic contributions from each molecule and interactions between the electric transition dipole moments of the molecules. The CD and CPL spectra can be decomposed into the components related to the rotational strength of each dye molecule and interactions of the electric−magnetic and electric−electric transition dipole moments between the molecules. The FEDA method was applied to the through-space conjugated oligomers, and it was found that the absorption and emission mainly originate from the individual chromophores. On the other hand, in the CD and CPL, the author demonstrated that the interactions between the electric transition dipole moments of the adjacent chromophores are crucial, while the interactions between the electric and magnetic transition dipole moments are not negligible.

Chapter 3 presents a strategy for obtaining modification guidelines of optical properties of multichromophoric systems with respect to the constituent molecules based on the analysis. Recent advances in experimental techniques have enhanced a degree of freedom in the design of polymer and supramolecular systems. In particular, since optical properties drastically change depending on the composition and structure, various photofunctional molecular aggregates have been synthesized, where the design guidelines

are demanded for developing efficient optical materials. In this study, the author proposed a post-modification strategy for emission and CPL of multichromophoric systems by using the FEDA method. The FEDA method was applied to an achiral molecular crystal which has the cross-stacked structure of chromophores and exhibits strong luminescence. Generation and annihilation mechanisms of the emission and CPL were analyzed, respectively. The emission is predominantly caused by a local electronic transition of a single chromophore due to the weak exciton coupling. The decomposed CPL components with the strong intensities originate from the interactions of electric transition dipole moments between the chromophore and its adjacent monomers, which cancel out each other in enantiomeric pairs of the achiral system. Based on these findings, the author proposed guidelines toward the improvement in the photofunctions based on the control of molecular species and molecular orientation of the constituent molecules of the system.

Chapter 4 presents the study on the inverse design of photofunctional molecular aggregates and the design of one-dimensional molecular aggregates with strong optical absorption and CD. In contrast to the direct design which is based on the knowledge and findings of existing molecular systems, the inverse design proposes functional molecules from the predefined properties. Here, the author proposed a theoretical design approach for photofunctional molecular aggregates using an inverse design framework, the linear combination of atomic potentials (LCAP). The Frenkel exciton model coupled with the LCAP is introduced for designing systems with desired optical properties by gradient-guided optimization searches in terms of constituent molecules in chemical space of molecular aggregates. The author has applied this approach to design one-dimensional

molecular aggregates having locally maximized absorption and/or CD intensities as an example. By exploring a small fraction of the vast chemical space of 10^{26} possible systems varying in composition and structure, the author successfully obtained the optimal aggregates. The optimal structure–photofunction relationships were investigated from the designed systems. The author clarified that the maximum CD of the designed system is nonlinearly enhanced depending on the number of constituent molecules. Furthermore, the author analyzed the optical spectra and revealed that the potential of the photofunctions is sufficiently exploited. The present method is useful to design photofunctional molecular aggregates and accelerate optical material discoveries.

Chapter 5 presents the research on the development and application of the inverse design method of molecule−metal nanostructure composite system and incident field. The interaction between molecule and plasmon generated on the surface of the metal nanostructure through the electromagnetic field irradiation significantly changes the response properties of the molecule. The properties of such molecule−metal nanostructure composite systems are determined by the molecule, metal nanostructure, and incident electromagnetic field. Recently, toward the photochemistry manipulation using plasmonic phenomena, it is becoming possible to control the metal nature and shape of metal nanostructures, molecular species, relative distance and orientation between the molecule and metal object, and intensity and shape of the electromagnetic field. The author proposed an inverse design method for the molecule and incident electric field of the molecule−metal nanostructure composite systems to realize the desired photophysical properties. The design of the molecule is implemented for the molecular species and the

spatial arrangements of the molecule with respect to the nanostructure. The continuous chemical space of the candidate molecule−metal systems is described based on the time-dependent quantum chemical description of the molecule and the continuum model of the metal nanostructure. The inverse design method enables us to find the optimal incident field and molecule near the metal nanostructure with arbitrary metal nature and shape by continuous optimization. This method was applied to the design of the optimal incident electric field and substituents of the organic molecule selectively excited to a target excited state in the proximity of the metal nanostructure. The results of the design of the molecule, incident electric field, and both of them were presented and discussed.

Chapter 6 presents the final remarks of the present studies.

Chapter 2

Frenkel-Exciton Decomposition Analysis of Optical Properties of Multichromophoric Systems

2.1. Introduction

In chiroptical spectroscopy, photophysical properties of chiral molecules such as circular dichroism (CD) has been successfully used to probe their configuration or conformation in the wide field of chemistry and biology. Recently, circularly polarized luminescence (CPL) has attracted much attention because of its potential utility for technological applications.[1] Among various kinds of CPL molecules, multichromophoric systems composed of organic chromophore units have been recognized as one of the most promising candidates because of its high absorption coefficient and quantum yield.[2] In the design or development of the CPL molecules, the control of electronic interactions between the units is important to achieve a high dissymmetry factor,[3] which is a key parameter for the optical chirality.

Molecular exciton theory[4] based on the Frenkel exciton model is an essential concept to interpret the electronic absorption spectrum of a multichromophoric system. This approach is also utilized as exciton chirality method[5] to determine the stereochemistry of chiral molecules through the CD spectrum. It has been generally recognized that these qualitative concepts are useful for interpreting or predicting the chiral photophysical properties of the system. For example, recently, the exciton chirality method was also utilized for the design of the CPL molecules.[6] However, the applicability of these approaches is still unknown for complex multichromophoric systems including several chromophoric units.

Quantum chemical calculations, for example, based on time-dependent density functional theory (TD-DFT), have been widely used for analyzing or predicting electronic

optical properties of the functional molecules. However, for the absorption and CD spectra of multichromophoric systems, the analysis or interpretation of the spectra is not straightforward. Recently, Mennucci and coworkers proposed a method which can suitably reproduce the results of whole systems by the calculations of chromophore units,[7,8] by combining the Frenkel exciton model in the matrix method[9] and a fully ab initio method to compute the exciton coupling.[10,11] The method has been also applied to CPL[12] and used to decompose absorption and CD spectra of nucleic acids into contributions from each unit in terms of the exciton composition.[13] In particular, the characteristics of the CD spectra were explained by a Frenkel-exciton decomposition analysis (FEDA) using a length-form rotatory strength.[13] The rotatory strength has been predominantly described by the electric-electric transition dipole moment interaction ($\mu\mu$), although the electric-magnetic transition dipole moment interaction (μm) was considered later.[8] Indeed, the use of the velocity-form rotatory strength is important to ensure the gauge-invariance of the calculations; moreover, it is still unknown if both the $\mu\mu$ and μm interactions are relevant or not for general applications.

Therefore, in this work, the author performs FEDA on the CD and CPL with the decomposition of $\mu\mu$ and μm interactions into each chromophoric unit using the velocity-form rotatory strength. The author has applied the method to recently developed through-space conjugated oligomers as an example because it achieves a considerable dissymmetry factor.[14] In particular, for CPL, the FEDA method can be used for analyzing the interactions among the chromophore units towards the rational design of CPL molecules. Through the present FEDA, we can understand the physical and structural

nature underlying the CD and CPL spectra of multichromophoric system as well as their absorption and emission spectra. The implemented method is in a framework of the exciton model and has the potential to be extended with the further improvement of the exciton Hamiltonian and its coupling.

2.2. Methods

The present method is based on the excitonic calculation method developed in Refs. [7] and [8]. For the detailed formulation of rotatory strength, the readers are referred to the original articles. Here, the decomposition is extended to the multi-component chromophores with the rotatory strength in the velocity form.

The velocity-form rotatory strength of the electronic transition from the ground state to the *K*th exciton state can be divided into two types of physical interactions as

$$R_{0K} = R_{0K}^{\mu m} + R_{0K}^{\mu\mu} \tag{1}$$

where $R_{0K}^{\mu m}$ and $R_{0K}^{\mu\mu}$ originate from electric−magnetic (μm) and electric−electric transition dipole moment ($\mu\mu$) interactions, respectively.[8] These terms are respectively written as

$$R_{0K}^{\mu m} = \frac{1}{E_K - E_0}\left\{\sum_{i}^{N}\sum_{a}^{n_i}\left(C_{ia}^{K}\right)^2 \varepsilon_{ia} R_{i0a} - \frac{e\hbar^2}{m_e}\mathrm{Im}\left(\sum_{i\neq j}^{N}\sum_{a,b}^{n_i,n_j} C_{ia}^{K}\boldsymbol{\mu}_{i0a}\cdot C_{jb}^{K}\boldsymbol{m}_{jb0}^{\mathrm{int}}\right)\right\}, \tag{2}$$

$$R_{0K}^{\mu\mu} = \frac{e^2\hbar^3}{2cm_e^2\left(E_K - E_0\right)}\sum_{i>j}^{N}\sum_{a,b}^{n_i,n_j}\boldsymbol{R}_{ij}\cdot\left(C_{ia}^{K}\boldsymbol{\mu}_{i0a}\times C_{jb}^{K}\boldsymbol{\mu}_{jb0}\right) \tag{3}$$

where e is the elementary charge, $\hbar$ is the reduced Planck constant, c is the speed

of light, m_e is the mass of an electron, E_K and E_0 are the exciton and the ground state energy, respectively. The indices *i* and *j* mean the different chromophoric units, and *a* and *b* indicate the local excitation of the units. C_{ia}^{K} is an exciton coefficient for the *a*th local excited state of the unit *i*.

In equation (2), ε_{ia} and R_{i0a} are respectively excitation energy and the velocity-form rotatory strength within the unit, whereas the second term is the μm interaction between the units. The first term is essentially relevant for the complexes with chiral units. $\boldsymbol{\mu}_{i0a}$ is the electric transition dipole moment of each unit *i* in the velocity form and written as μ here. $\boldsymbol{m}_{jb0}^{\mathrm{int}}$ is the intrinsic (internal) magnetic transition dipole moment of the unit and written as *m*. Thus, $R_{0K}^{\mu m}$ is composed of the intra and inter unit μm interactions. Notably, the inter-unit term can be non-zero even if the units themselves are not chiral. In equation (3), $R_{0K}^{\mu\mu}$ is composed of the inter-unit $\mu\mu$ interactions. $\boldsymbol{R}_{ij}$ is a distance vector from unit *i* to *j* and expressed as $\boldsymbol{R}_{ij} = \boldsymbol{R}_j - \boldsymbol{R}_i$. In the FEDA of chiroptical spectra, the author respectively defined $\mu_i m_j$ and $\mu_i \mu_j$ as the components of $R_{0K}^{\mu m}$ (μm interaction) and $R_{0K}^{\mu\mu}$ ($\mu\mu$ interaction) for the *i*th and *j*th chromophores. The detailed formulation is shown in the Supporting Information.

For all calculations, the CAM-B3LYP functional[15] was used to avoid underestimation of charge-transfer excitation energy and its artificial problem in simulating the shape of the spectra, in particular the Cotton effect. Ground-state and

excited-state geometries of all the systems were optimized using CAM-B3LYP/6-31G(d). The author confirmed that there is no imaginary frequency at all stable structures. For all the vertical excitation calculations, the 6-31+G(d) basis set was used. Solvent effects were described by the integral equation formalism-polarizable continuum model (IEF-PCM)[16] using $CHCl_3$ as solvent. The author modeled the *n*-$C_{12}H_{25}$ group in Figure 2.1 by hydrogen in all calculations. For the excitonic calculations, the [2.2]paracyclophane was replaced with a benzene dimer for the vertical transitions. The effect of this substitution on the calculations of the spectra was examined for dimer system as shown in Figure 2.S2 and was found to be minor. The ground and excited-state geometries of all systems were determined through optimizations of the full systems. All calculations were performed using the development version of Gaussian program.[17] The excitonic analysis was conducted by an originally developed program combined with the EXcitonic Analysis Tool (EXAT).[18]

2.3. Results and discussion

The author applied the FEDA with the excitonic calculation using quantum exciton coupling to the through-space conjugated dimer and trimer,[14] whose chemical structures are shown in Figure 2.1. It was reported that these oligomers show reasonable quantum yield.[14] These dimer and trimer have a pseudo-C_2 symmetry and the selected decomposition values are shown in the results of FEDA. Here, the author discusses mainly the results on the trimer; the results on the dimer are presented in the Supporting Information.

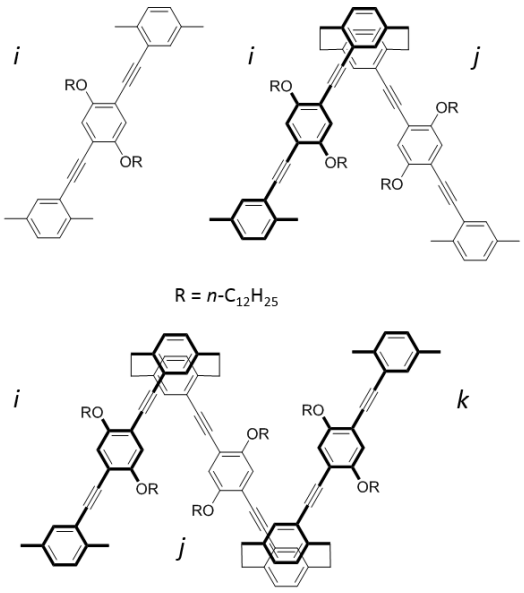

Figure 2.1. Chemical structures of monomer, dimer, and trimer systems of through-space conjugated oligomers investigated in this study. The S_p isomers are shown. The indexes *i*, *j*, and *k* denote the chromophoric units.

The simulated absorption and CD spectra with the full and the excitonic calculations of the trimer model system are shown in Figure 2.2 comparing with experimental spectra. The excitonic calculations suitably reproduced the calculations of the entire system and the experimental results in both absorption and CD spectra, in particular, for the Cotton effects observed at around 370 nm. In the energy region of ~300 nm, the TD-DFT calculations tend to overestimate the transition energy, and there are non-negligible effects of the simplified modeling, in which [2.2]paracyclophane is replaced by benzene dimer (see Figure 2.S2). The middle panel of Figure 2.2(b) displays the decomposition into two types of physical interactions in the CD spectrum. The μμ interaction is dominant in the Cotton effects at around 370 nm. However, μm interaction is not negligible and this

effect in trimer is much larger than that in dimer (see also Figure 2.S3).

The FEDA results for absorption and CD spectra are shown in lower panels of Figure 2.2. The FEDA clearly shows that the absorption peaks at around 370 nm dominantly originate from the local excitation of each chromophore unit, and the contribution from the interaction between the units is minor. On the other hand, the strong Cotton effects at around 370 nm in the CD spectrum are mainly due to the $\mu\mu$ interaction between adjacent units (*i* and *j*), whereas the $\mu\mu$ interaction of the distant units (*i* and *k*) is small. In the μm interaction, the adjacent-unit interaction is a main component, while the interaction between *i* and *k* units and the intra-unit rotatory strength have small contributions. The decomposed μm interactions are also shown in Figure 2.S7. Among the interactions of adjacent units, the $\mu_i m_j$ interaction is larger than the $\mu_j m_i$ interaction where *j* represents the central unit, but both interactions show similar Cotton effects as the $\mu\mu$ interaction at around 370 nm. On the other hand, within the unit, the contribution of R_j is larger than that of R_i and shows a negative Cotton effect at around 370 nm. The electric transition dipole moments of the adjacent *i* and *j* units for the first and third exciton states, where the summation is over excited states of monomer units, are also shown in Figure 2.S10. This interaction between transition moments seen in Figure 2.S10 provides an intuitive interpretation of the nature of CD or Cotton effects and therefore, the present method would be useful for the development of chiral multi-chromophore systems.

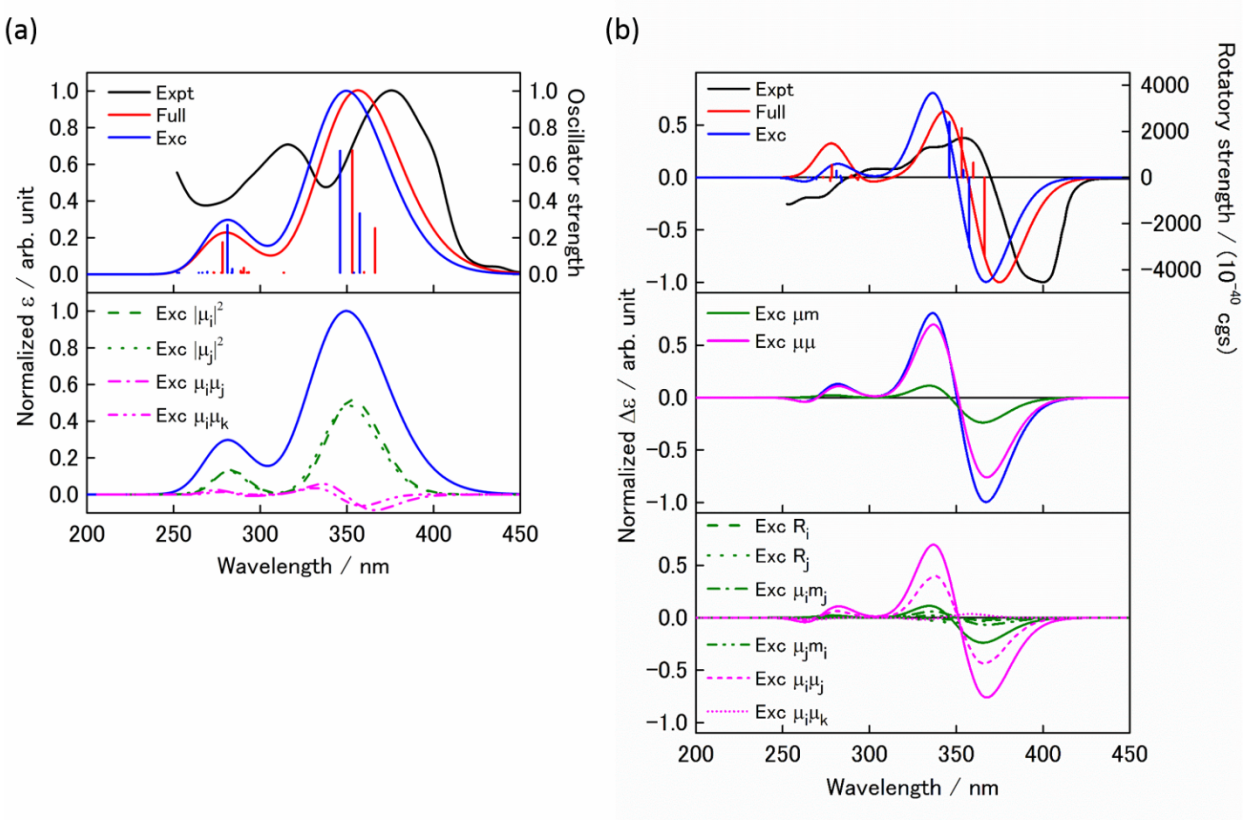

Figure 2.2. Full system and excitonic (a) absorption and (b) CD spectra for through-space conjugated trimer. FEDA results are respectively shown in middle and lower panels of (a) and (b). The experimental spectra were reproduced from Ref. [14].

Figure 2.3 displays the simulated emission and CPL spectra using the full and the excitonic calculations of the trimer model system compared to the experimental spectra. In both cases, the results of the excitonic calculations show good agreement with those of full calculations and experiment. The calculated rotatory strength of CPL is about one-fifth of that of CD obtained at around 370 nm. The physical-interaction decomposition of the CPL spectra is shown in the middle panel of Figure 2.3(b). The $\mu\mu$ interaction is a main component, yet the μm interaction is not negligible. The contribution of μm

interaction in the trimer is larger than that of dimer, as in the CD spectrum (see also Figure 2.S4).

In the lower panels of the same figure, the FEDA results are also shown. The emissive state is more localized on the central unit *j,* owing to geometry relaxation in the excited state. The relevant molecular orbitals at the geometry of the S_1 state for the corresponding transition are shown in Figure 2.S9. In the CPL spectrum, the $\mu\mu$ interaction between the adjacent units is the main component, as in the CD spectrum. In the interaction appearing in CPL, the electric transition dipole strength of the central unit *j* in the exciton state is much larger than that of the terminal units *i* and *k* (see also Figure 2.S10). Thus, the local rotatory strength R_j in the central unit is predominant in the μm interaction. The decomposed μm interactions of CPL are shown in Figure 2.S8. As observed in CD, among the interactions of the adjacent unit, the $\mu_i m_j$ interaction is larger than the $\mu_j m_i$ interaction, and all the contributions are negative.

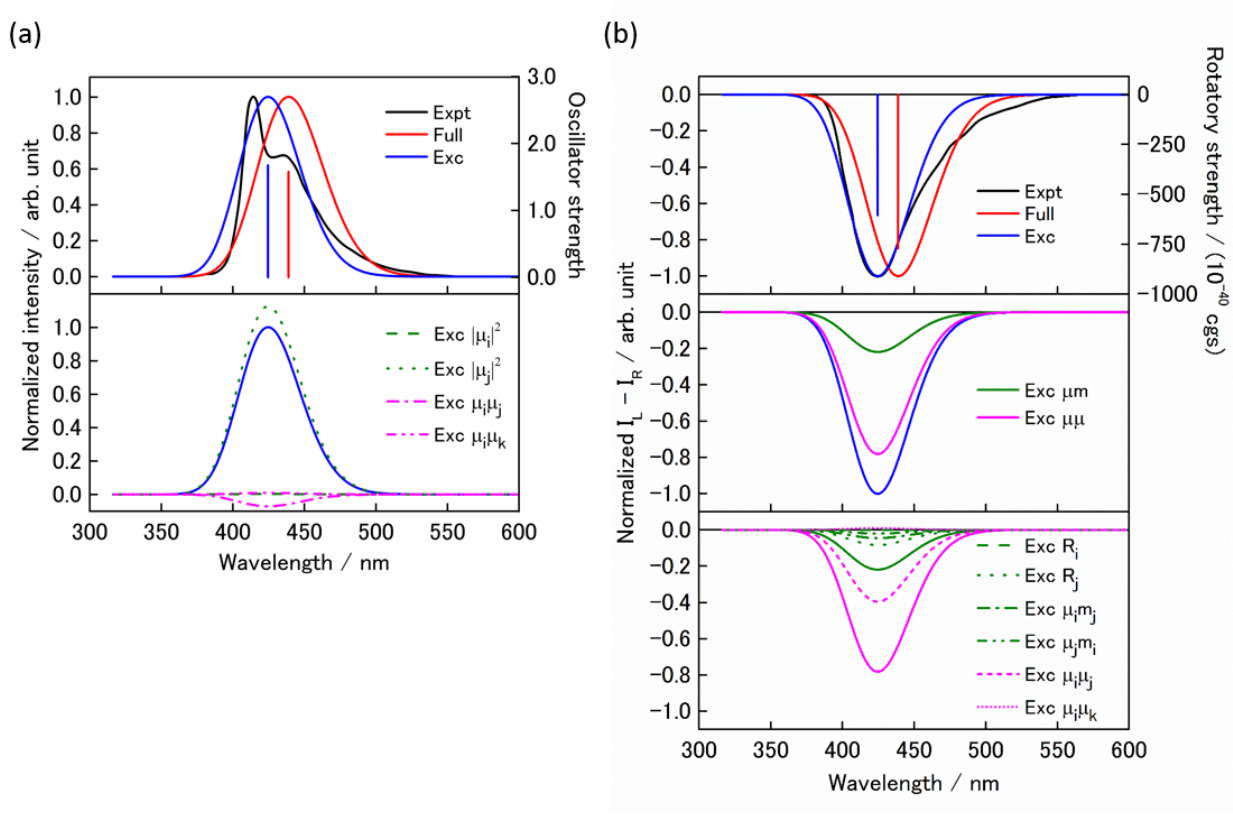

Figure 2.3. Full system and excitonic (a) emission and (b) CPL spectra for through-space conjugated trimer. FEDA results are respectively shown in middle and lower panels of (a) and (b). The experimental spectra were reproduced from Ref. [14].

2.4. Summary

The FEDA method has been utilized for the detailed decomposition of the CD and CPL of multichromophoric system and applied to recently developed through-space conjugated oligomers. This method is based on the velocity-form rotatory strength, and therefore is gauge invariant. The excitonic calculations with quantum exciton coupling suitably reproduced the full calculations of the system and experimental results. It was shown that the interactions between electric transition dipole moments of the adjacent

chromophoric units are crucial in CD and CPL spectra of the multichromophoric systems, nevertheless the interaction between electric and magnetic transition dipole moments is not negligible. The method enables us to evaluate the contribution of the each chromophoric unit to the CD and CPL spectra of the total system, and therefore is a useful tool for aiding the design of functional molecules.

Supporting Information

Frenkel-Exciton Decomposition Analysis (FEDA) Method

The Frenkel-exciton decomposition analysis (FEDA) method enables us to qualitatively evaluate the contributions of the constitution molecules into the optical properties of the molecular aggregate. The author employed this method in Chapters 2–4.

The Frenkel exciton model represents electronic excitations (excitons) of molecular aggregates as a superposition of singly excited states $\left|ia^{\mathrm{agg}}\right\rangle$ of constituent molecules. In the single-excitation manifold, the Frenkel exciton Hamiltonian is

$$\hat{H} = \sum_{i}^{N}\sum_{a}^{n_i} \varepsilon_{ia} \left|ia^{\mathrm{agg}}\right\rangle\left\langle ia^{\mathrm{agg}}\right| + \sum_{i\neq j}^{N}\sum_{a,b}^{n_i,n_j} V_{ia,jb} \left|ia^{\mathrm{agg}}\right\rangle\left\langle jb^{\mathrm{agg}}\right|$$

with

$$\left|ia^{\mathrm{agg}}\right\rangle = \left|ia\right\rangle \prod_{j\neq i}^{N} \left|j0\right\rangle$$

where the molecule *i* is in the *a*th excited state $\left|ia\right\rangle$ and all others in their ground state $\left|j0\right\rangle$. The diagonal term ε_{ia} denotes the *a*th excitation energy of the *i*th molecule. The off-diagonal term $V_{ia,jb}$ is the exciton coupling between the single electronic transitions for the excited states $\left|ia\right\rangle$ and $\left|jb\right\rangle$. In the exciton coupling for the singlet states, the Coulomb term is dominant, and the exchange (–correlation) and overlap terms are usually negligible. The dipole–dipole approximation of the Coulomb term is

$$V_{ia,jb} = \frac{\boldsymbol{\mu}_{i0a} \cdot \boldsymbol{\mu}_{j0b}}{R_{ij}^3} - 3\frac{\left(\boldsymbol{\mu}_{i0a} \cdot \boldsymbol{R}_{ij}\right)\left(\boldsymbol{\mu}_{j0b} \cdot \boldsymbol{R}_{ij}\right)}{R_{ij}^5}$$

where $\boldsymbol{\mu}_{i0a}$ denotes the electric transition dipole moment of the excitation from the ground state $|i0\rangle$ to the excited state $|ia\rangle$ and $\boldsymbol{R}_{ij}$ is the distance vector between the molecules *i* and *j*.

The diagonalization of the Hamiltonian matrix leads to sets of the *K*th exciton state $|K\rangle$ and the corresponding energy E_K. The exciton state is expressed as

$$|K\rangle = \sum_i^N \sum_a^{n_i} C_{ia}^K |ia^{\text{agg}}\rangle$$

where C_{ia}^K is the exciton coefficient for the local exciton state $|ia^{\text{agg}}\rangle$. The ground state is represented as the product of the ground states of the constituent molecules:

$$|0\rangle = \prod_i^N |i0\rangle .$$

The author focuses on the absorption, emission, circular dichroism (CD), and circularly polarized luminescence (CPL) of the molecular aggregates. These photo-activities can be represented by using the photophysical properties of each molecule in the Frenkel exciton model. The length-form electric transition dipole moment $\boldsymbol{\mu}_{i0a}$ and the magnetic transition dipole moment $\boldsymbol{m}_{i0a}$ for the transition *a*←0 of the *i*th molecule are expressed as

$$\begin{aligned} \boldsymbol{\mu}_{i0a} &= \langle i0|\hat{\mu}|ia\rangle \\ &= \langle i0|-e\hat{r}|ia\rangle \end{aligned}’$$

$$\begin{aligned}\boldsymbol{m}_{i0a} &= \langle i0|\hat{m}|ia\rangle \\ &= \frac{ie\hbar}{2m_e c}\langle i0|\hat{r}\times\nabla|ia\rangle\end{aligned}$$

where $\hat{\mu}$ and $\hat{m}$ are the electric and magnetic dipole operators, respectively, $\hat{r}$ is the electron position operator, ∇ is the corresponding differential operator, e is the elementary electric charge, $\hbar$ is the reduced Planck's constant, m_e is mass of the electron, and c is the speed of light. The exciton electric transition dipole moment $\boldsymbol{\mu}_{0K}$ and magnetic transition dipole moment $\boldsymbol{m}_{0K}$ of the excitation from the ground state $|0\rangle$ to the exciton state $|K\rangle$ are represented as

$$\begin{aligned}\boldsymbol{\mu}_{0K} &= \langle 0|\hat{\mu}|K\rangle \\ &= \sum_{i}^{N}\sum_{a}^{n_i} C_{ia}^{K}\boldsymbol{\mu}_{i0a}\end{aligned},$$

$$\begin{aligned}\boldsymbol{m}_{0K} &= \langle 0|\hat{m}|K\rangle \\ &= \sum_{i}^{N}\sum_{a}^{n_i} C_{ia}^{K}\boldsymbol{m}_{i0a}\end{aligned}.$$

The exciton electric and magnetic transition dipole moments are decomposed into the individual molecular components. The CD and CPL are expressed using the rotatory strength. The length-form rotatory strength for the transition K←0 is written as

$$\begin{aligned}R_{0K} &= \mathrm{Im}\left\{\langle 0|\hat{\mu}|K\rangle\cdot\langle K|\hat{m}|0\rangle\right\} \\ &= \mathrm{Im}\left(\boldsymbol{\mu}_{0K}\cdot\boldsymbol{m}_{K0}\right)\end{aligned}.$$

The length-form rotatory strength has a gauge dependence that originates from the magnetic dipole moment. The velocity-form rotatory strength for the exciton states,[3] which is the gauge independent, is expressed as

$$R_{0K} = -\frac{e\hbar^2}{m_e\left(E_K - E_0\right)}\mathrm{Im}\left(\boldsymbol{\nabla}_{0K}\cdot\boldsymbol{m}_{K0}\right)$$

where E_0 is the ground-state energy and $\boldsymbol{\nabla}_{0K}$ is the velocity-form electric transition dipole moment between the ground and exciton states and written as

$$\boldsymbol{\nabla}_{0K} = \sum_{i}^{N}\sum_{a}^{n_i} C_{ia}^{K}\boldsymbol{\nabla}_{i0a}$$

where $\boldsymbol{\nabla}_{i0a}$ is the electric transition dipole moment of the molecule in the velocity form. In this transformation, the equation

$$\boldsymbol{\mu}_{0K} = -\frac{e\hbar^2}{m_e\left(E_K - E_0\right)}\boldsymbol{\nabla}_{0K}$$

is used. This is an exact relation when the complete basis set is used for the calculation.

The intensity of the absorption and emission is proportional to the exciton electric transition dipole moment strength, which is expressed by explicitly writing the contributions of the individual chromophores as

$$\left|\boldsymbol{\mu}_{0K}\right|^2 = \sum_{i}^{N}\sum_{a}^{n_i}\left(C_{ia}^{K}\right)^2\left|\boldsymbol{\mu}_{i0a}\right|^2 + 2\sum_{i>j}^{N}\sum_{a,b}^{n_i,n_j} C_{ia}^{K}\boldsymbol{\mu}_{i0a}\cdot C_{jb}^{K}\boldsymbol{\mu}_{j0b}$$

or

$$\left|\boldsymbol{\nabla}_{0K}\right|^2 = \sum_{i}^{N}\sum_{a}^{n_i}\left(C_{ia}^{K}\right)^2\left|\boldsymbol{\nabla}_{i0a}\right|^2 + 2\sum_{i>j}^{N}\sum_{a,b}^{n_i,n_j} C_{ia}^{K}\boldsymbol{\nabla}_{i0a}\cdot C_{jb}^{K}\boldsymbol{\nabla}_{j0b}$$

where the first term is the molecular intrinsic contributions from each molecule ($|\mu_i|^2$) and the second term is the exciton electric transition dipole moment interactions between the molecules ($\mu_i\mu_j$). The FEDA allows us to analyze dividing the absorption and emission spectra of molecular aggregates into these contributions.

The gauge independence of the velocity-form rotatory strength is shown here. The magnetic dipole operator is written as

$$\hat{m} = \frac{ie\hbar}{2m_e c}\hat{r} \times \nabla .$$

When we change the position of the multichromophoric system ($\hat{r} \to \hat{r} + \hat{R}$), the magnetic transition dipole moment for the exciton state becomes

$$\boldsymbol{m}_{K0}{}' = \boldsymbol{m}_{K0} + \frac{ie\hbar}{2m_e c}\hat{R} \times \nabla_{K0}.$$

The rotatory strength in the new origin is expressed as

$$\begin{aligned} R_{0K}{}' &= -\frac{e\hbar^2}{m_e\left(E_K - E_0\right)}\mathrm{Im}\left(\nabla_{0K} \cdot \boldsymbol{m}_{K0}{}'\right) \\ &= -\frac{e\hbar^2}{m_e\left(E_K - E_0\right)}\mathrm{Im}\left\{\nabla_{0K} \cdot \boldsymbol{m}_{K0} + \frac{ie\hbar}{2m_e c}\nabla_{0K} \cdot \left(\hat{R} \times \nabla_{K0}\right)\right\} \\ &= -\frac{e\hbar^2}{m_e\left(E_K - E_0\right)}\mathrm{Im}\left\{\nabla_{0K} \cdot \boldsymbol{m}_{K0} - \frac{ie\hbar}{2m_e c}\hat{R} \cdot \left(\nabla_{0K} \times \nabla_{K0}\right)\right\} \\ &= R_{0K} \end{aligned}$$

and, therefore it is gauge invariant.

In terms of the origin dependence of the magnetic transition dipole moment, the velocity-form rotatory strength can be decomposed into two types of physical interactions. In practical excitonic calculations of the multichromophoric system, the chromophoric units are calculated in the reference frame of the system, and its schematic image is shown in Figure 2.S1.

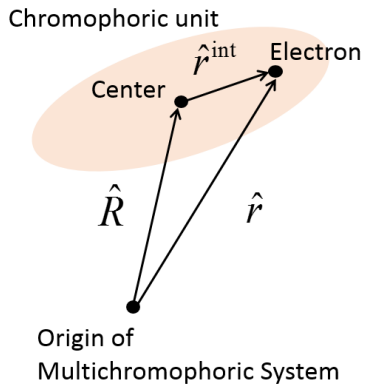

Figure 2.S1. Schematic illustration of the chromophore unit in the reference frame of the multichromophoric system.

The magnetic transition dipole moment can be divided into two parts in terms of the position operator of the electron $\hat{r}$; these terms originate in the intrinsic and extrinsic coordinates of the constituent molecules in the reference molecular aggregate system.[5,7] The magnetic dipole operator $\hat{m}$ is decomposed into the corresponding terms:

$$\begin{aligned}\hat{m} &= \frac{ie\hbar}{2m_e c}\hat{r}\times\nabla \\ &= \frac{ie\hbar}{2m_e c}\left(\hat{r}^{\mathrm{int}}+\hat{R}\right)\times\nabla \\ &= \hat{m}^{\mathrm{int}}+\hat{m}^{\mathrm{ext}}\end{aligned}$$

where the subscriptions “int” and “ext” denote the intrinsic and extrinsic terms, respectively. By using this expression, the magnetic transition dipole moment of the chromophore is decomposed into two terms and written as

$$\boldsymbol{m}_{i0a} = \boldsymbol{m}_{i0a}^{\mathrm{int}} + \boldsymbol{m}_{i0a}^{\mathrm{ext}}$$

where $\boldsymbol{m}_{i0a}^{\mathrm{int}}$ is the intrinsic (internal) magnetic transition dipole moment in the center of

the unit and given as

$$\boldsymbol{m}_{i0a}^{\text{int}} = \frac{ie\hbar}{2m_e c}\left\langle i0\middle|\hat{r}^{\text{int}}\times\nabla\middle|ia\right\rangle.$$

$\boldsymbol{m}_{i0a}^{\text{ext}}$ is the extrinsic term and written as

$$\boldsymbol{m}_{i0a}^{\text{ext}} = \frac{ie\hbar}{2m_e c}\boldsymbol{R}_i\times\nabla_{i0a}$$

where $\boldsymbol{R}_i$ is the barycenter of the *i*th molecule. As a result, the magnetic transition dipole moment for the exciton state is expressed as[7]

$$\begin{aligned}\boldsymbol{m}_{0K} &= \sum_i^N\sum_a^{n_i} C_{i0a}^K\left(\boldsymbol{m}_{i0a}^{\text{int}}+\boldsymbol{m}_{i0a}^{\text{ext}}\right)\\ &= \boldsymbol{m}_{0K}^{\text{int}}+\boldsymbol{m}_{0K}^{\text{ext}}\end{aligned}$$

The substitution of this equation into the equation of the rotatory strength leads to the decomposition of the rotatory strength into two types of physical interactions:

$$R_{0K} = R_{0K}^{\mu m}+R_{0K}^{\mu\mu}$$

where $R_{0K}^{\mu m}$ and $R_{0K}^{\mu\mu}$ in the velocity form can be respectively expressed as

$$\begin{aligned}R_{0K}^{\mu m} &= -\frac{e\hbar^2}{m_e\left(E_K-E_0\right)}\text{Im}\left(\nabla_{0K}\cdot\boldsymbol{m}_{K0}^{\text{int}}\right)\\ &= \frac{1}{E_K-E_0}\left\{\sum_i^N\sum_a^{n_i}\left(C_{ia}^K\right)^2\varepsilon_{ia}R_{i0a}-\frac{e\hbar^2}{m_e}\text{Im}\left(\sum_{i\neq j}^N\sum_{a,b}^{n_i,n_j}C_{ia}^K\nabla_{i0a}\cdot C_{jb}^K\boldsymbol{m}_{jb0}^{\text{int}}\right)\right\},\end{aligned}$$

$$\begin{aligned}R_{0K}^{\mu\mu} &= -\frac{e\hbar^2}{m_e\left(E_K-E_0\right)}\text{Im}\left(\nabla_{0K}\cdot\boldsymbol{m}_{K0}^{\text{ext}}\right)\\ &= \frac{e^2\hbar^3}{2cm_e^2\left(E_K-E_0\right)}\sum_{i>j}^N\sum_{a,b}^{n_i,n_j}\boldsymbol{R}_{ij}\cdot\left(C_{ia}^K\nabla_{i0a}\times C_{jb}^K\nabla_{jb0}\right).\end{aligned}$$

$\boldsymbol{R}_{ij}$ is the distance vector between the mass centers of the molecules *i* and *j*, $\boldsymbol{R}_j-\boldsymbol{R}_i$.

$R_{0K}^{\mu m}$ and $R_{0K}^{\mu\mu}$ have different physical natures which are electric–magnetic and electric–electric transition dipole moment interactions (μm and $\mu\mu$), respectively. $R_{0K}^{\mu m}$ is gauge independent because $\boldsymbol{m}_{ib0}^{\mathrm{int}}$ does not depend on the origin of the multichromophoric system. Therefore, $R_{0K}^{\mu\mu}$ is also gauge independent. The equations of $R_{0K}^{\mu m}$ and $R_{0K}^{\mu\mu}$ mean that the μm and $\mu\mu$ can be decomposed into the photophysical contributions from the molecules: the rotatory strength of the molecules ($\mu_i m_i$ or R_i), electric–magnetic transition dipole moment interactions ($\mu_i m_j$), and electric–electric ransition dipole moment interactions ($\mu_i \mu_j$) between the molecules. As a result, by the FEDA, the CD and CPL spectra are directly analyzed based on the decomposed spectra originating in these contributions of the constituent molecules. Similarly, the length-form rotatory strength can be divided as[7]

$$
\begin{aligned}
R_{0K}^{\mu m} &= \mathrm{Im}\left(\boldsymbol{\mu}_{0K}\cdot\boldsymbol{m}_{K0}^{\mathrm{int}}\right) \\
&= \sum_{i}^{N}\sum_{a}^{n_i}\left(C_{ia}^{K}\right)^2 R_{i0a} + \mathrm{Im}\left\{\sum_{i\neq j}^{N}\sum_{a,b}^{n_i,n_j} C_{ia}^{K}\boldsymbol{\mu}_{i0a}\cdot C_{jb}^{K}\boldsymbol{m}_{jb0}^{\mathrm{int}}\right\}
\end{aligned}
$$

$$
\begin{aligned}
R_{0K}^{\mu\mu} &= \mathrm{Im}\left(\boldsymbol{\mu}_{0K}\cdot\boldsymbol{m}_{K0}^{\mathrm{ext}}\right) \\
&= -\frac{\pi\left(E_K - E_0\right)}{ch}\sum_{i>j}^{N}\sum_{a,b}^{n_i,n_j}\boldsymbol{R}_{ij}\cdot\left(C_{ia}^{K}\boldsymbol{\mu}_{i0a}\times C_{jb}^{K}\boldsymbol{\mu}_{jb0}\right)
\end{aligned}
$$

For the gauge invariance of $R_{0K}^{\mu\mu}$, the excitation energy of the molecule is approximated by that of the molecular aggregate.

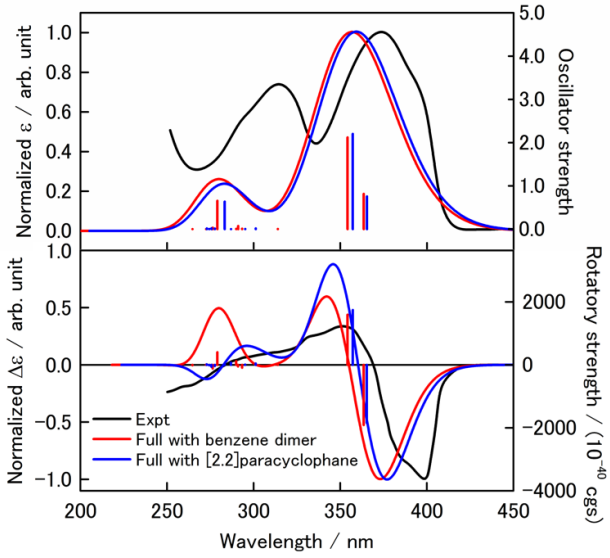

Figure 2.S2. Full system absorption and CD spectra for the through-space conjugated dimer with and without modeling of [2.2]paracyclophane. The experimental spectra were reproduced from Ref. [14].

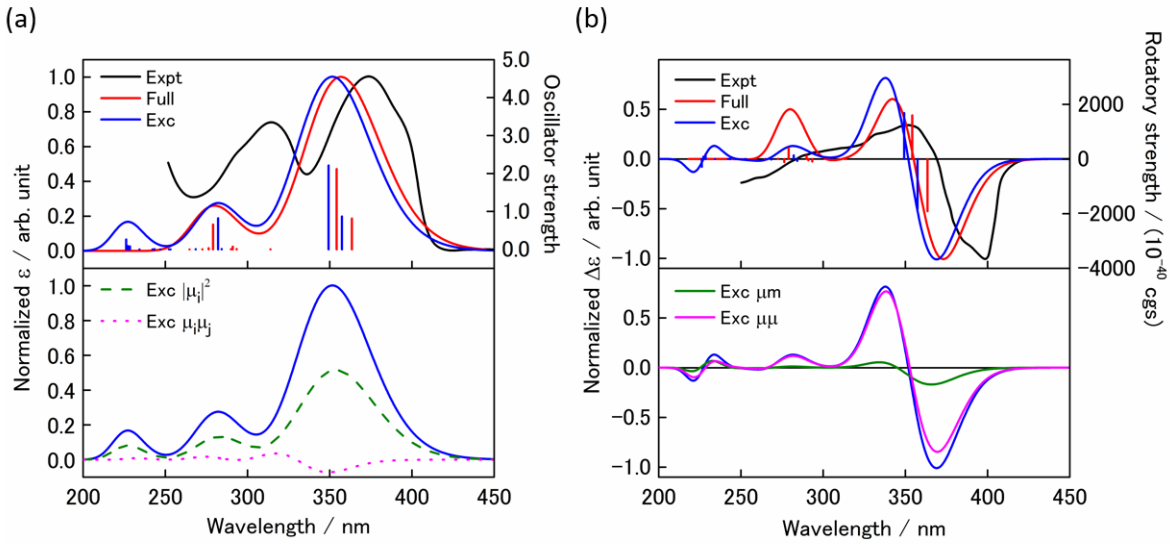

Figure 2.S3. Full system and excitonic (a) absorption and (b) CD spectra for the through-space conjugated dimer. The experimental spectra were reproduced from Ref. [14].

Table 2.S1. Selected vertical excited states of the through-space conjugated dimer

State	VEE (eV)	λ (nm)	f	R (10^{-40} cgs)
Full				
S_1	3.41	364	0.814	–1912
S_2	3.50	354	2.120	1597
Exc				
S_1	3.47	357	0.867	–1821
S_2	3.55	349	2.213	1681

VEE, vertical excitation energy; f, oscillator strength; R, rotatory strength

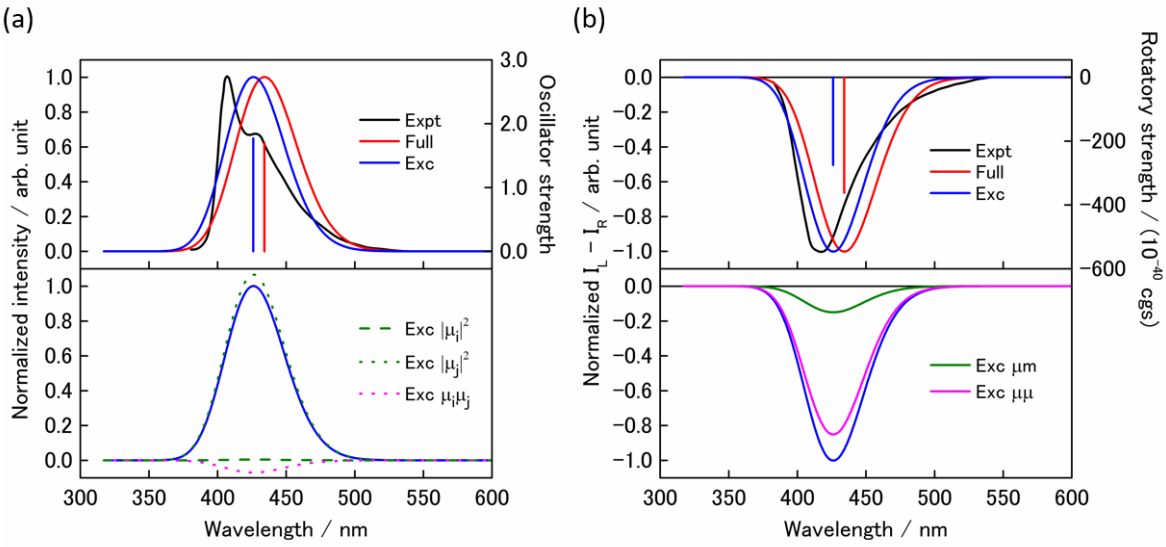

Figure 2.S4. Full system and excitonic (a) emission and (b) CPL spectra for the through-space conjugated dimer. The experimental spectra were reproduced from Ref. [14].

Table 2.S2. The vertical emission of the through-space conjugated dimer

VEE (eV)	λ (nm)	f	R (10^{-40} cgs)
Full			
2.86	434	1.702	–362
Exc			
2.91	426	1.771	–275

VEE, vertical emission energy; f, oscillator strength; R, rotatory strength

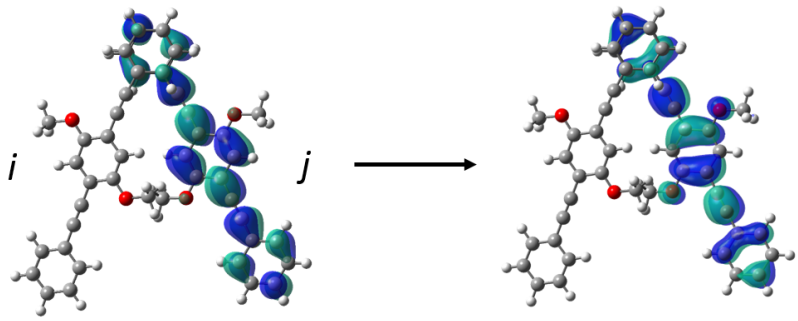

Figure 2.S5. Molecular orbitals of the through-space conjugated dimer in emission and CPL spectra.

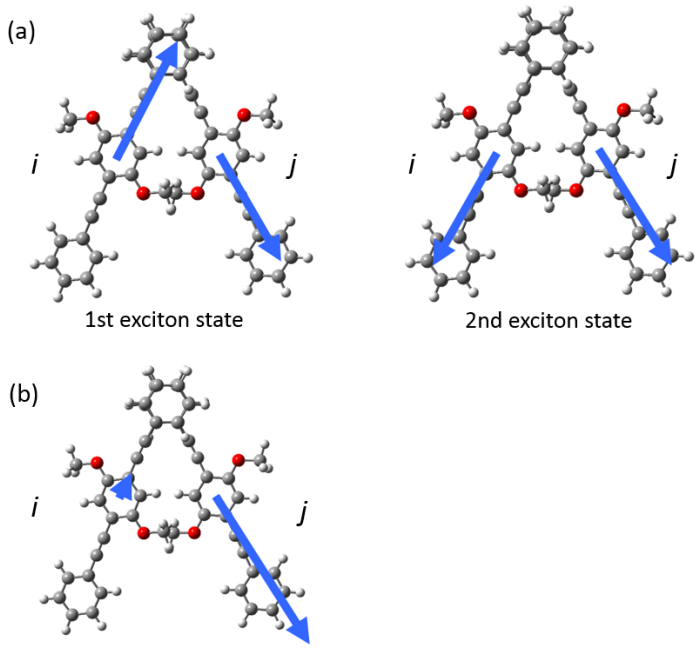

Figure 2.S6. Velocity-form transition dipole moments, where the summation is over excited states of monomer units of the through-space conjugated dimer, in the (a) absorption which involved in the bright exciton states and (b) emission spectra.

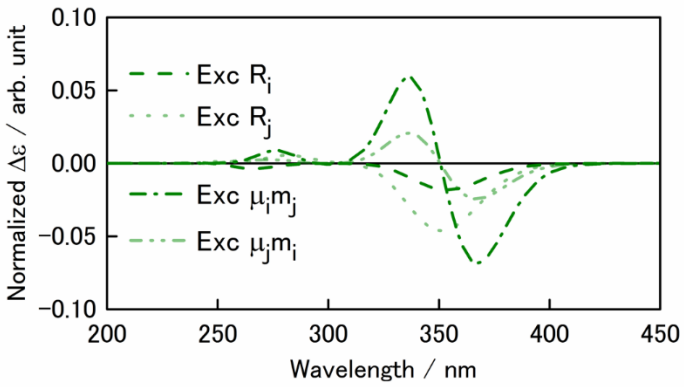

Figure 2.S7. CD spectra of the *μm* interaction for the through-space conjugated trimer.

Table 2.S3. Selected vertical excited states of the through-space conjugated trimer

State	VEE (eV)	λ (nm)	f	R (10^{-40} cgs)
Full				
S_1	3.39	366	1.113	–3388
S_2	3.45	360	0.016	643
S_3	3.51	353	3.056	2126
Exc				
S_1	3.47	357	1.484	–3029
S_2	3.50	354	0.004	324
S_3	3.58	346	3.045	2412

VEE, vertical excitation energy; f, oscillator strength; R, rotatory strength

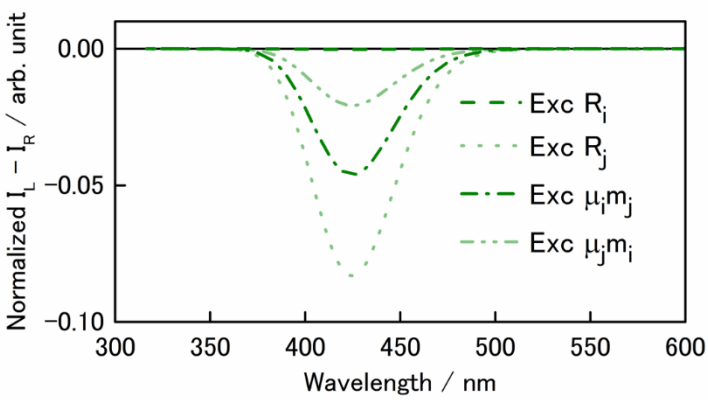

Figure 2.S8. CPL spectra of the μm interaction for the through-space conjugated trimer.

Table 2.S4. The vertical emission state of the through-space conjugated trimer

VEE (eV)	λ (nm)	f	R (10^{-40} cgs)
Full			
2.82	439	1.575	–772
Exc			
2.92	425	1.673	–605

VEE, vertical emission energy; f, oscillator strength; R, rotatory strength

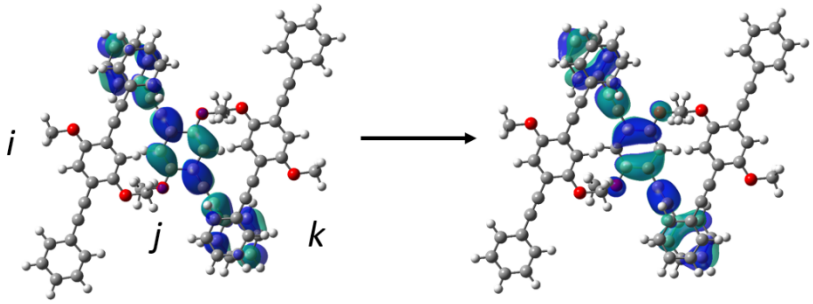

Figure 2.S9. Molecular orbitals of the through-space conjugated trimer in emission and CPL spectra.

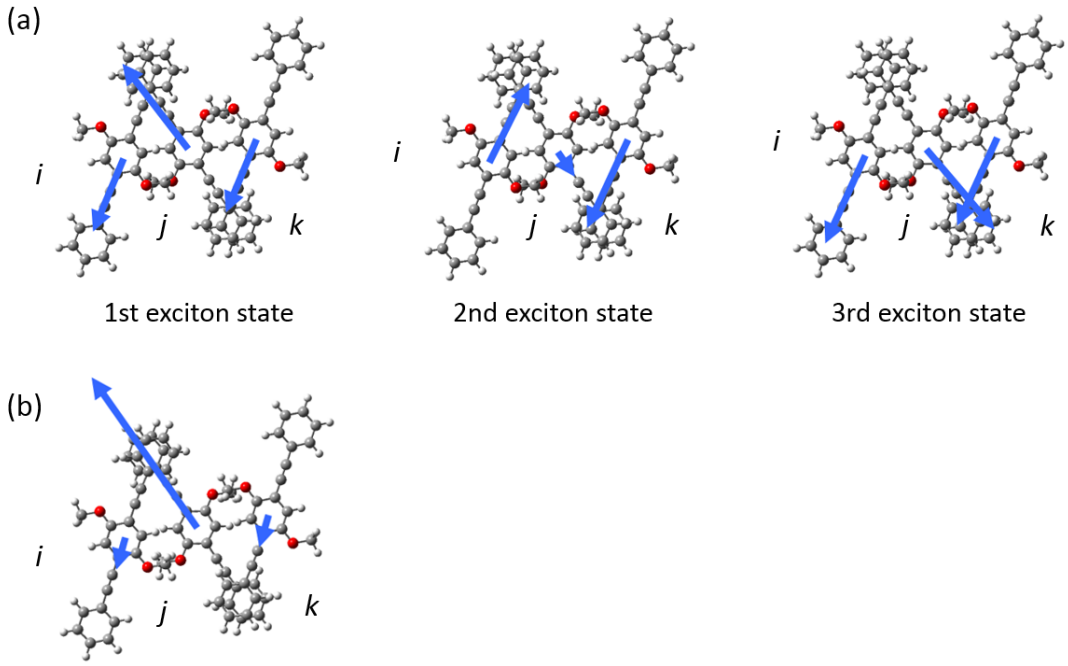

Figure 2.S10. Velocity-form transition dipole moments, where the summation is over excited states of monomer units of the through-space conjugated trimer, in the (a) absorption which involved in the bright exciton states and (b) emission spectra.

References

[1] (a) M. Schadt, *Annu. Rev. Mater. Sci.,* **1997**, *27*, 305–379; (b) J. F. Sherson, H. Krauter, R. K. Olsson, B. Julsgaard, K. Hammerer, I. Cirac, E. S. Polzik, *Nature,* **2006**, *443*, 557–560; (c) C. Wagenknecht, C.-M. Li, A. Reingruber, X.-H. Bao, A. Goebel, Y.-A. Chen, Q. Zhang, K. Chen, J.-W. Pan, *Nat. Photonics,* **2010**, *4*, 549–552; (d) R. Farshchi, M. Ramsteiner, J. Herfort, A. Tahraoui, H. T. Grahn, *Appl. Phys. Lett.,* **2011**, *98*, 162508; (e) H. Tsumatori, T. Harada, J. Yuasa, Y. Hasegawa, T. Kawai, *Appl. Phys. Express,* **2011**, *4*, 011601.

[2] (a) J. Mei, N. L. C. Leung, R. T. K. Kwok, J. W. Y. Lam, B. Z. Tang, *Chem. Rev.,* **2015**, *115*, 11718–11940; (b) K. Watanabe, K. Akagi, *Sci. Technol. Adv. Mater.,* **2014**, *15*, 044203; (c) J. Kumar, T. Nakashima, T. Kawai, *J. Phys. Chem. Lett.,* **2015**, *6*, 3445–3452; (d) E. M. Sánchez-Carnerero, A. R. Agarrabeitia, F. Moreno, B. L. Maroto, G. Muller, M. J. Ortiz, S. de la Moya, *Chem. Eur. J.,* **2015**, *21*, 13488–13500.

[3] C. A. Emeis, L. J. Oosterhoff, *Chem. Phys. Lett.,* **1967**, *1*, 129–132.

[4] M. Kasha, *Radiat. Res.,* **1963**, *20*, 55–71.

[5] N. Harada, K. Nakanishi, Circular Dichroic Spectroscopy - Exciton Coupling in Organic Stereochemistry; University Science Books: Mill Valley, CA, **1983**.

[6] K. Dhbaibi, L. Favereau, M. Srebro-Hooper, M. Jean, N. Vanthuyne, F. Zinna, B. Jamoussi, L. Di Bari, J. Autschbach, J. Crassous, *Chem. Sci.*, **2018**, *9*, 735–742.

[7] S. Jurinovich, G. Pescitelli, L. Di Bari, B. Mennucci, *Phys. Chem. Chem. Phys.*, **2014**, *16*, 16407–16418.

[8] S. Jurinovich, C. A. Guido, T. Bruhn, G. Pescitelli, B. Mennucci, *Chem. Commun.*,

2015, *51*, 10498–10501.

[9] P. M. Bayley, E. B. Nielsen, J. A. Schellman, *J. Phys. Chem.,* **1969**, *73*, 228–243.

[10] C.-P. Hsu, G. R. Fleming, M. Head-Gordon, T. Head-Gordon, *J. Chem. Phys.*, **2001**, *114*, 3065–3072.

[11] M. F. Iozzi, B. Mennucci, J. Tomasi, R. Cammi, *J. Chem. Phys.,* **2004**, *120*, 7029–7040.

[12] F. Zinna, T. Bruhn, C. A. Guido, J. Ahrens, M. Bröring, L. Di Bari, G. Pescitelli, *Chem. Eur. J.,* **2016**, *22*, 16089–16098.

[13] D. Loco, S. Jurinovich, L. D. Bari, B. Mennucci, *Phys. Chem. Chem. Phys.,* **2016**, *18*, 866–877.

[14] Y. Morisaki, K. Inoshita, Y. Chujo, *Chem. Eur. J.,* **2014**, *20*, 8386–8390.

[15] T. Yanai, D. P. Tew, N. C. Handy, *Chem. Phys. Lett.,* **2004**, *393*, 51–57.

[16] B. Mennucci, E. Cancès, J. Tomasi, *J. Phys. Chem. B,* **1997**, *101*, 10506–10517.

[17] M. J. Frisch, G. W. Trucks, H. B. Schlegel, G. E. Scuseria, M. A. Robb, J. R. Cheeseman, G. Scalmani, V. Barone, G. A. Petersson, H. Nakatsuji, X. Li, M. Caricato, A. Marenich, J. Bloino, B. G. Janesko, R. Gomperts, B. Mennucci, H. P. Hratchian, J. V. Ortiz, A. F. Izmaylov, J. L. Sonnenberg, D. Williams-Young, F. Ding, F. Lipparini, F. Egidi, J. Goings, B. Peng, A. Petrone, T. Henderson, D. Ranasinghe, V. G. Zakrzewski, J. Gao, N. Rega, G. Zheng, W. Liang, M. Hada, M. Ehara, K. Toyota, R. Fukuda, J. Hasegawa, M. Ishida, T. Nakajima, Y. Honda, O. Kitao, H. Nakai, T. Vreven, K. Throssell, J. A. Montgomery, Jr., J. E. Peralta, F. Ogliaro, M. Bearpark, J. J. Heyd, E. Brothers, K. N. Kudin, V. N. Staroverov, T. Keith, R. Kobayashi, J. Normand, K. Raghavachari, A.

Rendell, J. C. Burant, S. S. Iyengar, J. Tomasi, M. Cossi, J. M. Millam, M. Klene, C. Adamo, R. Cammi, J. W. Ochterski, R. L. Martin, K. Morokuma, O. Farkas, J. B. Foresman, D. J. Fox, Gaussian Development Version, *Revision I.10*+, Gaussian, Inc.: Wallingford, CT, 2016.

[18] S. Jurinovich, L. Cupellini, C. A. Guido, B. Mennucci, *J. Comput. Chem.,* **2017**, *39*, 279–286.

Chapter 3

Theoretical Study on Optical Properties of Multichromophoric Systems Based on an Exciton Approach: Modification Guidelines

3.1. Introduction

Functions of molecular aggregates intrinsically originate in physical properties and interactions of constituent molecules. In particular, optical properties of multichromophoric systems such as absorption, emission, circular dichroism (CD), and circularly polarized luminescence (CPL) spectra drastically change depending on molecular compositions and structure, which is important for the applications to light emitting device,[1-5] photoreaction control,[6-13] and sensing and imaging.[14-19] Recently, a degree of freedom of supramolecular and polymer design has been significantly enhanced. It is possible to construct various molecular aggregates with designed arrangement of molecules by advanced experimental techniques, for example, nonequilibrium self-organization,[20,21] simultaneous arrangement on a porous crystal,[22-26] and sequence control in polymers or oligomers.[27-35] In the nonequilibrium self-organization, structurally different aggregates in nonequilibrium nondissipative states can be obtained depending on preparation protocols. The porous crystals have well-defined adsorption sites and enable the control of the relative positions and orientations of guest molecules within a confined space. The regulation of order of side-chain monomers in the oligomers and polymers can be achieved by copolymer synthesis strategies. Although the applicable scope of these methods is still limited, it is promising to construct the molecular aggregates with the designed structure. In this context, design guidelines are required for further development of photofunctions of the multichromophoric systems.

The Frenkel exciton which is a strongly bound electron–hole pair and its relevant concepts are useful for interpretation and expectation of trends of the optical properties of the multichromophoric systems. For instance, dependence of the absorption and emission on relative conformations of the chromophores is often interpreted by H- and J-

aggregates.[36-38] In the H-aggregate in which the chromophores overlap with a face-to-face arrangement, the lowest bright excitation is blue-shifted compared to the monomer, and electronic transition to the first excited state on the fluorescence is prohibited. The aggregate and crystal of the chromophores often suffer from aggregation-caused quenching (ACQ) due to H-aggregate formation through π–π stacking.[39] Although the ACQ is a significant problem in the application of the emission of the molecular aggregate, this character is utilized to suppress luminescence, for example, in a target selective biological probe having an on–off switch.[14,40] In the J-aggregate in which the chromophores are arranged head-to-tail, the transition probability to the first excited state is increased, and the transition energy is red-shifted. Another notable example is the exciton chirality method (ECM)[41] for the CD spectrum. However, applicable scope of these concepts is unknown for the complex multichromophoric systems which have different types of the chromophores and three-dimensionally stacked structure. For these systems, based on excitonic approaches to simulate the optical properties,[42,43] the author successfully applied a Frenkel-exciton decomposition analysis (FEDA) method[44] for evaluation of contributions from each chromophore to the optical spectra of the whole system.

In this work, the author aims to provide a strategy to improve the emission and CPL from the complex multichromophoric system with respect to its 3D structure as well as its intrinsic photophysical property by the excitonic calculation and FEDA. The author adopted the molecular aggregate of 2,5-diphenyl-1,4-distyrylbenzene with two trans double bonds (*trans*-DPDSB)[45] as an example due to its strong emission and complex structure. A needle-like crystal of *trans*-DPDSB is a first reported X-aggregate in which chromophores have cross-stacking structure with a molecular-plane angle of 70°, which

leads to highly fluorescent quantum yield (0.8) by avoiding the ACQ.[46,47] A chemical structure of the *trans*-DPDSB molecule is shown in Figure 3.1. In *trans*-DPDSB, two phenyl substituents are attached to a central phenyl ring of a poly(*p*-phenylene vinylene) (PPV)-type unit in order to generate CH/π interactions and realize the cross-stacking arrangement. A unit cell of the crystal and the system with identification numbers **1**–**9** of each chromophore are shown in Figures 3.2(a) and (b), respectively. This system is composed of two different conformational monomers **A** and **B** shown by blue and red in Figure 3.2(c). The crystal belongs to achiral space group $P2_1/c$ which is typical of organic molecular crystals and has no CD and CPL signals, while this system contains partially chiral structure. For example, a pair of chromophores **1** and **5** is in the chiral relation. A theoretical study on the isomers of DPDSB in the gas phase was conducted,[48] while its aggregate properties have not been investigated yet. Taken together, the system is suitable for discussing the optical properties of the complex multichromophoric system and its modification design strategy. Unfortunately, the absorption spectrum of the crystal, which provides information about the excited-state dynamics, has not been reported. The theoretical calculations of this work have indicated that this system is in a weak coupling regime where exciton coupling is considerably weaker than exciton–phonon coupling. That is, in the emission, the exciton mainly localizes on the monomer.

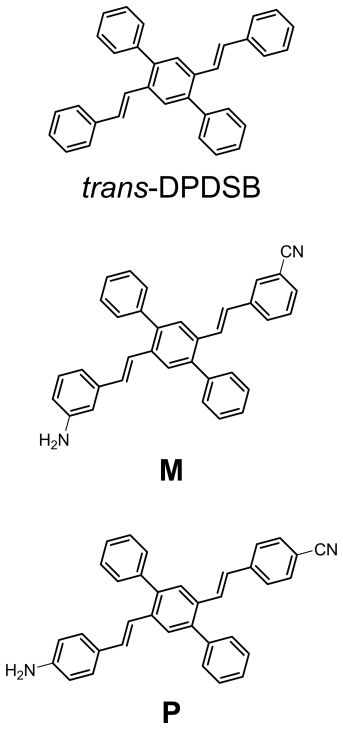

Figure 3.1. Chemical structures of *trans*-DPDSB and its derivatives **M** and **P** studied in this work.

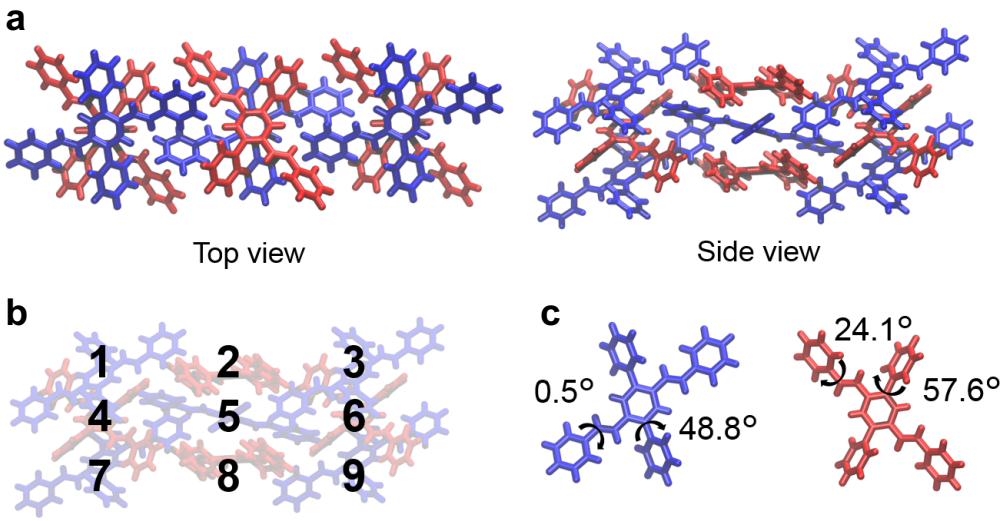

Figure 3.2. a) Multichromophoric system for a unit cell of the crystal of *trans*-DPDSB. b) Identification numbers of the individual chromophores. c) Two types of conformational structures of *trans*-DPDSB in the crystal. The dihedral angle values were taken from Ref. [45].

In this work, the author investigates the optical properties of the crystal of *trans*-DPDSB by the excitonic calculations and FEDA. The author has examined the absorption, emission, CD, and CPL spectra in the weak coupling case in terms of the photophysical properties of the molecules constituting the system; in particular, focusing on the mechanisms of disappearance of the CD and CPL in the achiral molecular cluster. Based on the analysis, the author has proposed the post-modification guidelines for the emission and CPL via control of transition dipole moments of individual chromophores, which can be implemented by manipulation of molecular species and arrangement of the multichromophoric system in practice. The author also studied an asymmetric multichromophoric system with derivatives of *trans*-DPDSB (Figure 3.1).

3.2. Methods

An adopted computational model is the multichromophoric system consisting of nine chromophores of *trans*-DPDSB (Figure 3.2(a), (b)). Eight monomers surrounding the central molecule which is supposed to relax the geometry in the first excited state are considered to be involved in electronic transitions and are included in the system. For the sake of simplicity, the system was rigorously symmetrized to a C_i point group in a tight cutoff level of structural parameters by using GaussView.[49] This operation almost does not change the original structure.

The excited state of each chromophore was calculated by using the time-dependent density functional theory (TD-DFT). The reliability of the TD-DFT calculations for various excited states has been well assessed by systematic benchmark studies.[50-53] The CAM-B3LYP[54] functional was employed in the present TD-DFT calculations because of its better description of charge-transfer or charge-polarization transitions, in particular

in aggregate systems. Accuracy of the electric transition dipole moment of the chromophore is a key factor for the optical properties of the aggregate system in the excitonic calculations. Most recently, the benchmark study on the direction and magnitude of the electric transition dipole moment of organic chromophores indicated that the range-separated hybrid exchange functionals including CAM-B3LYP are reliable.[53] It was systematically confirmed that the CAM-B3LYP can suitably describe the character and type of exciton in large π-conjugated systems.[55] In addition, for the exciton coupling, dependence of transition densities on the method is smaller than that of excited-state densities.[56]

Basis set dependence was carefully examined in the absorption spectrum of the monomer. The 6-31+G(d,p) basis set with which the vertical excitation energy and oscillator strength were almost converged was used to simulate the optical properties. The ground- and excited-state geometries of the monomers were optimized at the CAM-B3LYP/6-31G(d,p) level. The author confirmed that there was no imaginary vibrational frequency at the optimized structures. The integral equation formalism-polarizable continuum model (IEF-PCM)[57,58] was used to describe solvent effects of the THF solution in all the calculations of the monomer. The solvent effects on the excited-state geometry optimization were considered in the linear response (LR) scheme with equilibrium solvation. The LR-PCM with the non-equilibrium solvation was adopted to simulate the absorption spectrum. The emission energy was calculated by using the state-specific (SS) PCM with the non-equilibrium solvation.

Reorganization energy characterizes the relaxation dynamics of the exciton state in the multichromophoric systems. To evaluate the reorganization energy, the author performed the our own *N*-layer integrated molecular orbital molecular mechanics

(ONIOM) (QM:QM')[59-61] calculations. The localized transition on the single chromophore should be considered. Therefore, in the ONIOM calculation, innermost chromophore **5** in which the exciton coupling concentrates, and the exciton localizes on the first exciton state was treated as the model system with the TD-CAM-B3LYP/6-31G(d,p) level. The author employed the low-level CAM-B3LYP/3-21G(d) for the remaining part which is composed of the surrounding eight chromophores representing environmental effects. In the geometry optimization of the first excited state, only chromophore **5** was relaxed and the surrounding molecules were kept frozen. The reorganization energy was estimated as half the Stokes shift.

The optical properties were calculated using the Frenkel-exciton model generalized using the matrix method[62] to treat several states and molecules. In the simulation of the spectra on absorption and emission processes, five and three excited states, respectively, were considered for the chromophores. For the exciton coupling, which is off-diagonal terms of the Frenkel-exciton Hamiltonian, the author employed the Coulomb term calculated directly from the transition densities through analytical integral techniques.[63,64] The author neglected the exchange–correlation and overlap terms of the exciton coupling because these interactions are prohibited in the singlet states. The intermolecular charge-transfer transition usually has small transition probability. Moreover, excimer formation is not observed in the experimental emission spectrum of the crystal.[45] Therefore, the author also did not consider the charge-transfer state in the excitonic calculations. The absorption and CD spectra were simulated based on the crystal structure. The excited-state geometry of the multichromophoric system was optimized using same computational level with the reorganization energy except for the application of the TD-DFT to the real system at the low level of the ONIOM (QM:QM') method to

consider environmental effects in the excited state. In the large molecular aggregates such as crystals, anisotropic effects should be significant for the optical properties.[65-70] The readers can refer to Refs. [65–67] for the theories of anisotropic optical spectra and Refs. [68–70] for these molecular exciton approaches. This strategy is a general approach which can also be applied to randomly oriented molecular aggregates. The author has treated the multichromophoric system as the randomly oriented aggregates in order not to limit the modification strategy in this work, while the crystal has a regular structure.

The FEDA method is described in Chapter 2 of this thesis. All the calculations of the electronic states were performed using Gaussian 16 A.03 program suites.[71] The excitonic calculations and analyses were conducted using the EXcitonic Analysis Tool (EXAT)[72] combined with our originally developed program. The molecular structures were drawn with VMD.[73]

3.3. Results and Discussion

A. Monomer in solution and crystal

The optical properties of the monomer which is a building block of the multichromophoric system were investigated in this section. As mentioned above, there is a detailed theoretical study of the isolated *trans*-DPDSB molecule,[48] and the present results are qualitatively consistent with those reported previously, where the B3LYP functional[74] was used without considering solvent effects. To establish the computational level of this work, the author examined the optical properties of the monomer. The absorption spectra of the monomer in THF calculated using the 6-31G(d,p), 6-31+G(d,p), and 6-311+G(d,p) basis sets are shown in Figure 3.3 together with the corresponding electric transition dipole moments of two strong peaks. The TD-DFT calculations well

reproduced a trend of the absorption spectrum of the experiment regardless of the basis sets. Regarding the peak top in absorption, the calculations overestimated the transition energy about 0.25 eV at 6-31G(d,p), in contrast to about 0.16 and 0.14 eV at 6-31+G(d,p) and 6-311+G(d,p), respectively (see Table 3.S1). The direction of the electric transition dipole moment for the lowest excited state, which is important for the emission based on the Kasha rule, is almost the same for all the basis sets (Figure 3.S1). Since the absorption intensities also converged in the spectrum, 6-31+G(d,p) was employed for the further calculations in this work. Figure 3.S2 displays the molecular orbitals (MOs) relevant to the transitions with the large oscillator strength in the absorption (see also Table 3.S1). The MOs representing the first and second intense peaks localize on the distyrylbenzene (DSB) and p-terphenyl (PTP) moieties, respectively. As a result, the author confirmed that the DSB moiety is certainly responsible for the lowest absorption and emission within a picture of the Kasha rule, which supports the design concept of the *trans*-DPDSB crystal that the emission mainly originates in the DSB backbone and the PTP moiety rotates the DSB moieties in the stacked structure. The red shift in the solvent was estimated to be 0.1 eV from the calculations.

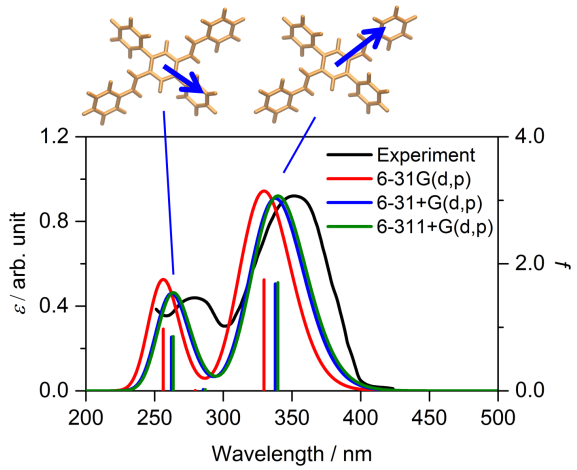

Figure 3.3. Absorption spectra of the monomer in THF calculated using 6-31G(d,p), 6-31+G(d,p), and 6-311+G(d,p) basis sets with the electric transition dipole moments corresponding to the intense peaks. The experimental spectrum was reproduced from Ref. [48]. The sticks represent the oscillator strength in each excited state.

The calculated emission energy was 2.89 eV (429 nm) in good agreement with the experimental values[75] of 2.74 to 3.07 eV (452 to 404 nm). The obtained Stokes shift representing the relaxation in the excited state was about 0.8 eV in perfect agreement with the experiment. Thus, the calculation level was validated by these results. Figure 3.4 displays superposition of the local minimum structures in the ground and excited states (individual structures with conformational parameters are shown in Figure 3.S3). The DSB backbone of the excited state is more planar than that of the ground state, while two phenyl substituents of the PTP are more perpendicular to the DSB moiety. Bond alternation, which is change of single and double bond nature, in the ground and excited states is shown in Figure 3.S4. In the ground state, the bond alternation is clear, while it decreases in the excited state. That is, π-conjugation significantly increases by the transition.

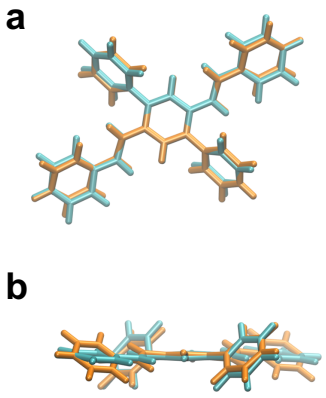

Figure 3.4. a) Top and b) side views of the superposition of the local minimum structures in the ground (orange) and excited (cyan) states of the monomer in THF.

In the investigation of the optical properties of the multichromophoric system, the photophysical properties of the constituent chromophores are important. Figure 3.5 shows the absorption spectra and corresponding electric transition dipole moments of two kinds of monomers **5** (**A**) and **6** (**B**) in different geometries (Figure 3.2(b)) constituting the crystal of *trans*-DPDSB. The MOs relevant to the main absorption peaks are shown in Figures 3.S5 and 3.S6. The trends of the absorption spectra of chromophores **5** and **6** are quite similar, while the absorption peak of **5** is lower by about 0.2 eV than that of **6**, which indicates that the exciton tends to localize on chromophore **A** in the first exciton state of the multichromophoric system.

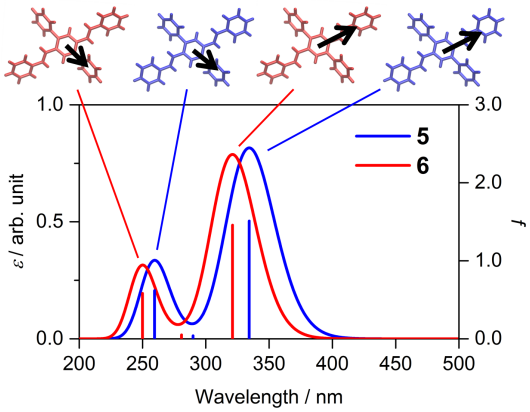

Figure 3.5. Absorption spectra of two kinds of monomers **5** (**A**) and **6** (**B**) constituting the crystal with the electric transition dipole moments corresponding to the intense peaks. The sticks represent the oscillator strength in each excited state.

B. Multichromophoric system for crystal

The result of the excitonic calculation of the absorption spectrum is shown in an upper panel of Figure 3.6. The absorption spectra of the monomer and multichromophoric system show a similar trend due to the weak exciton coupling. The FEDA revealed that the local absorption properties of each chromophore are dominant, while inter-chromophore contribution is minor. In comparison with the whole system, the contributions of each inner-chromophore term are 12–13%. A lower panel of Figure 3.6 shows the FEDA results. The decomposed absorption spectra for the individual chromophores are almost the same in each conformational structure **A** and **B**. Therefore, only these of chromophores **1** and **2**, and the sum for each structure **A** and **B** are shown in the lower panel of Figure 3.6. All the decomposed spectra which originate from the individual monomers are compared in Figure 3.S7.

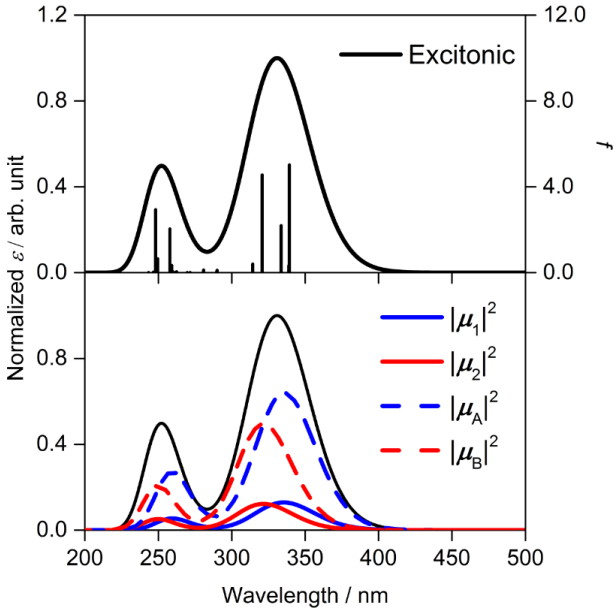

Figure 3.6. Absorption spectrum of the multichromophoric system in the upper panel and FEDA results in the lower panel. The sticks represent the oscillator strength in each exciton state.

The rotatory strength of the total system is zero as shown in Figure 3.S8(a). The chromophore aggregate in the C_i symmetry is achiral and optically inactive, which leads to no CD signal. First, the author divided the total CD spectrum into the physical components which are the μm and $\mu\mu$ terms. The spectra for the μm and $\mu\mu$ terms also do not emerge as shown in upper and lower panels of Figure 3.S8(b), respectively. Second, for the further interpretation how the CD vanishes in the achiral system including the partially chiral structures, the author estimated the chirality from the maximum absolute values of each decomposed spectrum. The sum of absolute values of the $\mu\mu$ components accounts for 97% of the total absolute values. Thus, Figure 3.7 shows the FEDA result for the selected $\mu\mu$ terms, which originates in the different conformations, with corresponding pairs of the chromophores. The other decomposed spectra with the strong

absolute intensity are shown in Figure 3.S9. The author found that the pairs of the decomposed CD spectra with opposite signs which are caused by the enantiomeric relation cancel out each other.

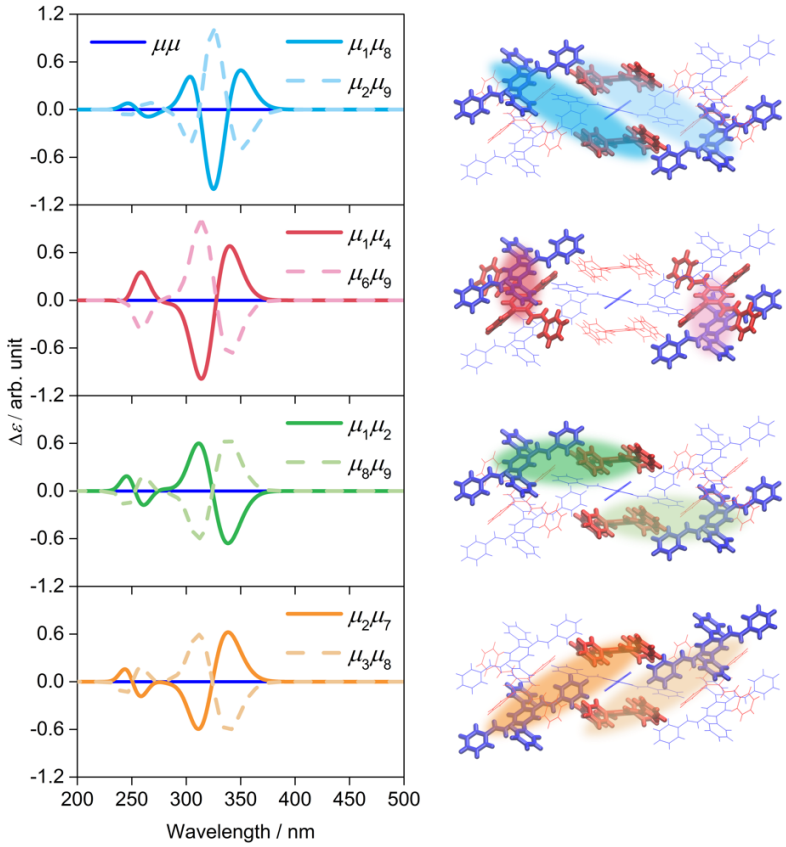

Figure 3.7. FEDA results for the CD spectrum of the multichromophoric system. Only corresponding chromophores for the decomposed spectra are represented in the licorice models with the bold bonds.

To examine the relaxation dynamics of the excited state of the multichromophoric system, the reorganization energy was estimated by using the ONIOM method. The calculated reorganization energy is 0.38 eV, which is much larger than the strongest exciton coupling of 0.051 eV. Therefore, the exciton–vibration coupling which promotes

the exciton localization is dominant over the exciton coupling with a tendency to the delocalization. The absorption of the aggregate is a superposition of the absorption of the individual monomers in the Franck–Condon principle. On the other hand, it is considered that the exciton mainly localizes on the single chromophore in the emissive process.

Figure 3.8(a) shows the emission spectrum of the multichromophoric system. The experimental and calculated emission spectra are in good agreement. The structure obtained in the experimental spectrum is assumed to be vibronic or other electronic states. The FEDA results are shown in Figures 3.8(b) and (c). The exciton electric transition dipole moments for the individual monomers in the emissive process are shown in Figure 3.9. The author notes that only the relative orientations of each transition dipole moment are meaningful. As shown in Figure 3.8(b), the author found that the strongest contribution to the emission of the entire system is caused by the local transition of the central chromophore, and the corresponding exciton electric transition dipole moment is much larger than the others (see also Figure 3.9). The eight decomposed spectra with the relatively strong intensity are shown in Figure 3.8(c). The FEDA clearly revealed that the surrounding chromophores contribute to the emission through the interaction with the relaxed chromophore. The decomposed spectra of the $\mu\mu$ interactions between chromophores **2** and **5**, **5** and **8** behave like the H-aggregate, i.e, $\mu_2\mu_5$ and $\mu_5\mu_8$ have the negative contributions to the emission. On the other hand, the other intense decomposed spectra have the positive contributions like the J-aggregate. These investigations indicate that introducing strong exciton coupling to this system is effective for enhancement of the emission intensity.

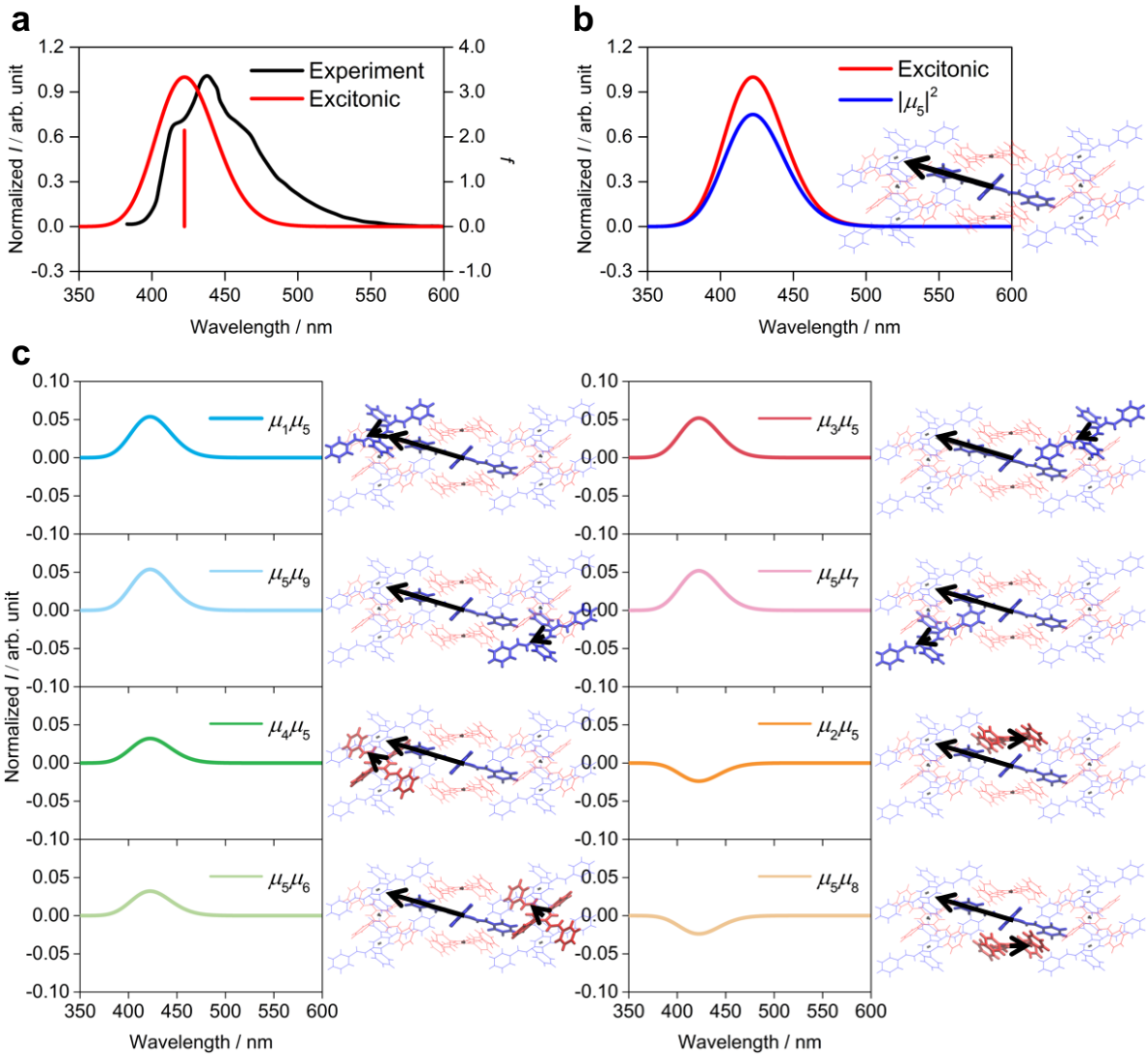

Figure 3.8. a) Emission spectrum of the multichromophoric system and b, c) FEDA results. Only corresponding chromophores with the exciton electric transition dipole moments for the decomposed spectra are represented in the licorice models with the bold bonds. The experimental spectrum was reproduced from Ref. [45]. The stick represents the oscillator strength.

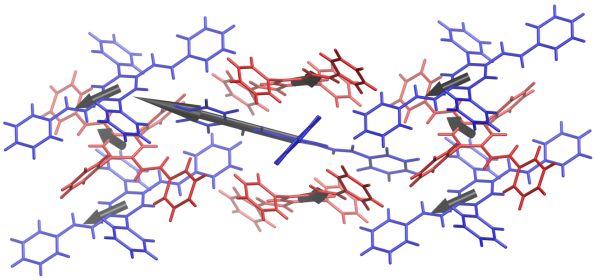

Figure 3.9. Exciton electric transition dipole moments of the chromophores constituting the multichromophoric system for the emissive process. The transition dipole moment of central chromophore **5** is scaled by 1/6.

The CPL signal of the multichromophoric system does not emerge in the simulation as well as the CD spectrum (Figure 3.S10(a)). The FEDA shows that the μm and $\mu\mu$ components of the spectrum also do not arise (Figure 3.S10(b)). As in the case of the CD spectrum, the author estimated these terms in the CPL and found that the $\mu\mu$ term is dominant. In the $\mu\mu$ components, the interactions of the exciton electric transition dipole moments between the central monomer and the surrounding monomers mainly generate the CPL as shown in Figure 3.10. However, the $\mu\mu$ interactions cancel out each other in the enantiomeric conformations.

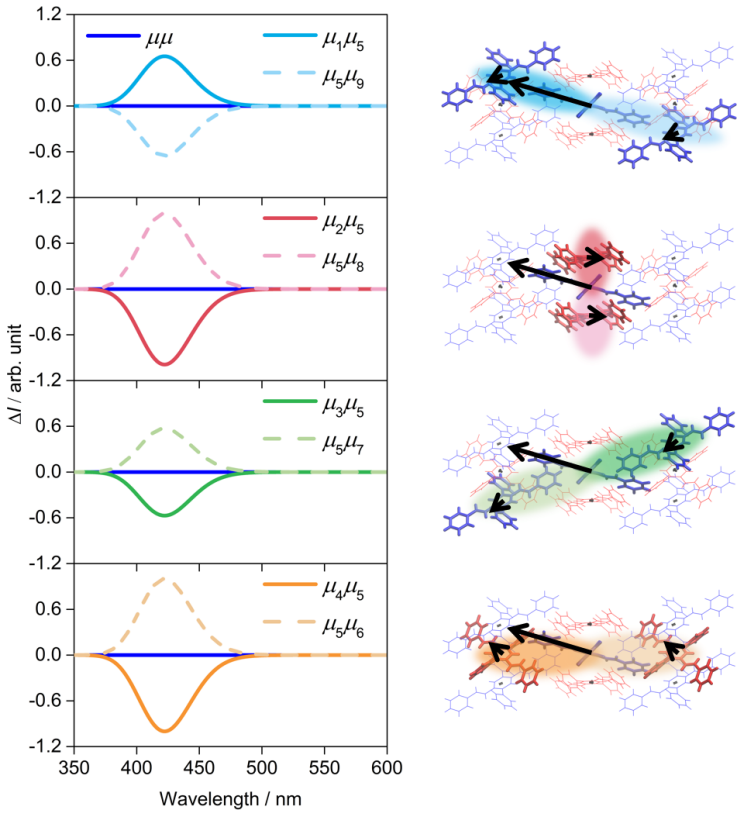

Figure 3.10. FEDA results for the CPL spectrum of the multichromophoric system. Only corresponding chromophores with the exciton electric transition dipole moments for the decomposed spectra are represented in the licorice models with the bold bonds.

C. Computational modification guidelines of emission and CPL

The nature of the optical spectra of the present multichromophoric system was clarified by the excitonic calculation and FEDA. Here, the modification guidelines for the emission and CPL of the multichromophoric system based on the exciton state are discussed. The modification guidelines are attributed to the control of the local optical properties of the chromophores constituting the multichromophoric system. In practice, it is possible to implement this modification by the manipulation of the molecular species and arrangement of the multichromophoric system. The author assumed that distribution of the exciton among the chromophores does not change; the control of exciton dynamics is

beyond the scope of this work. However, external manipulation of a population of the exciton, for instance, by nanoplasmonics is theoretically proposed,[76] which would be promising to overcome this limitation.

Because of the weak coupling, the exciton substantially localizes to a chromophore *M* in the emission, which is expressed as

$$\sum_{a}^{n_M}\left(C_{Ma}^{1}\right)^2 >> \sum_{j\neq M}^{N}\sum_{b}^{n_j}\left(C_{jb}^{1}\right)^2$$

where C_{ia}^{K} is the exciton coefficient for the *a*th local excited state of the unit *i* (please see Chapter 2) and $\sum_{i}^{N}\sum_{a}^{n_i}\left(C_{ia}^{K}\right)^2 = 1$. From the result of the exciton calculation, $\sum_{a}^{n_M}\left(C_{Ma}^{1}\right)^2$ and $\sum_{j\neq M}^{N}\sum_{b}^{n_j}\left(C_{jb}^{1}\right)^2$ are 0.987 and 0.013, respectively, in the present system. This indicates that the exciton almost localizes on monomer **5**. The monomer on which the exciton localizes is a key to improve the optical functions of the system in the weak coupling regime. In the emission, the FEDA clearly shows that the emission is mainly due to the local transition of chromophore **5**, and the surrounding chromophores contribute via the interaction with central monomer **5**. In addition, the $\mu\mu$ interaction between chromophore **5** and its surrounding chromophores is dominant in the CPL. The exciton electric transition dipole moment of chromophore **5** is composed of the local transition ones. The author found that the component for the first excited state is dominant (>99% in comparing the strengths). To improve the intensities of the emission and CPL, it is most effective to increase the electric transition dipole moment for the first excited state of monomer **5**. To examine this guideline numerically, the transition dipole moment was extended to 1.5 times the original one. As the result, the emission and CPL were

enhanced as shown in Figures 3.S11 and 3.S12.

To generate the CPL spectrum, the orientation control of the electric transition dipole moments of the chromophores are required. The FEDA clearly indicated that the contributions from each enantiomeric conformation offset each other in the achiral aggregate as shown in Figure 3.10. Therefore, if one of the decomposed spectra in the mirror image relation is reversed, the CPL can be generated. The author inverted the signs of negative CPL elements $\mu_2\mu_5$, $\mu_3\mu_5$, $\mu_4\mu_5$, $\mu_5\mu_9$ to generate the right-handed CPL. From the equation of the decomposed rotatory strength shown in Chapter 2 of this thesis, it is considered that μ_2, μ_3, μ_4, and μ_9 for μ_5 can be manipulated by the inversion of the angle between the vectors. The proposed modification in this work is based on the exciton state of the calculated multichromophoric system, i.e., the exciton coefficients, which means that the direction of the exciton electric transition dipole moments of the individual monomers cannot be reversed in this guideline. The electric transition dipole moment for the first excited state is dominant at μ_2, μ_3, μ_4, and μ_9 (>99% in comparing the strengths). Therefore, the directions of the electric transition dipole moments of the monomers **2**, **3**, **4**, and **9** for the first excited state were manipulated to invert these dihedral angles (defined in Figure 3.S13) with respect to that of **5**. The simplest way to realize this manipulation is to change the orientations of the monomers in the multichromophoric system according to the control of the transition dipole moments suggested by the modification guideline, which is worth challenging by the molecular arrangement methodologies for molecular aggregates like the nonequilibrium self-organization, the adsorption on the tailored space of the porous crystal. The schematic representation of the modification about, for example, $\mu_4\mu_5$ is shown in Figure 3.11. The modified CPL spectrum and FEDA result are shown in Figure 3.12 together with these of the improved

transition dipole moment as above. The CPL spectrum was numerically produced and enhanced according to the computational post-modification guideline. The change of emission spectrum can be negligible in this modification (Figure 3.S14).

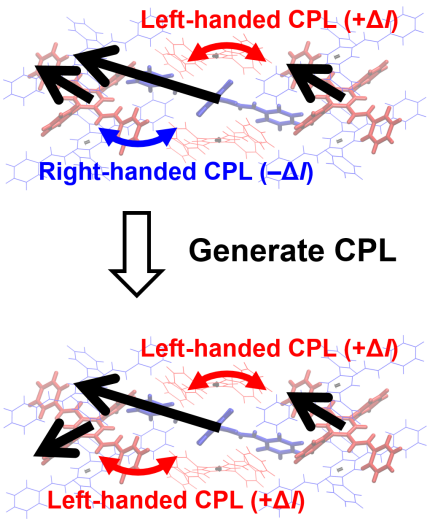

Figure 3.11. Schematic representation of the post-modification guideline to produce CPL. The bold arrows are the exciton electric transition dipole moments of the chromophores **4**, **5**, and **6** for the emissive process.

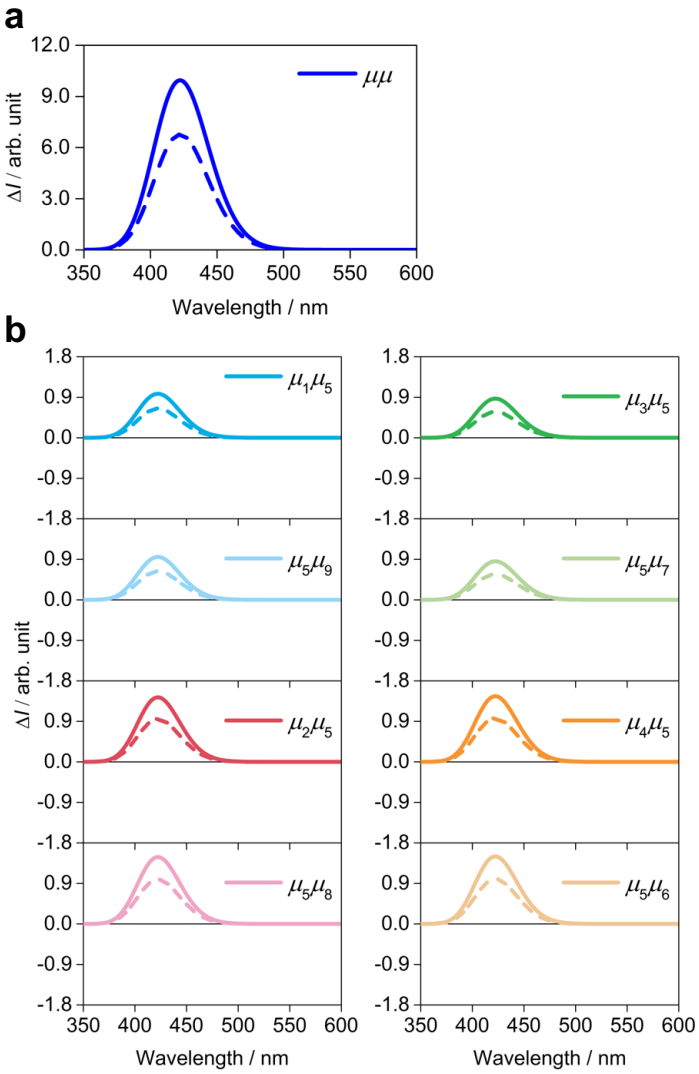

Figure 3.12. a) Modified CPL spectra based on the modification guideline and b) FEDA results. The broken and solid lines respectively indicate before and after the modification of the electric transition dipole moment for the first excited state of chromophore **5**.

D. Asymmetric multichromophoric system

Here the optical properties of an asymmetric multichromophoric system by introducing the asymmetry in the molecular unit were investigated. Figure 3.1 shows the chemical structures of asymmetric molecules **M** and **P** designed based on *trans*-DPDSB to be chiral. In the molecules **M** and **P**, an electron-donating NH_2 and an electron-

withdrawing CN groups are introduced into the *trans*-DPDSB molecule. First, the author examined the emission properties of the molecules **M** and **P**. The calculation results are summarized in Table 3.S3 in comparison with the *trans*-DPDSB molecule. The rotatory strengths are nonzero and have a negative value, which leads to the right-handed CPL (negative ΔI). The electric transition dipole strength for the emission increases in both molecules. Next, the author investigated the emission and CPL of the asymmetric multichromophoric system. The author replaced the central monomer **5** of the multichromophoric system of *trans*-DPDSB with **M** because its rotatory strength is larger than that of **P**. The new central monomer is defined as **5'**. Such molecular assembly of different molecules is expected to be constructed by using the molecular arrangement technologies in practice. The reorganization energy is 0.44 eV and much larger than the strongest exciton coupling of 0.058 eV, which indicates that this system is in the weak exciton coupling region. The optimized structure of the asymmetric multichromophoric system in the first excited state is shown in Figure 3.S17. Figures 3.S18 and 3.13 respectively show the emission and CPL spectra of the asymmetric multichromophoric system. The exciton electric transition dipole moments for the individual monomers in the emissive process are shown in Figure 3.S19. The nature of the emission spectrum is qualitatively the same as that of the achiral system. On the other hand, the asymmetric multichromophoric system has the CPL spectrum because of its chiral structure. The FEDA shows that positive and negative spectra originate from the μm and $\mu\mu$ interactions, respectively. The spectrum of the $\mu\mu$ interaction has a strong intensity. As the result, the CPL spectrum of the system has the right-handed CPL. The dominant component of the μm interaction is the intrinsic rotatory strength of the monomer **5'** and shown in Figure 3.13(b) as $R_{5'}$. $R_{5'}$ has the opposite-handed CPL nature to the monomer in the vacuum due

to the structural modification induced by the steric effect in the multichromophoric system. The $\mu\mu$ interactions between the central monomer and the surrounding monomers have the strong CPL intensities, while these almost cancel out each other (Figure 3.13(c)).

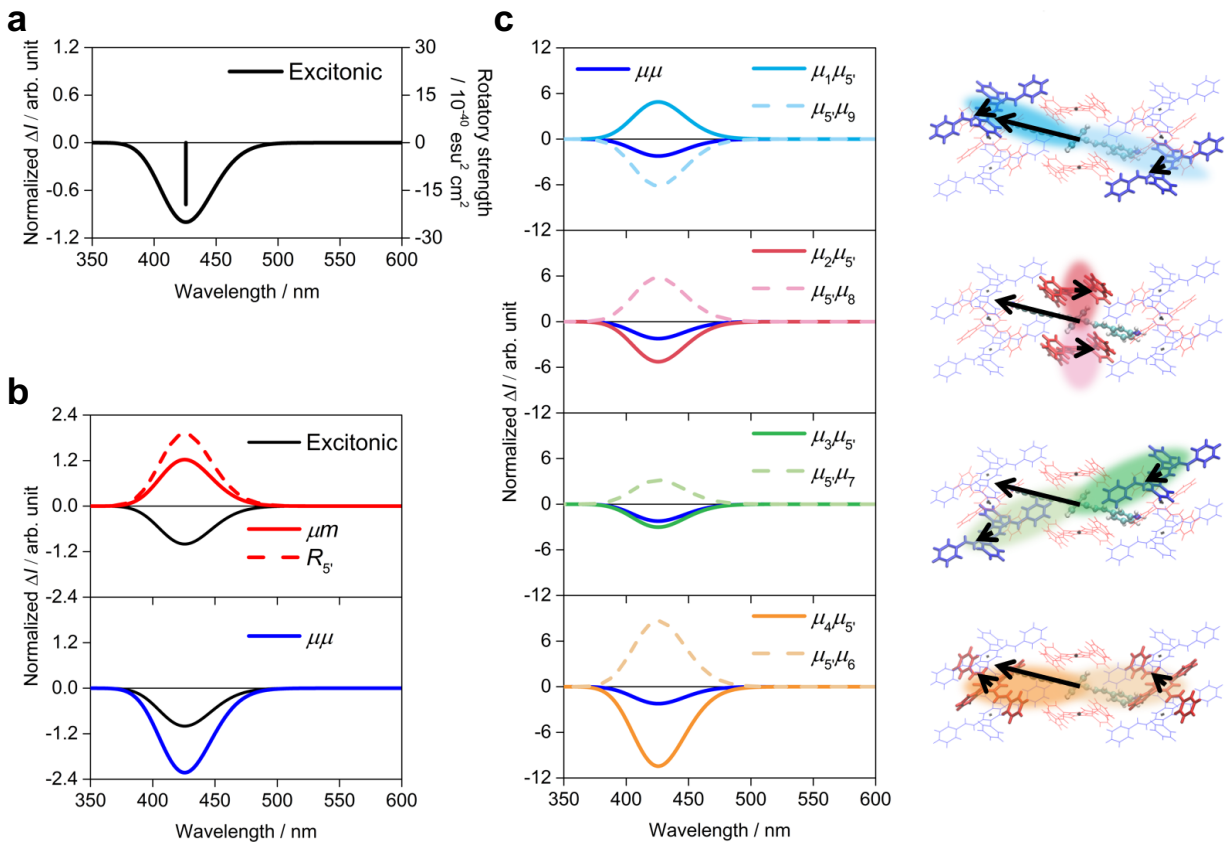

Figure 3.13. a) CPL spectrum of the asymmetric multichromophoric system and b, c) FEDA results. Only corresponding chromophores with the exciton electric transition dipole moments for the decomposed spectra are represented in the licorice models with the bold bonds. The stick represents the rotatory strength.

3.4. Conclusions

The generation and annihilation mechanisms of the optical properties of the achiral multichromophoric system and its modification guidelines for the emission and CPL have

been presented. The absorption and emission spectra are mainly due to the local transition in the individual chromophores. The interactions between the relaxed chromophore and the surrounding ones positively contribute to the emission intensity. This investigation suggests that the intensity can be considerably improved by introducing strong exciton coupling. The interactions of the exciton electric transition dipole moments between the chromophores have significant potential for the CD and CPL spectra, while these pairs in the structural enantiomer relation contained in the system cancel out each other, which leads to no chiral activity. In particular, the exciton localized chromophore is the key to improve the emission and CPL spectra in the weak coupling region. The modification guidelines suggested that the improvement of the electric transition dipole moment for the first excited state of this chromophore is most effective. Moreover, the control of the relative conformations of the electric transition dipole moments of some (surrounding) chromophores leads to the generation of the CPL signal. These modifications were numerically simulated. The author also performed the exciton analysis for the asymmetric system. This kind of FEDA with quantum chemical calculations is useful for the further development or discovery of high-performance optical materials.

Supporting Information

Table 3.S1. Absorption properties of the monomer in THF

Basis set	ES[a]	λ (nm)	VEE[b] (eV)	f	Character
6-31G(d,p)	1	330	3.76	1.7477	H[c] → L[d]
	2	280	4.43	0.0068	H → L+1, H–2 → L
	3	270	4.59	0.0000	H–1 → L, H → L+2
	4	256	4.84	0.9732	H–2 → L, H → L+1
	5	243	5.11	0.0000	H–5 → L
6-31+G(d,p)	1	338	3.67	1.6837	H → L
	2	285	4.34	0.0207	H → L+1, H–2 → L
	3	279	4.44	0.0000	H → L+2, H–1 → L
	4	262	4.73	0.8482	H–2 → L, H → L+1
	5	249	4.98	0.0000	H–5 → L, H–1 → L+6
6-311+G(d,p)	1	340	3.65	1.7053	H → L
	2	287	4.32	0.0210	H → L+1
	3	280	4.42	0.0000	H → L+2, H–1 → L
	4	264	4.70	0.8546	H–2 → L
	5	250	4.95	0.0000	H–5 → L, H → L+4
Experiment[e]	1	353	3.51		
	2	277	4.48		

[a]ES: Excited State. [b]VEE: Vertical Excitation Energy.

[c]H: Highest occupied molecular orbital. [d]L: Lowest unoccupied molecular orbital.

[e]from Ref. [75].

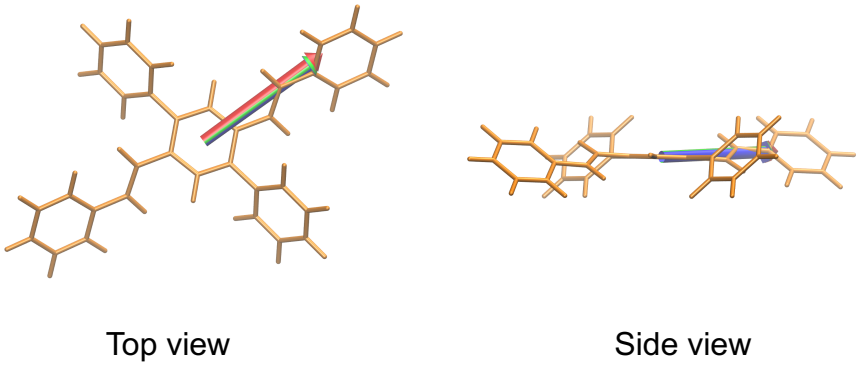

Figure 3.S1. Electric transition dipole moment for the first excited state of the monomer in THF (red, 6-31G(d,p); blue, 6-31+G(d,p); green, 6-311+G(d,p)).

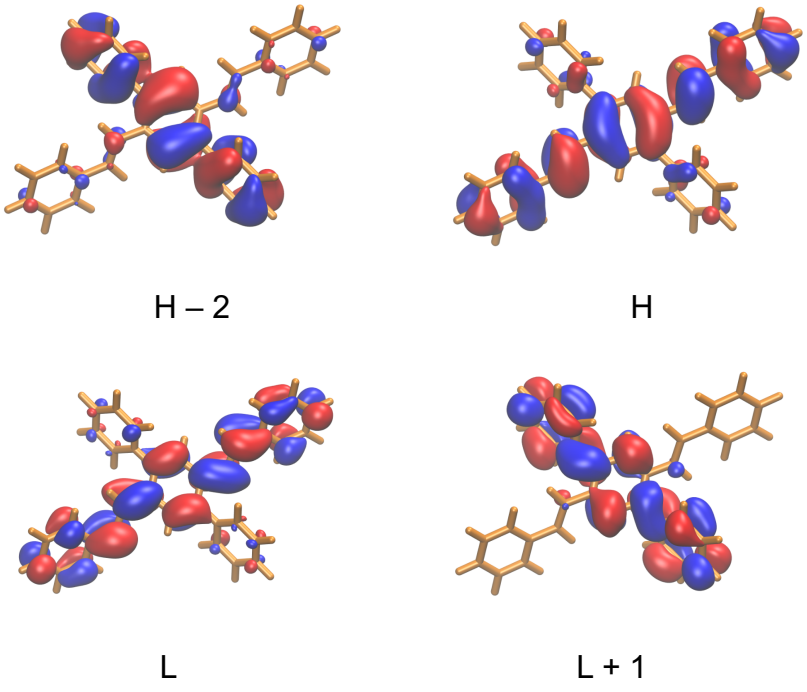

Figure 3.S2. Frontier MOs of the monomer in THF (Isovalue = |0.02|).

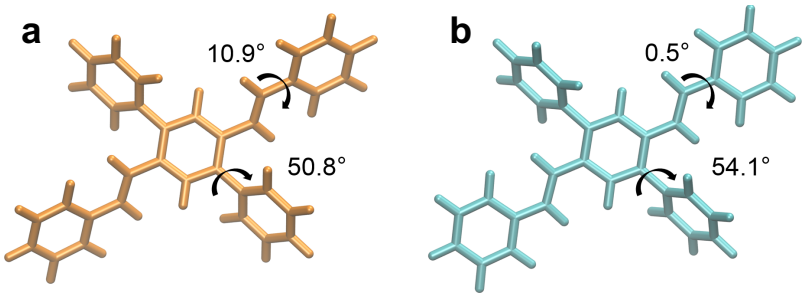

Figure 3.S3. Local minimum structures in a) ground and b) excited states of the monomer in THF.

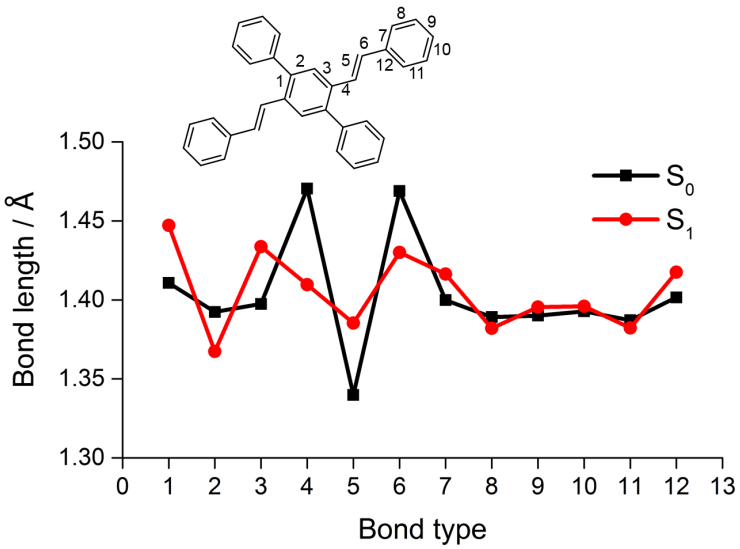

Figure 3.S4. Bond alternation for the transition of the monomer in THF.

Table 3.S2. Absorption properties of the monomer in the crystal

Monomer	ES[a]	λ (nm)	VEE[b] (eV)	f	Character
5	1	334	3.71	1.5103	H[c] → L[d]
	2	290	4.28	0.0392	H → L+1, H–1 → L
	3	270	4.59	0.0000	H → L+2, H–2 → L
	4	260	4.78	0.6190	H–1 → L, H → L+1
	5	247	5.03	0.0000	H–5 → L
6	1	321	3.86	1.4576	H → L
	2	281	4.42	0.0499	H–2 → L, H → L+1
	3	261	4.75	0.0000	H–1 → L, H → L+2
	4	250	4.96	0.5822	H → L+1, H–2 → L
	5	243	5.09	0.0000	H–4 → L, H → L+7

[a]ES: Excited State. [b]VEE: Vertical Excitation Energy.

[c]H: Highest occupied molecular orbital. [d]L: Lowest unoccupied molecular orbital.

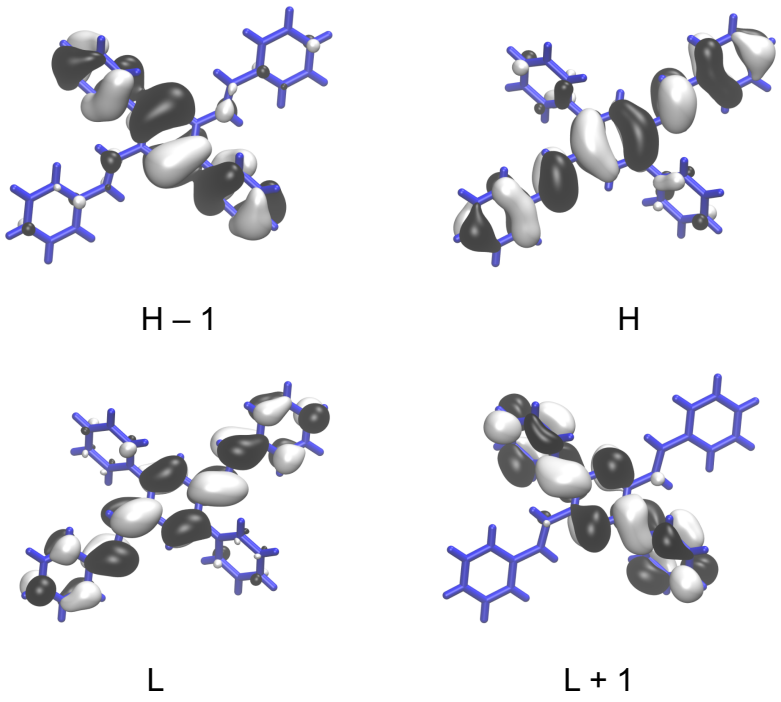

Figure 3.S5. Frontier MOs of chromophore **5** (**A**) in the crystal (Isovalue = |0.02|).

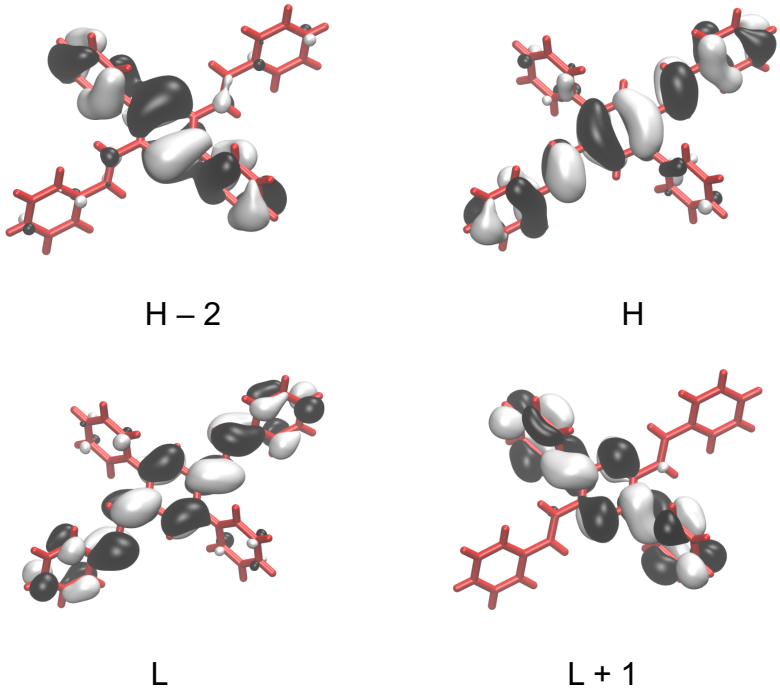

Figure 3.S6. Frontier MOs of chromophore **6** (**B**) in the crystal (Isovalue = |0.02|).

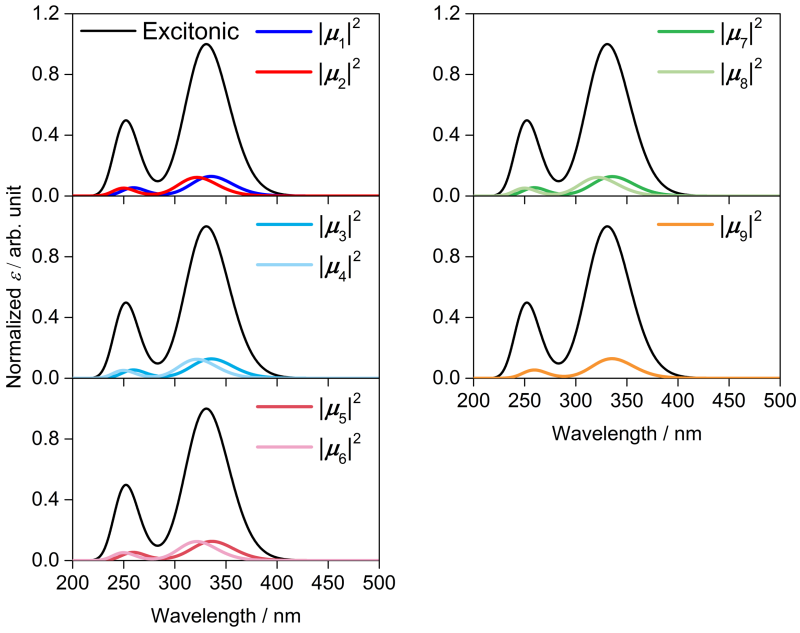

Figure 3.S7. Absorption spectrum of the multichromophoric system and FEDA results.

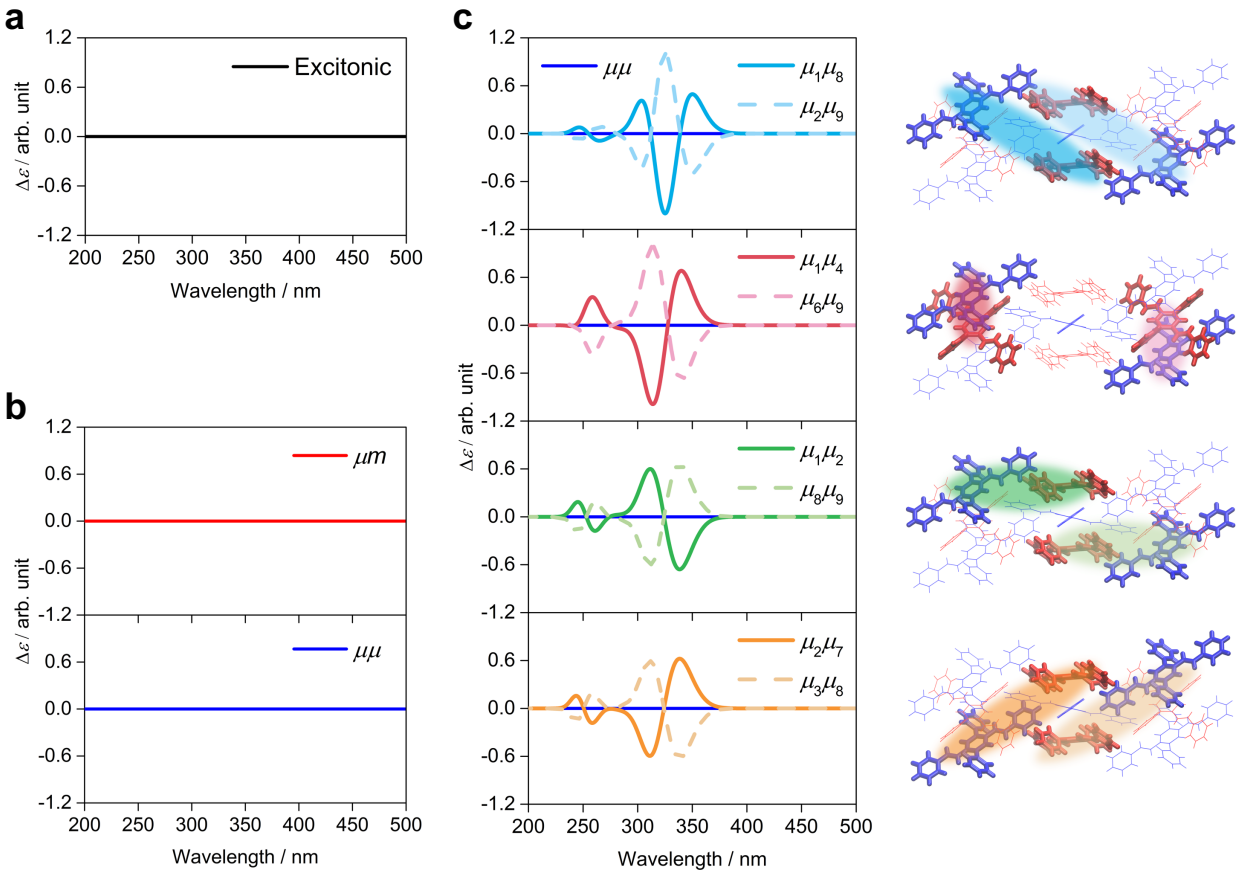

Figure 3.S8. a) CD spectrum of the multichromophoric system and b, c) FEDA results. Only corresponding chromophores for the decomposed spectra are represented in the licorice models with the bold bonds.

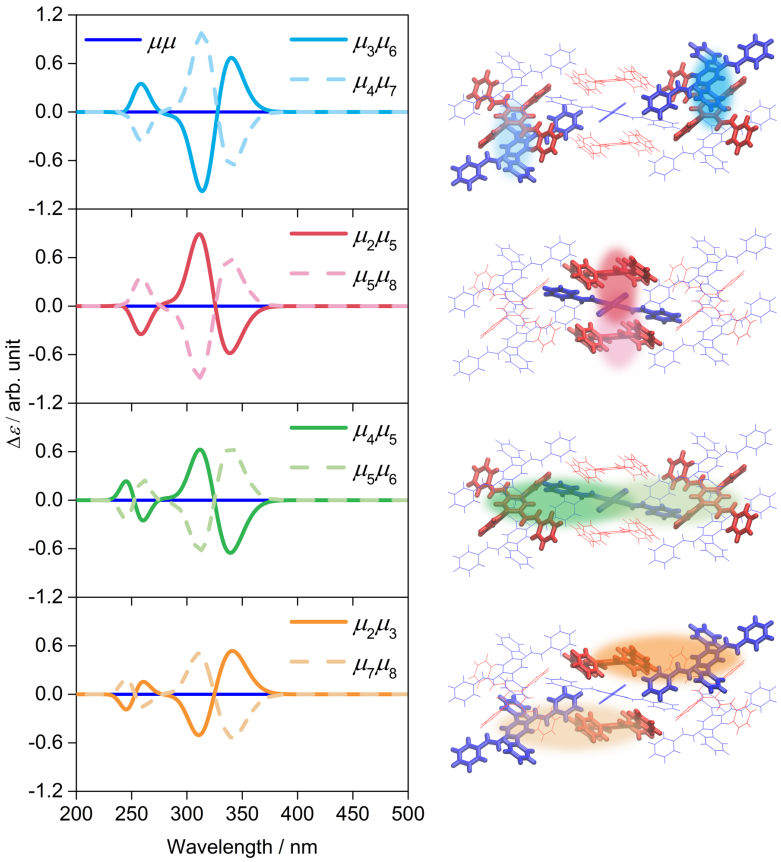

Figure 3.S9. FEDA results for the CD spectrum of the multichromophoric system. Only corresponding chromophores for the decomposed spectra are represented in the licorice models with the bold bonds.

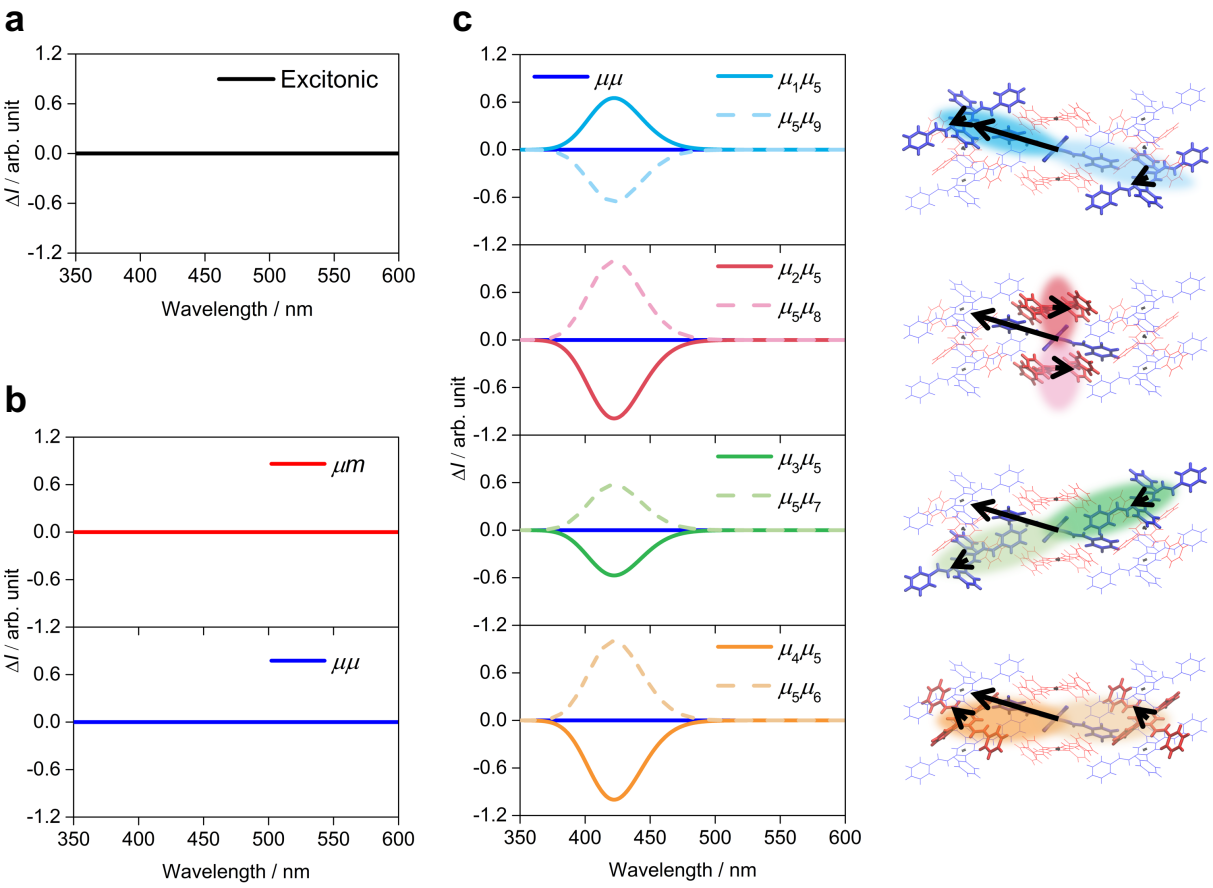

Figure 3.S10. a) CPL spectrum of the multichromophoric system and b, c) FEDA results. Only corresponding chromophores with the exciton electric transition dipole moments for the decomposed spectra are represented in the licorice models with the bold bonds.

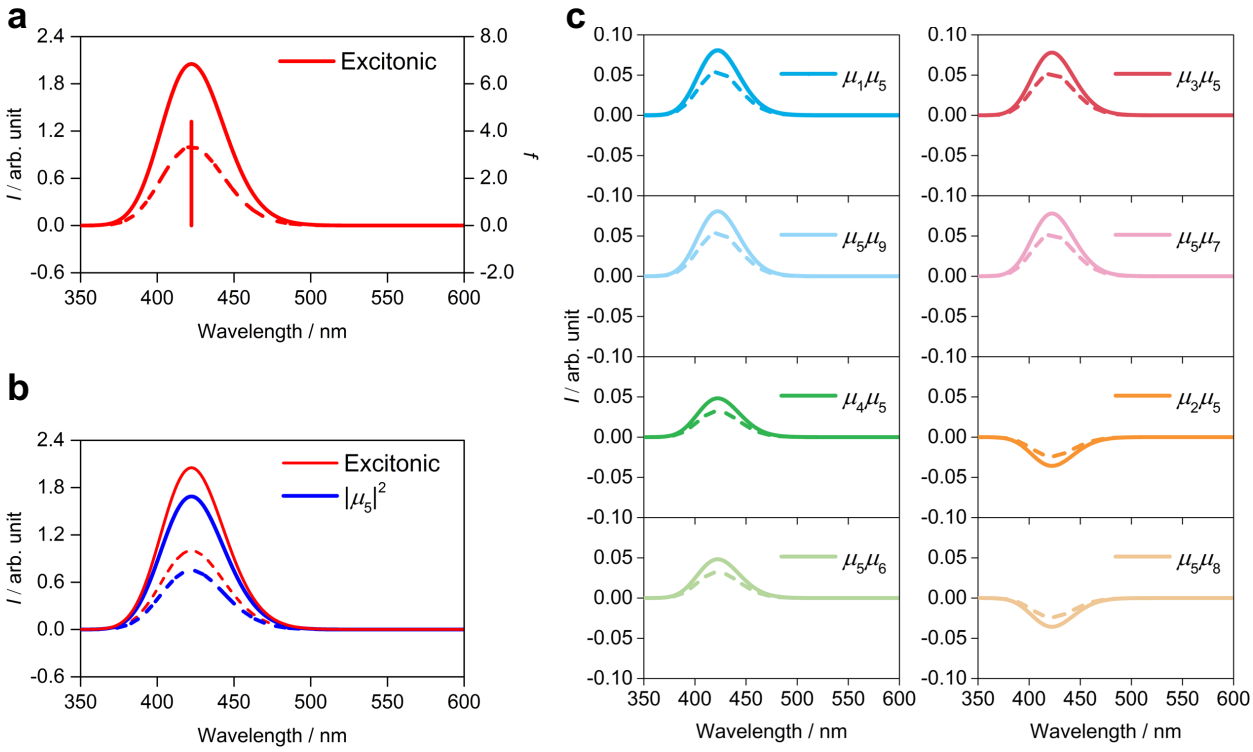

Figure 3.S11. a) Enhanced emission spectrum of the multichromophoric system and b, c) FEDA results. Broken and solid lines respectively indicate before and after the modification of the electric transition dipole moment for the first excited state of chromophore **5**. The stick represents the oscillator strength.

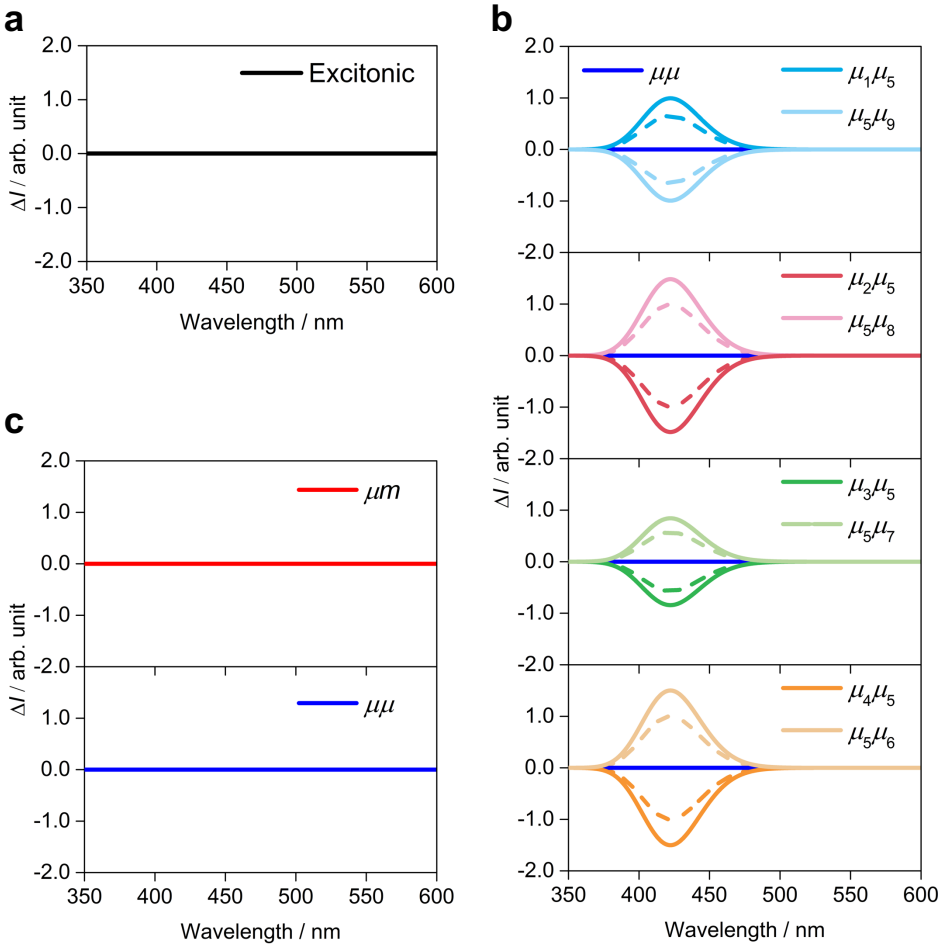

Figure 3.S12. a) Enhanced CPL spectrum of the multichromophoric system and b, c) FEDA results. Broken and solid lines respectively indicate before and after the modification of the electric transition dipole moment for the first excited state of chromophore **5**.

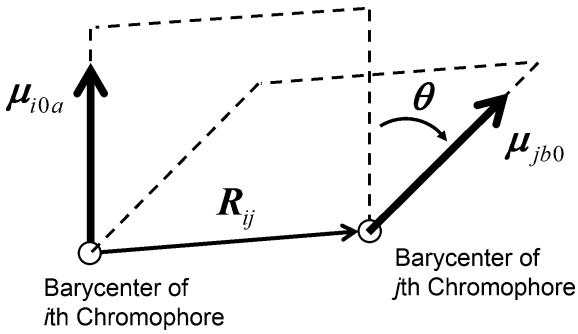

Figure 3.S13. Dihedral angle θ for electric transition dipole moments of *i*th and *j*th chromophores.

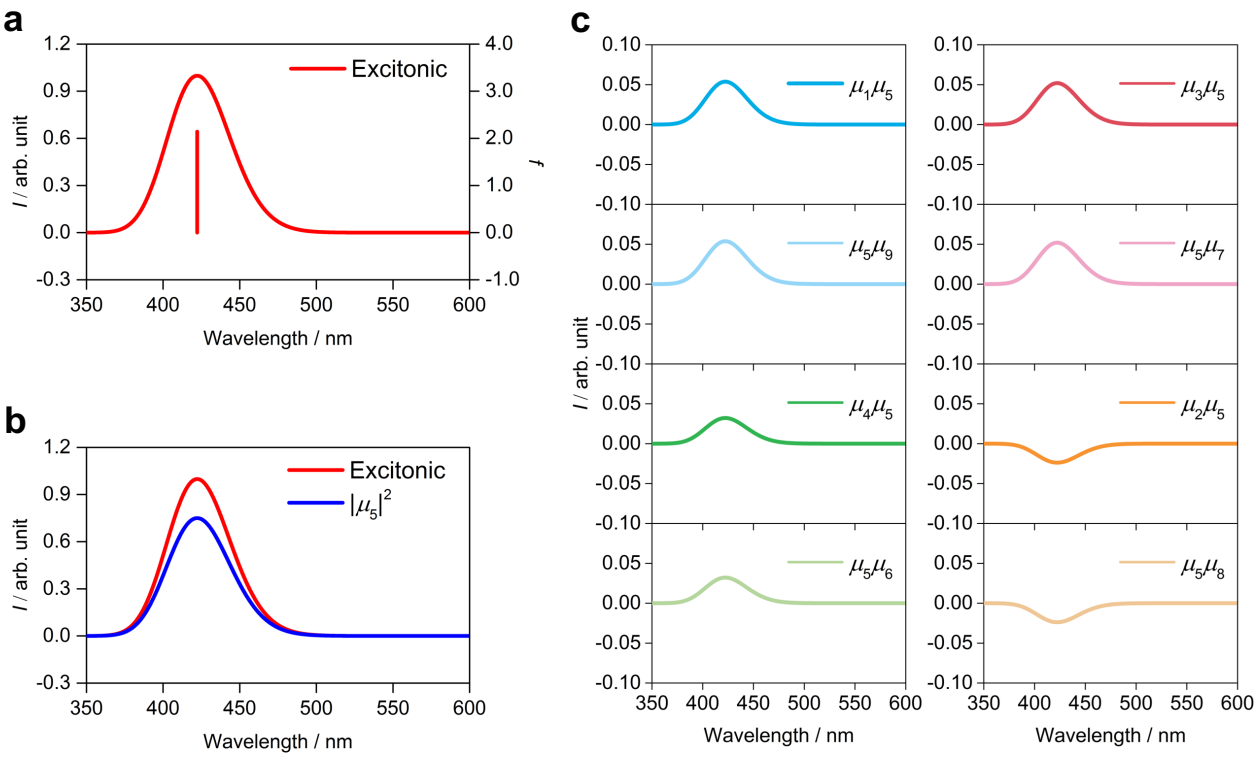

Figure 3.S14. a) Emission spectrum of the multichromophoric system in the modification of the CPL spectrum and b, c) FEDA results. The stick represents the oscillator strength.

Table 3.S3. Emission properties of asymmetric monomers **M** and **P**

Monomer	λ (nm)	VEE[a] (eV)	f	D^b (a.u.)	R (10^{-40} esu^2 cm^2)	Character
M	424	2.92	1.640	0.2643	-9.1	H[c] → L[d]
P	450	2.75	1.903	0.2889	-2.9	H → L
Trans-DPDSB	431	2.88	1.636	0.2593	0.0	H → L

[a]VEE: Vertical Excitation Energy. [b]*D*: Electric transition dipole strength.

[c]H: Highest occupied molecular orbital. [d]L: Lowest unoccupied molecular orbital.

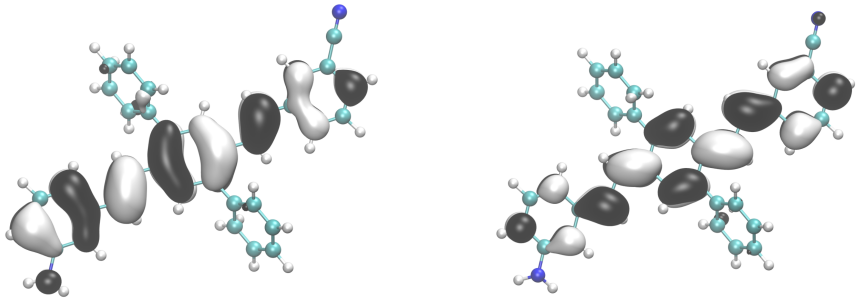

H L

Figure 3.S15. Frontier MOs of asymmetric monomer **M** (Isovalue = |0.02|).

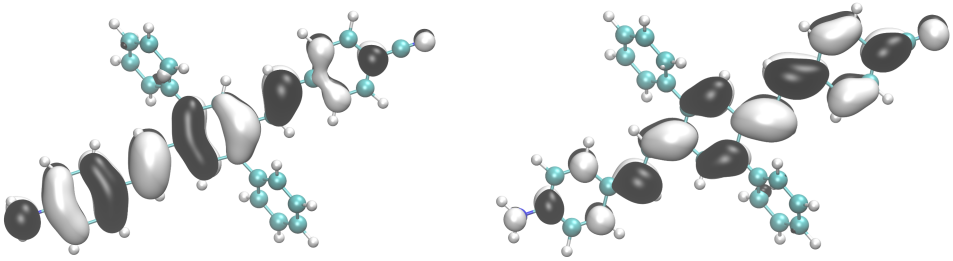

H L

Figure 3.S16. Frontier MOs of asymmetric monomer **P** (Isovalue = |0.02|).

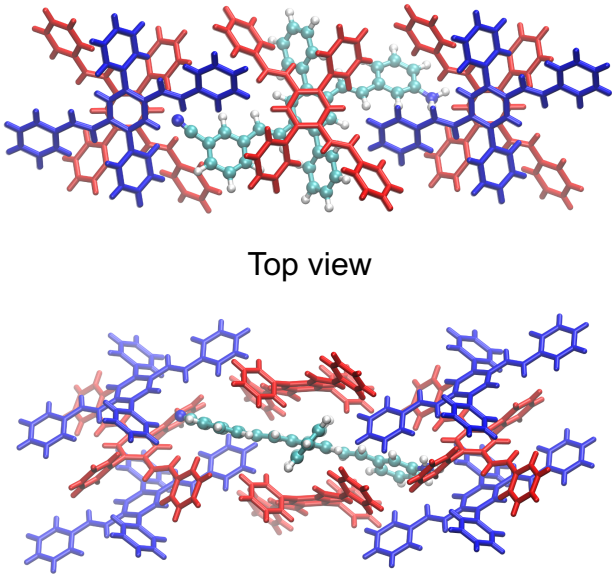

Figure 3.S17. Optimized structure of the asymmetric multichromophoric system in the first excited state.

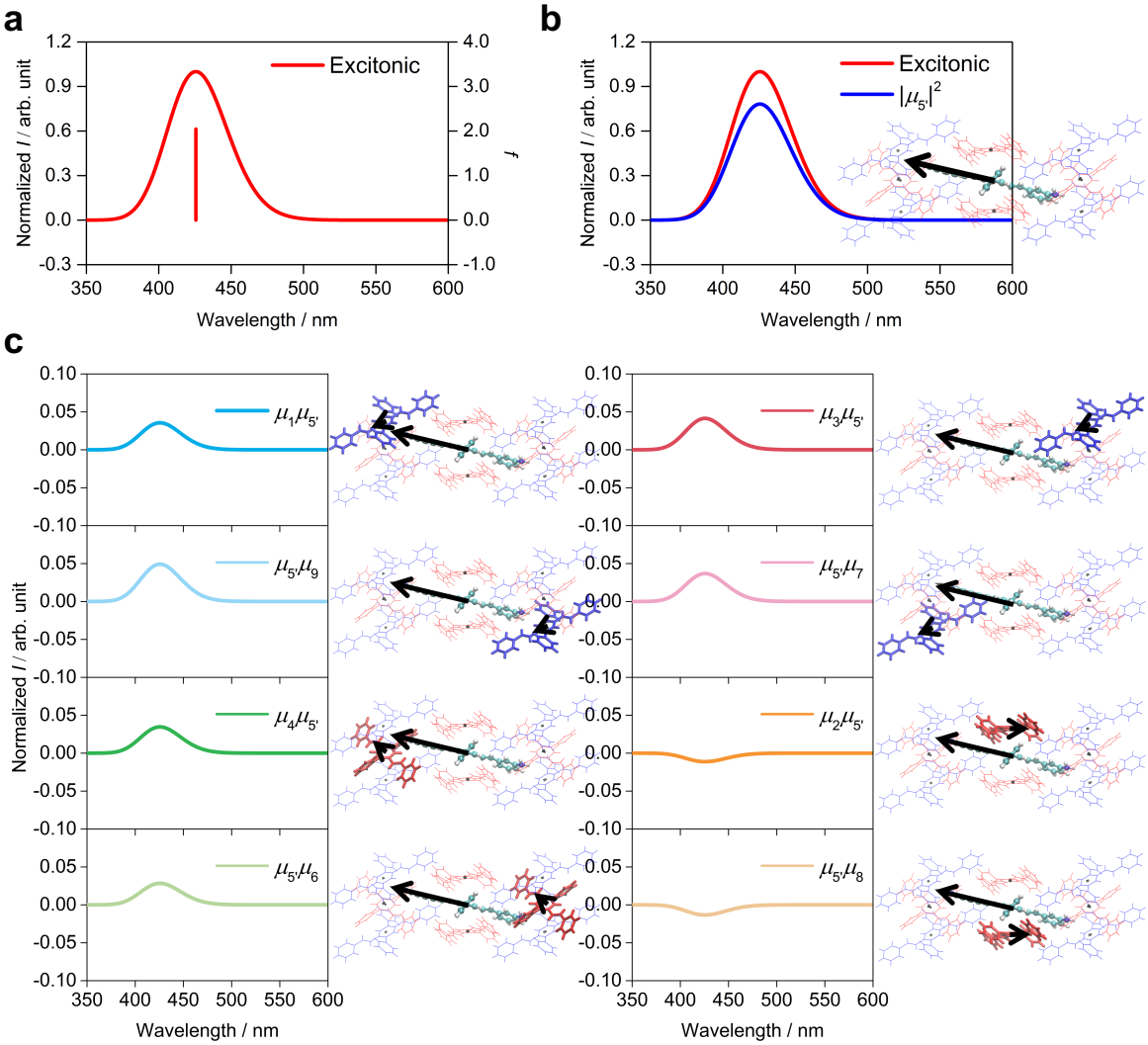

Figure 3.S18. a) Emission spectrum of the asymmetric multichromophoric system and b, c) FEDA results. Only corresponding chromophores with the exciton electric transition dipole moments for the decomposed spectra are represented in the licorice models with the bold bonds. The stick represents the oscillator strength.

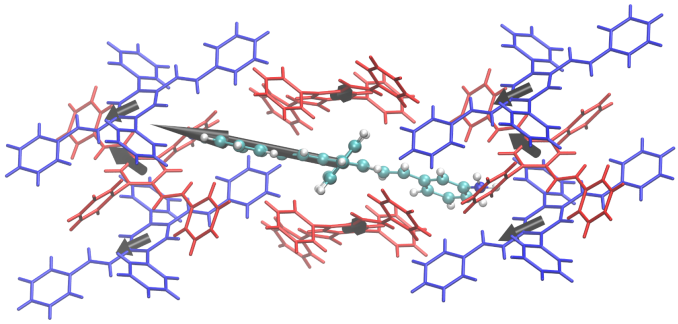

Figure 3.S19. Exciton electric transition dipole moments of the chromophores constituting the asymmetric multichromophoric system for the emissive process. The transition dipole moment of central chromophore **5'** is scaled by 1/6.

References

[1] E. Peeters, M. P. T. Christiaans, R. A. J. Janssen, H. F. M. Schoo, H. P. J. M. Dekkers, E. W. Meijer, *J. Am. Chem. Soc.*, **1997**, *119*, 9909–9910.

[2] M. Schadt, *Annu. Rev. Mater. Sci.*, **1997**, *27*, 305–379.

[3] Y. Yang, R. C. da Costa, M. J. Fuchter, A. J. Campbell, *Nat. Photonics*, **2013**, *7*, 634.

[4] Y. Yang, R. C. da Costa, D.-M. Smilgies, A. J. Campbell, M. J. Fuchter, *Adv. Mater.*, **2013**, *25*, 2624–2628.

[5] F. Zinna, U. Giovanella, L. D. Bari, *Adv. Mater.*, **2015**, *27*, 1791–1795.

[6] M. D. Cohen, G. M. J. Schmidt, *J. Chem. Soc.*, **1964**, *1996*.

[7] A. G. Schultz, A. G. Taveras, R. E. Taylor, F. S. Tham, R. K. Kullnig, *J. Am. Chem. Soc.*, **1992**, *114*, 8725–8727.

[8] A. Nakamura, Y. Inoue, *J. Am. Chem. Soc.*, **2003**, *125*, 966–972.

[9] M. Yoshizawa, S. Miyagi, M. Kawano, K. Ishiguro, M. Fujita, *J. Am. Chem. Soc.*, **2004**, *126*, 9172–9173.

[10] M. Yamashina, Y. Sei, M. Akita, M. Yoshizawa, *Nat. Commun.*, **2014**, *5*, 4662.

[11] V. Ramamurthy, S. Gupta, *Chem. Soc. Rev.*, **2015**, *44*, 119–135.

[12] V. Ramamurthy, J. Sivaguru, *Chem. Rev.*, **2016**, *116*, 9914–9993.

[13] H. Yonezawa, S. Tashiro, T. Shiraogawa, M. Ehara, R. Shimada, T. Ozawa, M. Shionoya, *J. Am. Chem. Soc.*, **2018**, *140*, 16610–16614.

[14] A. Okamoto, *Chem. Soc. Rev.*, **2011**, *40*, 5815–5828.

[15] J. Hall, T. Renger, R. Picorel, E. Krausz, *Biochim. Biophys. Acta, Bioenerg.*, **2016**, *1857*, 115–128.

[16] J. Hall, T. Renger, F. Müh, R. Picorel, E. Krausz, *Biochim. Biophys. Acta, Bioenerg.*, **2016**, *1857*, 1580–1593.

[17] Y. Imai, Y. Nakano, T. Kawai, J. Yuasa, *Angew. Chem. Int. Ed.*, **2018**, *57*, 8973–8978.

[18] P. Reiné, A. M. Ortuño, S. Resa, L. Álvarez de Cienfuegos, V. Blanco, M. J. Ruedas-Rama, G. Mazzeo, S. Abbate, A. Lucotti, M. Tommasini, S. Guisán-Ceinos, M. Ribagorda, A. G. Campaña, A. Mota, G. Longhi, D. Miguel, J. M. Cuerva, *Chem. Commun.*, **2018**, *54*, 13985–13988.

[19] J. Andréasson, U. Pischel, *Chem. Soc. Rev.*, **2018**, *47*, 2266–2279.

[20] E. Mattia, S. Otto, *Nat. Nanotechnol.*, **2015**, *10*, 111.

[21] A. Sorrenti, J. Leira-Iglesias, A. J. Markvoort, T. F. A. de Greef, T. M. Hermans, *Chem. Soc. Rev.*, **2017**, *46*, 5476–5490.

[22] O. Ohmori, M. Kawano, M. Fujita, *Angew. Chem. Int. Ed.*, **2005**, *44*, 1962–1964.

[23] O. Ohmori, M. Kawano, M. Fujita, *Angew. Chem. Int. Ed.*, **2005**, *117*, 1998–2000.

[24] O. Ohmori, M. Kawano, M. Fujita, *CrystEngComm*, **2005**, *7*, 255–259.

[25] N. Yanai, T. Uemura, S. Kitagawa, *Chem. Mater*, **2012**, *24*, 4744–4749.

[26] S. Tashiro, T. Umeki, R. Kubota, M. Shionoya, *Angew. Chem. Int. Ed.*, **2014**, *53*, 8310–8315.

[27] R. B. Merrifield, *J. Am. Chem. Soc.*, **1963**, *85*, 2149–2154.

[28] K. Satoh, S. Ozawa, M. Mizutani, K. Nagai, M. Kamigaito, *Nat. Commun.*, **2010**, *1*, 6.

[29] I.-H. Lee, H. Kim, T.-L. Choi, *J. Am. Chem. Soc.*, **2013**, *135*, 3760–3763.

[30] S. C. Solleder, M. A. R. Meier, *Angew. Chem. Int. Ed.*, **2014**, *53*, 711–714.

[31] J. C. Barnes, D. J. C. Ehrlich, A. X. Gao, F. A. Leibfarth, Y. Jiang, E. Zhou, T. F. Jamison, J. A. Johnson, *Nat. Chem.*, **2015**, *7*, 810.

[32] N. ten Brummelhuis, *Polym. Chem.*, **2015**, *6*, 654–667.

[33] W. Xi, S. Pattanayak, C. Wang, B. Fairbanks, T. Gong, J. Wagner, C. J. Kloxin, C. N. Bowman, *Angew. Chem. Int. Ed.*, **2015**, *54*, 14462–14467.

[34] S. Mochizuki, N. Ogiwara, M. Takayanagi, M. Nagaoka, S. Kitagawa, T. Uemura, *Nat. Commun.*, **2018**, *9*, 329.

[35] S. Mochizuki, T. Kitao, T. Uemura, *Chem. Commun.*, **2018**, *54*, 11843-11856.

[36] M. Kasha, *Radiat. Res.*, **1963**, *20*, 55–71.

[37] J. Cornil, D. A. dos Santos, X. Crispin, R. Silbey, J. L. Brádas, *J. Am. Chem. Soc.*, **1998**, *120*, 1289–1299.

[38] N. J. Hestand, F. C. Spano, *Chem. Rev.*, **2018**, *118*, 7069–7163.

[39] J. B. Birks. Photophysics of Aromatic Molecules; Wiley-Interscience: London, **1970**.

[40] T. Shiraogawa, G. Candel, R. Fukuda, I. Ciofini, C. Adamo, A. Okamoto, M. Ehara, *J. Comput. Chem.*, **2019**, *40*, 127–134.

[41] N. Harada, K. Nakanishi. Circular Dichroic Spectroscopy—Exciton Coupling in Organic Stereochemistry; University Science Books: Mill Valley, CA, 1983.

[42] S. Jurinovich, G. Pescitelli, L. D. Bari, B. Mennucci, *Phys. Chem. Chem. Phys.*, **2014**, *16*, 16407–16418.

[43] S. Jurinovich, C. A. Guido, T. Bruhn, G. Pescitelli, B. Mennucci, *Chem. Commun.*, **2015**, *51*, 10498–10501.

[44] T. Shiraogawa, M. Ehara, S. Jurinovich, L. Cupellini, B. Mennucci, *J. Comput. Chem.*, **2018**, *39*, 931–935.

[45] Z. Xie, B. Yang, F. Li, G. Cheng, L. Liu, G. Yang, H. Xu, L. Ye, M. Hanif, S. Liu, D. Ma, Y. Ma, *J. Am. Chem. Soc.*, **2005**, *127*, 14152–14153.

[46] Z. Xie, W. Xie, F. Li, L. Liu, H. Wang, Y. Ma, *J. Phys. Chem. C*, **2008**, *112*, 9066–

9071.

[47] J.-D. Zhou, W.-Q. Zhang, L.-L. Liu, Z.-Q. Xie, Y.-G. Ma, *Chinese Chem. Lett.*, **2016**, *27*, 1350–1356.

[48] B. Yang, Z. Xie, H. Zhang, H. Xu, M. Hanif, X. Gu, F. He, J. Yu, Y. Ma, J. Shen, X. Liu, J. Feng, *Chem. Phys.*, **2008**, *345*, 23–31.

[49] R. Dennington, T. A. Keith, J. M. Millam. GaussView, Version 6, Semichem Inc.: Shawnee Mission, KS, 2016.

[50] C. A. Guido, S. Knecht, J. Kongsted, B. Mennucci, *J. Chem. Theory Comput.*, **2013**, *9*, 2209–2220.

[51] D. Bousquet, R. Fukuda, P. Maitarad, D. Jacquemin, I. Ciofini, C. Adamo, M. Ehara, *J. Chem. Theory Comput.*, **2013**, *9*, 2368–2379.

[52] D. Bousquet, R. Fukuda, D. Jacquemin, I. Ciofini, C. Adamo, M. Ehara, *J. Chem. Theory Comput.*, **2014**, *10*, 3969–3979.

[53] D. Robinson, *J. Chem. Theory Comput.*, **2018**, *14*, 5303–5309.

[54] T. Yanai, D. P. Tew, N. C. Handy, *Chem. Phys. Lett.*, **2004**, *393*, 51–57.

[55] S. A. Mewes, F. Plasser, A. Dreuw, *J. Phys. Chem. Lett.*, **2017**, *8*, 1205–1210.

[56] A. Muñoz-Losa, C. Curutchet, I. F. Galván, B. Mennucci, *J. Chem. Phys.*, **2008**, *129*, 034104.

[57] B. Mennucci, E. Cancès, J. Tomasi, *J. Phys. Chem. B*, **1997**, *101*, 10506–10517.

[58] J. Tomasi, B. Mennucci, R. Cammi, *Chem. Rev.*, **2005**, *105*, 2999–3094.

[59] R. D. J. Froese, K. Morokuma, *Chem. Phys. Lett.*, **1996**, *263*, 393–400.

[60] T. Vreven, K. Morokuma, *J. Comput. Chem.*, **2000**, *21*, 1419–1432.

[61] L. W. Chung, W. M. C. Sameera, R. Ramozzi, A. J. Page, M. Hatanaka, G. P. Petrova, T. V. Harris, X. Li, Z. Ke, F. Liu, H.-B. Li, L. Ding, K. Morokuma, *Chem. Rev.*,

2015, *115*, 5678–5796.

[62] P. M. Bayley, E. B. Nielsen, J. A. Schellman, *J. Phys. Chem.*, **1969**, *73*, 228–243.

[63] C.-P. Hsu, G. R. Fleming, M. Head-Gordon, T. Head-Gordon, *J. Chem. Phys.*, **2001**, *114*, 3065–3072.

[64] M. F. Iozzi, B. Mennucci, J. Tomasi, R. Cammi, *J. Chem. Phys.*, **2004**, *120*, 7029–7040.

[65] J. Snir, J. Schellman, *J. Phys. Chem.*, **1973**, *77*, 1653–1661.

[66] J. Snir, J. A. Schellman, *J. Chem. Phys.*, **1974**, *78*, 387–392.

[67] T. B. Pedersen, H. Koch, *J. Chem. Phys.*, **2000**, *112*, 2139–2147.

[68] A. E. Hansen, *Manatsh. Chem.*, **2005**, *136*, 253–273.

[69] A. E. Hansen, *Manatsh. Chem.*, **2005**, *136*, 275–287.

[70] D. Lindorfer, T. Renger, *J. Phys. Chem. B*, **2018**, *122*, 2747–2756.

[71] M. J. Frisch, G. W. Trucks, H. B. Schlegel, G. E. Scuseria, M. A. Robb, J. R. Cheeseman, G. Scalmani, V. Barone, G. A. Petersson, H. Nakatsuji, X. Li, M. Caricato, A. V. Marenich, J. Bloino, B. G. Janesko, R. Gomperts, B. Mennucci, H. P. Hratchian, J. V. Ortiz, A. F. Izmaylov, J. L. Sonnenberg, D. Williams-Young, F. Ding, F. Lipparini, F. Egidi, J. Goings, B. Peng, A. Petrone, T. Henderson, D. Ranasinghe, V. G. Zakrzewski, J. Gao, N. Rega, G. Zheng, W. Liang, M. Hada, M. Ehara, K. Toyota, R. Fukuda, J. Hasegawa, M. Ishida, T. Nakajima, Y. Honda, O. Kitao, H. Nakai, T. Vreven, K. Throssell, J. A. Montgomery, Jr., J. E. Peralta, F. Ogliaro, M. J. Bearpark, J. J. Heyd, E. N. Brothers, K. N. Kudin, V. N. Staroverov, T. A. Keith, R. Kobayashi, J. Normand, K. Raghavachari, A. P. Rendell, J. C. Burant, S. S. Iyengar, J. Tomasi, M. Cossi, J. M. Millam, M. Klene, C. Adamo, R. Cammi, J. W. Ochterski, R. L. Martin, K. Morokuma, O. Farkas, J. B. Foresman, D. J. Fox. Gaussian, Inc.: Wallingford, CT, 2016.

[72] S. Jurinovich, C. A. Guido, L. Cupellini, B. Mennucci, *J. Comput. Chem.*, **2018**, *39*, 279–286.

[73] W. Humphrey, A. Dalke, K. Schulten, *J. Molec. Graphics*, **1996**, *14*, 33–38.

[74] A. D. Becke, *J. Chem. Phys.*, **1993**, *110*, 6158–6170.

[75] Z. Xie, B. Yang, W. Xie, L. Liu, F. Shen, H. Wang, X. Yang, Z. Wang, Y. Li, M. Hanif, G. Yang, L. Ye, Y. Ma, *J. Phys. Chem. B*, **2006**, *110*, 20993–21000.

[76] S. Caprasecca, S. Corni, B. Mennucci, *Chem. Sci.*, **2018**, *9*, 6219–6227.

Chapter 4

Theoretical Design of Photofunctional Molecular Aggregates for Optical Properties: An Inverse Design Approach

4.1. Introduction

Molecular aggregates have various photofunctions and in particular, optical properties of the aggregates drastically change depending on their structure and composition. Photo-absorption is an essential property for photo-induced processes and functions such as photochemical reactions, emission, circularly polarized luminescence, and excitation energy transfer. Circular dichroism (CD), which is the differential absorption between left and right circularly polarized light, is a characteristic optical property of chiral molecules and has been used to probe their absolute structure in the wide field of chemistry and biology. The CD also has practical importance for applications in chiral photoswitches,[1,2] high-resolution sensings,[3,4] absolute asymmetry synthesis,[5,6] and information processing. Various photofunctional molecular aggregates have been developed aiming at the control of the photoabsorption and CD. In this field, the design guidelines are indispensable to accelerate the development of efficient optical materials.

The immense chemical diversity of molecules offers the vast potential to the design of the photofunctional molecular aggregates. Molecular aggregates can be identified by their constituent molecules and structures. These elements determine the properties of the systems and therefore must be controlled to create the molecular aggregate with desired functions. To this end, various experimental strategies such as nonequilibrium and programmable self-organization,[7-10] simultaneous arrangement on a porous crystal,[11-14] and controlled polymerization strategies[15-18] have been developed in the field of supramolecular chemistry. Although the current application scope of these techniques is still limited, it is promising to create the system having arbitrary composition and structure in the future. However, for rational

implementation of this strategy, *a priori* knowledge of the structure and composition of the designed system with the desired properties is required. The purpose of this work is to present a useful method to search for photofunctional molecular aggregates whose existence is not revealed and to provide insight into their design.

There are two molecular design approaches; direct and inverse design.[19-21] The direct design is a material-dependent approach and driven by knowledge and findings in existing systems. For example, as the direct design, the author proposed a post-modification strategy of optical properties of molecular aggregates based on the calculation and analysis of a given system.[22] On the other hand, the inverse design is to predict molecular systems from target properties. Complementary to the direct design approach, *a priori* optimal design of photofunctional molecular aggregates by the inverse approach, as well as advances in the experimental techniques, is demanded for rational discoveries of novel photofunctional systems. Various applications of the inverse design have been reported in the field of nanophotonics.[23] The inverse design approach for molecular systems is of fundamental importance in the development of such optical devices.

The inverse design based on chemical space, a set of all possible molecular systems varying in the composition, size, and structure, has recently been intensively studied.[19-21,24-29] The inverse design uses information of target functional space for discovering molecular systems with desired properties in the chemical space. In this context, a straightforward way of the design is experimental or computational screening of all the candidates in the chemical space. However, such direct design is not effective for the large chemical space because the processing capacity easily reaches to its limit. Instead of the screening, it is possible to optimize the molecular

system in the chemical space.[30] For theoretical representation of this inverse design, the variational particle approach[31,32] and the linear combination of atomic potentials (LCAP)[24] were proposed. These methods enable us to continuously map the chemical space based on the *ab initio* computation method and utilize the gradient-guided search for efficiently designing systems. The huge computational costs of the *ab initio* methods hinder these applications to the large chemical space. To overcome this problem, the LCAP was implemented using the semi-empirical AM1, Hückel, and extended Hückel methods.[33,34] These LCAP strategies were successfully utilized in the design of nonlinear optical molecules,[24,33-37] inhibitors for redox regulation,[38] dye-sensitized solar cells,[39] molecular catalysts,[40] and catalytic sites on metal surface[41] and in atomic configuration search of alloys.[42]

The Frenkel exciton model has been widely adopted to describe and interpret photophysical phenomena of molecular aggregates, including the absorption and CD. For example, the H- and J-aggregates based on this model are well-known concepts for qualitative interpretation of the absorption spectrum[43,44] and exploited in a biological probe with an on–off switch.[45,46] The exciton chirality method (ECM) is utilized to predict molecular conformational dependence of the CD.[47] Thus, utilizing the Frenkel exciton model is suitable for molecule-based inverse design of photofunctional molecular aggregates for those optical properties. Moreover, based on the Frenkel exciton model, multiscale modelling approaches for various photo-induced processes have been developed.[48] The inverse design method provides a promising basis for designing various photofunctional composite systems.

In this work, the author develops an inverse design approach for the rational and efficient design of photofunctional molecular aggregates with desired optical

properties based on the Frenkel exciton model coupled with the LCAP framework. The author has applied this method to the design of one-dimensional molecular aggregates with strong absorption and/or CD as an example. Chemical space for the design consists of the possible systems with a variety of molecular species and their structural arrangements. The optimal structure–photofunction relationships were investigated from the designed systems. The author characterized the contributions from each constituent molecule to the optical spectra of the designed systems by using the Frenkel-exciton decomposition analysis (FEDA) method based on the length-form electric transition dipole moments (please see Chapter 2).[49] Based on the finding, the author examined the potential of the photofunctions in the designed systems.

4.2. Methods

Here the author describes the present inverse design method for photofunctional molecular aggregates. The author describes the inverse design based on the LCAP framework[24,34] and the Frenkel exciton model. Then, the chemical space for the present design regarding the constituent molecules and structures of molecular aggregates is described. Finally, the computational details are given.

4.2.1. Frenkel exciton model

The Frenkel exciton model and related notations are summarized in Chapter 2 of this thesis. The absorption and CD spectra can be represented as the absorption coefficient (ε) and the molar CD ($\Delta\varepsilon$), respectively. The details of the simulation of these spectra are given in Supporting Information.

4.2.2. Inverse design approach for photofunctional molecular aggregates

The author couples the Frenkel exciton model with the LCAP framework to continuously interpolate discrete chemical space of possible molecular aggregates based on spatially arranged molecules. This allows us to compute derivatives of target properties with respect to the chemical space and to utilize gradient-based optimization techniques for the design. In the density functional theory (DFT), the external (electron–nuclear attraction) potential which is defined by the atomic types and positions determines the Hamiltonian of a molecule. Thus, the external potential is the variables of molecular properties and needs to be optimized to design the system. In the LCAP, the external potential of an atom (or chemical group) is expanded as a linear combination of atomic potentials (or collection of these potentials).[24] The author follows the tight-binding LCAP approach[34] since the Frenkel exciton model uses the tight-binding Hamiltonian.

Molecules are also the design variables of a molecular aggregate. For the continuous representation of the molecular aggregate in the chemical space, the author represented the constituent molecule as an admixture of the candidate molecules by the linear combination with participation coefficients $\left\{b_i^{(A)}\right\}$ indicating these probability weights. The inverse design approach is implemented introducing the following Frenkel exciton Hamiltonian:

$$\begin{aligned}\hat{H}_{\mathrm{ID}} = &\sum_{i}^{N}\sum_{a}^{n_i}\sum_{A}^{N_i^{\mathrm{type}}} b_i^{(A)}\varepsilon_{ia}^{(A)}\left|ia_{\mathrm{ID}}^{\mathrm{agg}}\right\rangle\left\langle ia_{\mathrm{ID}}^{\mathrm{agg}}\right| \\ &+\sum_{i\neq j}^{N}\sum_{a,b}^{n_i,n_j}\sum_{A,B}^{N_i^{\mathrm{type}},N_j^{\mathrm{type}}} b_i^{(A)}b_j^{(B)}V_{ia,jb}^{(A,B)}\left|ia_{\mathrm{ID}}^{\mathrm{agg}}\right\rangle\left\langle jb_{\mathrm{ID}}^{\mathrm{agg}}\right|\end{aligned} \tag{1}$$

where the subscript "ID" denotes the inverse design. $b_i^{(A)}$ is the participation coefficient for the Ath candidate molecule with the possible spatial arrangement at the molecular site i. $\varepsilon_{ia}^{(A)}$ is the excitation energy of the candidate molecule A at the site i. $V_{ia,jb}^{(A,B)}$ is the exciton coupling between the molecules A at the site i and B at the site j. Constrains on $b_i^{(A)}$ are $\sum_A^{N_i^{\text{type}}} b_i^{(A)} = 1$ and $0 \le b_i^{(A)} \le 1$ because there is a single molecule at the molecular site i, *i.e.*, the Hamiltonian corresponds to the system in the continuous chemical space. Thus, the Hamiltonian of the total system varies continuously over the chemical space, and the inverse design of the system reduces to the optimization of the participation coefficients. The alchemical states with the participation coefficients in $0 < b_i^{(A)} < 1$ have the admixtures of the candidate molecules. Such the nonphysical systems between the possible ones lie in the continuous chemical space. Therefore, after the optimization through the alchemical states, it is necessary to convert the participation coefficients from non-integer to integer in order to finally obtain the nearest possible system as the designed one. The round-off value of the participation coefficients must satisfy the condition $\sum_A^{N_i^{\text{type}}} b_i^{(A)} = 1$ imposed on the designed system to have the Hamiltonian of the actual system. The author notes that it is generally difficult to efficiently perform the simulated annealing under the condition $b_i^{(A)} = 1$ for the combinatorial optimization because of the difficulties in defining the neighborhood needed to adjust the transition probabilities for the change of molecular species.

The matrix elements of the Frenkel exciton Hamiltonian of the molecular aggregate in the continuous chemical space are weight-averaged over the candidate molecules (equation (1)). Diagonalization of the Hamiltonian matrix provides the exciton energies and the exciton coefficients $\left\{C^K_{ia,\mathrm{ID}}\right\}$ with respect to the given participation coefficients. For the actual system whose participation coefficients are 0 or 1 at all the molecular sites, the Hamiltonian matrix is identical with that of the original Frenkel exciton model, and the optical properties can be computed as described in Chapter 2 and Supporting Information of this thesis. Under the assumption that the Hamiltonian defined in equation (1) is of the Frenkel exciton model across the entire continuous chemical space, the exciton electric transition dipole moment (ETDM) $\boldsymbol{\mu}_{0K,\mathrm{ID}}$ and magnetic transition dipole moment (MTDM) $\boldsymbol{m}_{0K,\mathrm{ID}}$ can be expressed as those of the actual molecular aggregates: $\boldsymbol{\mu}_{0K,\mathrm{ID}} = \sum_i^N \sum_a^{n_i} C^K_{ia,\mathrm{ID}} \boldsymbol{\mu}_{i0a,\mathrm{ID}}$ and $\boldsymbol{m}_{0K,\mathrm{ID}} = \sum_i^N \sum_a^{n_i} C^K_{ia,\mathrm{ID}} \boldsymbol{m}_{i0a,\mathrm{ID}}$. Here $\boldsymbol{\mu}_{i0a,\mathrm{ID}}$ and $\boldsymbol{m}_{i0a,\mathrm{ID}}$ are the ETDM and MTDM at the molecular site *i* for the *a*th excited state, respectively. To compute optical properties with $\boldsymbol{\mu}_{0K,\mathrm{ID}}$ and $\boldsymbol{m}_{0K,\mathrm{ID}}$ for the inverse design, $\boldsymbol{\mu}_{i0a,\mathrm{ID}}$ and $\boldsymbol{m}_{i0a,\mathrm{ID}}$ need to be evaluated for all the possible values of the participation coefficients. Therefore, as with the Hamiltonian matrix elements, the author represents $\boldsymbol{\mu}_{i0a,\mathrm{ID}}$ and $\boldsymbol{m}_{i0a,\mathrm{ID}}$ as the weighted averages of the TDMs of the candidate molecules with the participation coefficients:

$$\boldsymbol{\mu}_{i0a,\mathrm{ID}} = \sum_A^{N_i^{\mathrm{type}}} b_i^{(A)} \boldsymbol{\mu}_{i0a(A)} \tag{2}$$

$$\boldsymbol{m}_{i0a,\mathrm{ID}} = \sum_{A}^{N_i^{\mathrm{type}}} b_i^{(A)} \boldsymbol{m}_{i0a(A)} \tag{3}$$

where $\boldsymbol{\mu}_{i0a(A)}$ and $\boldsymbol{m}_{i0a(A)}$ are the ETDM and MTDM of the candidate molecule *A* at the site *i* for the *a*th excited state, respectively. Here the participation coefficients are the same as those in the Hamiltonian used to obtain the exciton energies and the exciton coefficients. $\boldsymbol{\mu}_{i0a,\mathrm{ID}}$ and $\boldsymbol{m}_{i0a,\mathrm{ID}}$ are equal to those of the candidate molecules at $b_i^{(A)} = 1$, and $\boldsymbol{\mu}_{0K,\mathrm{ID}}$ and $\boldsymbol{m}_{0K,\mathrm{ID}}$ are identical to $\boldsymbol{\mu}_{0K}$ and $\boldsymbol{m}_{0K}$ of the original Frenkel exciton model, respectively, in the actual designed molecular aggregates. The rotatory strength, absorption coefficient, and molar CD for the inverse design are computed from the obtained photophysical properties as described in equations (S1) and (S2) in Supporting Information.

The author analyzes the absorption and CD spectra of the designed systems by using the FEDA method[49] based on the excitonic approach to simulate the optical properties.[50] The details of the FEDA can be found in Supporting Information. A simplified flowchart of the present inverse design strategy is shown in Figure 4.1. It is also possible to obtain the parameters of the exciton Hamiltonian and photophysical properties of the molecules from experimental data.

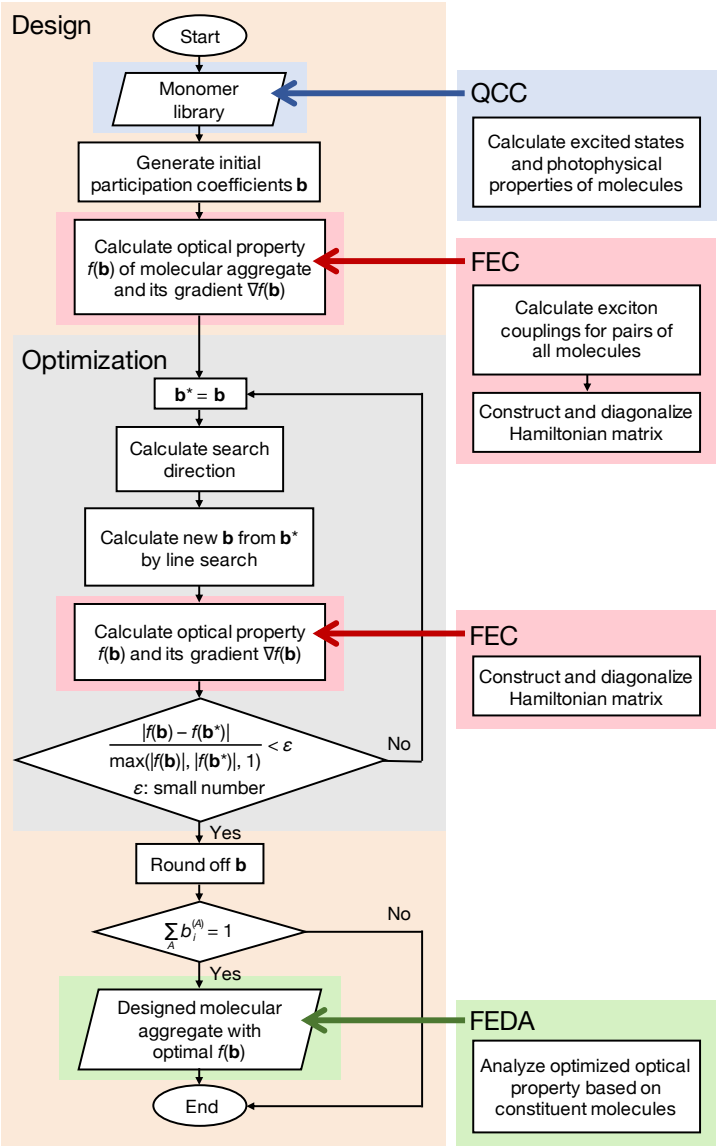

Figure 4.1. Simplified flowchart of inverse design of a photofunctional molecular aggregate for optical properties. QCC: Quantum Chemistry Calculation. FEC: Frenkel Excitonic Calculation. FEDA: Frenkel-Exciton Decomposition Analysis.

4.2.3. Chemical space

The author has designed molecular aggregates (Figure 4.2) in which molecules are one-dimensionally stacked in this work. For the candidate molecules constituting the systems, the author examined *trans*-stilbene and its five derivatives (Figure 4.2).

Trans-stilbene is a structural dimer of poly(paraphenylenevinylene), PPV,[51] which shows strong emission and is important for electric optical devices. It is also a common backbone of stilbenoids having various bioactivities.[52] Such π-conjugated planar organic molecules tend to form a co-facial stacking structure in the aggregate due to the π–π interaction, and the one-dimensional arrangement of molecules is a typical structure of multichromophoric systems. Recently, it is becoming possible to control the molecular stacking structure and constituent molecules by chemical modification, manipulation of the aggregation processes,[8-10] and sequence control of functional groups of polymers.[15-18] Therefore, this work has focused on the design of the one-dimensional molecular aggregates with the tailored molecular rotation angles (Figure 4.2). In the aggregates, the molecules are stacked in the co-facial arrangements separated by 4 Å and have a degree of freedom in the rotation from 0° to 360° with the change of 3° around the stacked axis. At the rotation angle of 0°, the central ethylene units of the candidate molecules are arranged in parallel. The mass centers of the constituent molecules of the system are located on the stacking axis. To investigate the system size dependence of the photofunctions, the author has designed the molecular dimer, pentamer, and decamer. The numbers of the possible molecular aggregates of the dimer, pentamer, and decamer are $6 \times (2 \times 60 + 4 \times 120) = 3.6 \times 10^3$, $6 \times (2 \times 60 + 4 \times 120)^4 \approx 7.8 \times 10^{11}$, and $6 \times (2 \times 60 + 4 \times 120)^9 \approx 6.0 \times 10^{25}$, respectively. Even if we evaluate the possible system in nanoseconds, the screening of all the possible decamers takes about two billion years, which means its implementation is practically impossible.

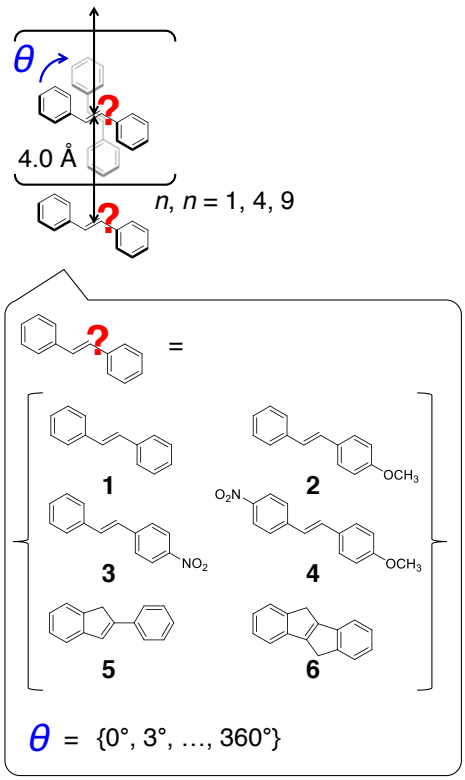

Figure 4.2. Schematic representation of possible one-dimensional molecular aggregates composed of *trans*-stilbene and its five derivatives (**1**–**6**). **1**: *trans*-stilbene. **2**: *trans*-4-methylstilbene. **3**: *trans*-4-nitrostilbene. **4**: *trans*-4-methyl-4'-nitrostilbene. **5**: 2-phenylindene. **6**: indeno[2,1-*a*]indene.

4.2.4. Computational details

For the exciton coupling, the dipolar form was used, which allows high-throughput calculations of the optical properties. The intense electronic excitation for the first excited state of each candidate molecule is included in the Frenkel exciton Hamiltonian. The author carefully examined the accuracy of the exciton model in comparison with the linear-response time-dependent (TD-) DFT results of the dimer of **1** (*trans*-stilbene) calculating fifteen excited states. For half the bandwidth at 1/*e* peak height of the Gaussian of the optical spectra in equations (S1) and (S2), the author employed 0.25 eV.

The geometries of the candidate molecules were optimized at the B3LYP functional[53] with the 6-31G(d) basis set. The photophysical properties of the monomers were calculated using the TD-DFT with the CAM-B3LYP[54]/6-311+G(d) level of theory. The accuracy of the TD-DFT for the photophysical properties of small organic molecules has been well assessed by the systematic benchmark calculations.[55-57] The ETDM is one of the key properties of the exciton model employed in this work; the systematic benchmark study showed that the CAM-B3LYP functional performs well for the ETDM.[57] All the electronic state calculations for the molecular monomers were performed using Gaussian 16 version B program suite.[58] The excitonic calculations were conducted using our originally developed program. The molecular structures were drawn with VMD.[59]

The author employed the quasi-Newton method with the limited-memory Broyden–Fletcher–Goldfarb–Shanno (L-BFGS) algorithm[60] for the continuous optimization of the participation coefficients because of its applicability to large-scale optimization problems. The author used the Fortran module L-BFGS-B version Lbfgsb.3.0[61,62] for the L-BFGS. The target properties of the design are the positive maximum of the absorption coefficient, molar CD, and both of them. The maximum values of the absorption and CD spectra were obtained by the golden section search method.[63] For the simultaneous optimization of the absorption and CD, the author represented the target function as the equal-weighted average of these maximum positive values. For each design, ten sets of the design were performed using the different randomized initial participation coefficients. The random numbers were generated using the Mersenne Twister with the standard implementation MT19937.[64]

The inverse design was performed using a homemade code. More information on the optimization is provided in Supporting Information.

4.3. Results and Discussion

Since the design results depend on the computational method, the author initially evaluated the accuracy of the design objective function calculated using the Frenkel exciton model. The optimized structures of the candidate molecules (**1**–**6**) in the ground state with the ETDMs for the first excited state are shown in Figure 4.S1. These excited states are characterized as the π–π* excitation by the molecular orbitals relevant to the transitions (Figure 4.S2). The author employed molecular dimers of **1** with the various conformations to examine the accuracy of the Frenkel exciton model and the proposed design method. A simplified model of the molecular aggregate to be investigated (Figure 4.1) was adopted for this purpose as shown in Figure 4.S3. First, the maximum absorption and CD intensities on the various conformations of the model by the excitonic calculation were compared with those of the TD-DFT. Figure 4.S4 shows the torsion angle dependence of the maximum absorption and CD by the TD-DFT and excitonic calculations. The Frenkel exciton model qualitatively reproduced the TD-DFT results. The bright excitation of the dimer in the H-aggregate (the torsion angle is 0 and 180° in the adopted model) is blue-shifted compared to the monomer,[43] which leads to the large absorption coefficient due to the difference in the excitation energy as shown in equation (S1). In the design for the strong CD, the author obtained the dimer structure with a torsion angle of 60°. According to the ECM,[47] molecular dimers with the left-handed twisted structure have a positive Cotton effect in the short-wavelength region. Moreover, equation (S2) indicates the linear dependence of the CD intensity

with the excitation energy; the obtained structure has the largest positive CD intensity. The present computational results are consistent with these qualitative interpretations. Next, the author examined the performance of the inverse design approach. The structures with the strongest absorption and CD (Figure 4.S5) are successfully designed by the proposed method (Figure 4.3). Based on these assessments, the present design scheme was validated.

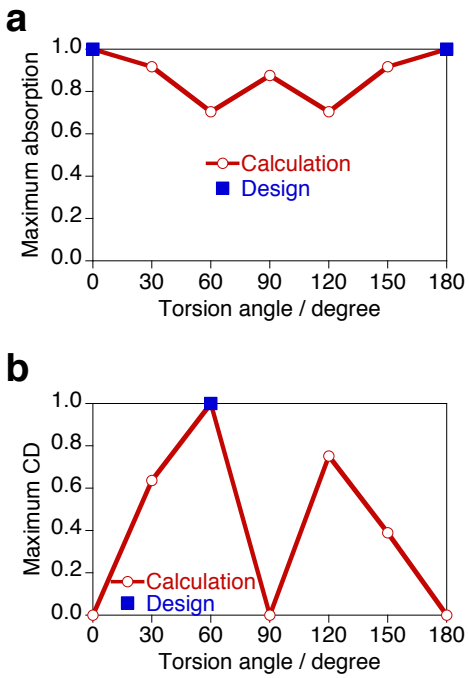

Figure 4.3. Design results of **1** dimers (blue squares) on torsion angle dependence of maximum positive a) absorption and b) CD intensities calculated by the Frenkel exciton model (circles with red outline). The absorption and CD intensities are normalized based on the obtained maximum.

The author has designed the one-dimensional molecular dimers, pentamers, and decamers with strong absorption and/or CD. The inverse design approach was applied

with the continuous optimization scheme to update the molecular aggregate in the chemical space. The author performed ten trials of the design with the randomized initial conditions for each design. All the optimizations successfully converged. Among the ninety trials in all the design of three aggregates for three target properties, most of the locally optimized systems yielded the possible systems after rounding the optimized participation coefficients, while only two attempts of the dimer design for the strong CD failed to obtain the actual system. The author additionally performed two trials of that design for the consistent comparison with the other results and successfully obtained the candidate systems. Figure 4.S6 shows the histograms of all the locally optimized objective functions. The local optima for the CD have a wide range of values compared with the other objective functions. The continuous optimization which uses the property gradient is more efficient than the non-gradient methods and gives optimality to the results. As shown in Figure 4.S6, the local optima located on the property surface depend on the chemical space and provide difficulties for the search of the global optimum. Since the chemical space must be composed of the possible candidates, the author refers to the obtained system with the best target property as the designed system in this work. The optimization histories of the designed systems are shown in Figure 4.S7. The objective functions are sufficiently smooth as a function of the participation coefficients. The optimization in all the design completed within a thousand optimization steps with the moderate convergence criteria. The numbers of the evaluated systems during the design are about 7, 4×10^{-8}, and 1×10^{-21}% of all the possible systems of the dimer, pentamer, and decamer, respectively, which clearly indicates the effectiveness of the inverse design.

The designed systems with the locally maximized absorption intensity have the H-aggregate structure (Figure 4.4). The constituent molecules and structural parameters of the designed systems are summarized in Tables 4.S1–S3. Whereas the candidate molecules for the design are *trans*-stilbene and its five derivatives (**1**–**6**), the designed dimer and pentamer are composed of only the derivative **4** and have the homogeneous aggregate composition. On the other hand, the decamer is composed of two different types of molecules; the molecules at the edge of the stacking are **2** and the others are **4**. This result indicates the importance of heterogeneous aggregate composition systems and control of molecular species for the strong absorption in large molecular systems. Figure 4.5 shows the absorption spectra of the designed dimer, pentamer, and decamer. As the number of the constituent molecules increases, the maximum absorption peak shifts to the shorter wavelength region, enhancing the intensity. This is possibly because the absorption intensity increases as the excitation energy (equation (S1)). Following Ref. [65], the author examined the absorption strength distribution across the entire excitation energy region. The analysis results are shown in Supporting Information.

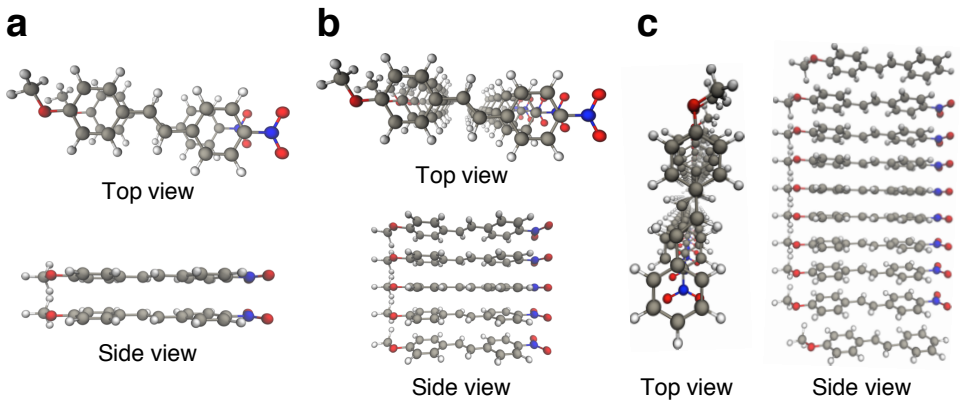

Figure 4.4. Designed a) dimer, b) pentamer, and c) decamer with locally maximized maximum absorption intensity.

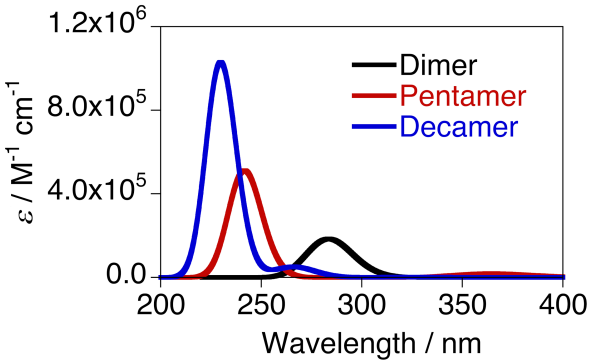

Figure 4.5. Absorption spectra of designed systems with locally maximized maximum absorption intensity.

The designed systems for the strong CD have a left-handed helical structure and are composed of only the derivative **4** (Figure 4.6). The torsion angle in the molecular stacking becomes smaller as the number of the constituent molecules increases (see Tables 4.S1–S3). The author found that the torsion angles of the pentamer and decamer are non-uniform and relatively small at the edge of the stacking structure. These results suggest that precise orientation control of the constituent molecules is essential for developing designed structures having strong CD. Figure 4.7 displays the CD spectra of the designed systems. All the CD spectra show the negative first and positive second Cotton effects. Similar to the case of strong absorption, the increase in the number of the constituent molecules results in the shift of the strongest positive CD peak to the shorter wavelength possibly because of the positive dependence of the CD intensity on the excitation energy (see equation (S2)).

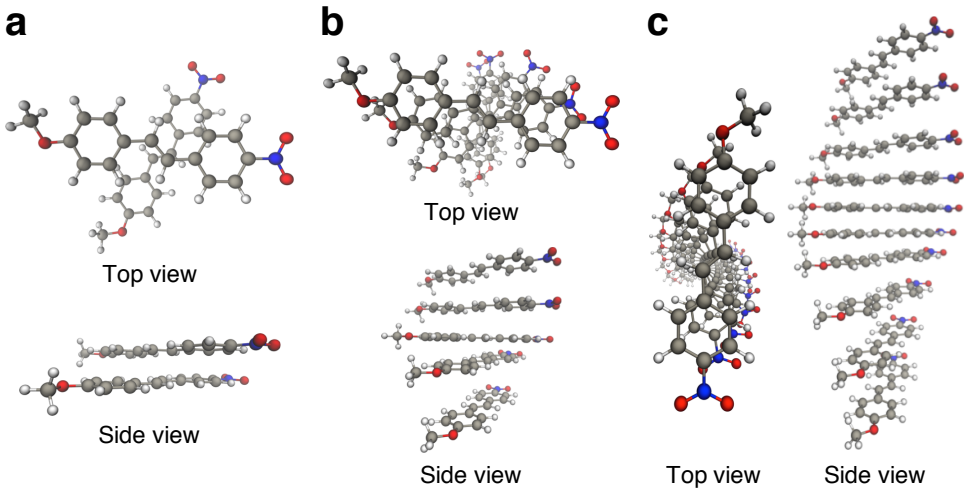

Figure 4.6. Designed a) dimer, b) pentamer, and c) decamer with locally maximized maximum CD intensity.

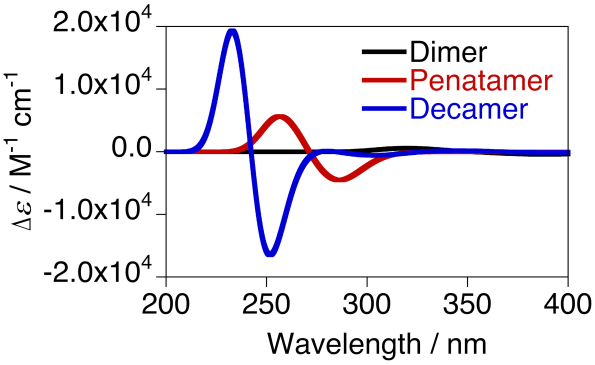

Figure 4.7. CD spectra of designed systems with locally maximized maximum CD intensity.

The author investigated the system size dependence on the target photofunctions of the designed systems in more detail. Figure 4.8 shows the relative intensities of the locally maximized maximum absorption and CD of the designed systems. The maximum absorption intensity increases almost additively in proportion to the number

of the constituent molecules, while the maximum CD intensity is significantly enhanced in a non-additive manner. This finding suggests that the creation of the appropriate aggregate structure proposed by the design is particularly important for the strong CD of large molecular systems.

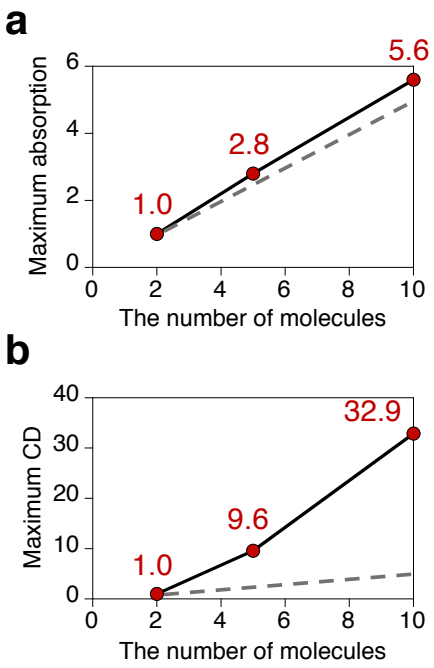

Figure 4.8. System size dependence of locally maximized maximum a) absorption and b) CD intensities of designed systems. The red dots are the maximum absorption and CD. The gray dashed lines represent linear increases in these properties.

The author analyzed the absorption and CD spectra of the designed systems by using the FEDA method. In the FEDA, the optical spectra are directly decomposed into the spectra corresponding to the physical and chemical natures of the constituent molecules. Figures 4.S8–S12 show the decomposed spectra with the contributions of the constituent molecules. The author found that the CD of the designed systems only

originates in the interactions of the exciton ETDMs of the molecules, $\mu_i\mu_j$, where the indices *i* and *j* of the molecules are in the order of the stacking. In the stacking structure, the ETDMs of all the candidate molecules are perpendicular to the MTDMs. Consequently, the interaction of the exciton ETDM and MTDM has no contributions to the CD. The FEDA revealed that all the decomposed spectra have positive contributions to the peak with the maximum absorption or CD intensity, which indicates that the potential of the photofunctions is sufficiently utilized in the designed systems. On the other hand, those partially or completely cancel out each other in the other energy region.

The author also designed the one-dimensional molecular aggregates with both of the strong absorption and CD to demonstrate the potential utilities of the inverse design. The designed dimer and pentamer are the same as the systems obtained in the design for the strong absorption, H-aggregate. Figure 4.S13 shows the designed decamer. The designed decamer has the identical aggregate composition to the system for the absorption, while there is small torsion in the central region of the stacking (see Table 4.S3). In this manner, once the target optical properties are determined, it is possible to perform the design of the system.

4.4. Conclusions

The author proposed an inverse design approach of photofunctional molecular aggregates for optical properties based on the Frenkel exciton model and LCAP framework. In this approach, the constituent molecule of the system is represented as an admixture of the candidate molecules for the design. This allows for the efficient gradient-based optimization search of the optimal systems in chemical space

composed of possible molecular aggregates varying in the constituent molecules and the structure. The present method has been applied to design one-dimensional molecular aggregates with strong absorption and/or CD in the chemical space including various candidate molecules and their spatial arrangements. The author successfully proposed the promising molecular components and aggregate structure by evaluating only a small faction (10^2–10^3) of the entire chemical space of up to about 10^{26}. The designed systems with the locally maximized absorption intensity have the H-aggregate structure. It was found that the designed decamer has the heterogeneous aggregate composition. The strong CD can be obtained in the left-handed helical structure with the non-uniform torsion angles and the homogeneous aggregate composition. The resulting systems indicate that the design and fine engineering of molecular aggregates with respect to the structure and composition are important to realize the desired optical properties. The author also clarified that the CD can be nonlinearly increased by designing and creating appropriate molecular arrangements and increasing the number of constituent molecules. The author showed that the potential of the photofunctions is sufficiently utilized in the designed systems by using the FEDA method, which also contributes to the acceleration of the search. Furthermore, the applicability of the present approach was demonstrated by the design of the system with both the strong absorption and CD. In light of advances in supramolecular chemistry, the present inverse design approach is useful for the investigation of optimal structure–photofunction relationships and the acceleration of discoveries of high-performance optical materials.

Supporting Information

Optimization

In the inverse design of this work, the participation coefficients must be optimized under the conditions $\sum_{A}^{N_i^{\text{type}}} b_i^{(A)} = 1$ and $0 \le b_i^{(A)} \le 1$. It is possible to convert the constrained optimization problem into an unconstrained one by using the following expression of the participation coefficients:[24]

$$b_i^{(A)} = \frac{\left(t_i^{(A)}\right)^2}{\sum_{A}^{N_i^{\text{type}}} \left(t_i^{(A)}\right)^2}$$

where the constraints on $b_i^{(A)}$ are automatically satisfied. The arbitrary real numbers $\left\{t_i^{(A)}\right\}$ were optimized instead of $\left\{b_i^{(A)}\right\}$.

For the stop condition of the L-BFGS optimization, the author employed the moderate convergence criterion of 2.20×10^{-9} for the continuous search (see Figure 4.1). The quasi-Newton method uses the gradient of the target property to update the molecular aggregate in the inverse design. The author employed the forward finite-difference formula for the numerical differential of the target optical properties with a small number of 10^{-5}.

The target properties of the design are the maximum positive values of the absorption and CD spectra. The author initially estimated the peak with the positive maximum absorption or CD intensity in the simulated spectrum with sufficient grid points. Then, the golden section search was performed on that peak until the interval of the search becomes sufficiently small.

In the exciton model used in this work, conformational inversion of the monomer around the stacking axis does not affect the optical properties. Thus, the author presents the simple structures of the designed systems for simplicity.

Simulation of absorption and circular dichroism (CD) spectra

The absorption and CD spectra can be represented as the absorption coefficient ε and the molar CD $\Delta\varepsilon$, respectively, and written as follows by using overlapping Gaussian functions for each excitation:

$$\varepsilon(\nu) = \frac{8\pi^3 N_{\mathrm{A}}}{3000hc\ln 10}\frac{1}{\sqrt{\pi}\Delta\nu}\sum_{K}^{M}\nu_{0K}\left|\boldsymbol{\mu}_{0K}\right|^2\exp\left\{-\left(\frac{\nu-\nu_{0K}}{\Delta\nu}\right)^2\right\} \tag{S1}$$

$$\Delta\varepsilon(\nu) = \frac{32\pi^3 N_{A}}{3000hc\ln 10}\frac{1}{\sqrt{\pi}\Delta\nu}\sum_{K}^{M}\nu_{0K}R_{0K}\exp\left\{-\left(\frac{\nu-\nu_{0K}}{\Delta\nu}\right)^2\right\} \tag{S2}$$

where h is the Planck's constant, N_A is the Avogadro's number, ν is the photon energy, $\Delta\nu$ is half the bandwidth at 1/e peak height of the Gaussian, and ν_{0K} is the calculated excitation energy for the transition K←0. The ETDM and rotatory strengths are in esu^2 cm^2.

Results

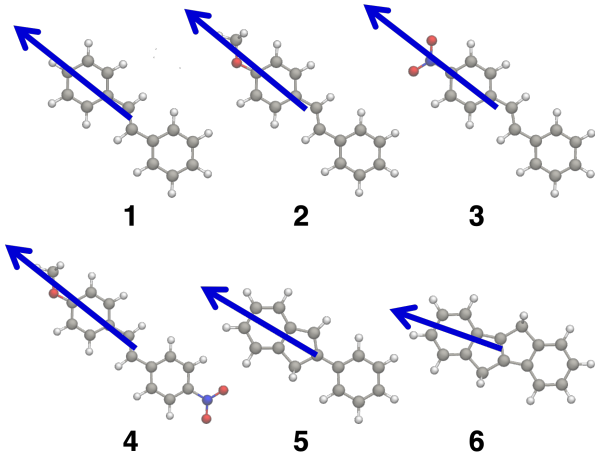

Figure 4.S1. ETDMs of the intense electronic excitation for the first excited state of **1**–**6**. The ETDMs are located on mass centers of the molecules.

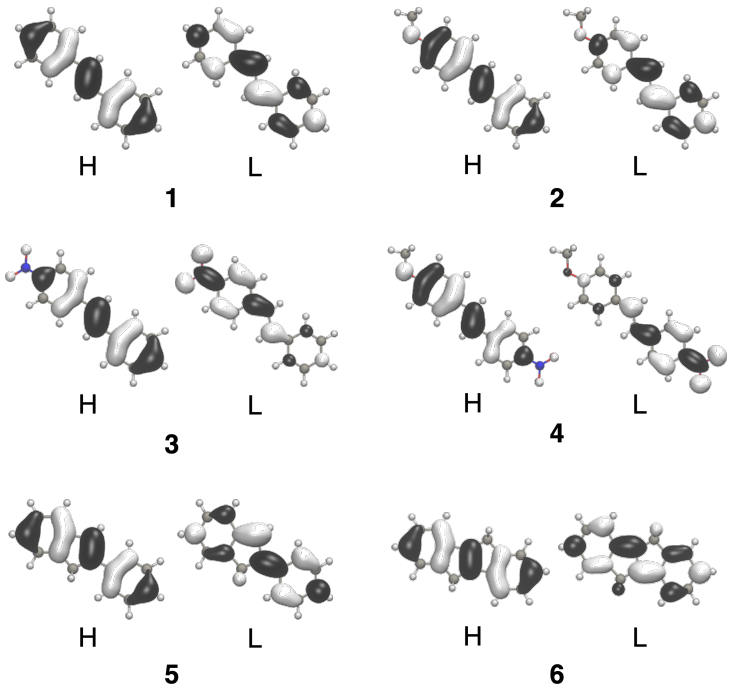

Figure 4.S2. Molecular orbitals of molecules of **1**–**6** (Isovalue = |0.03|). H and L denote the highest occupied molecular orbital and the lowest unoccupied molecular orbital, respectively.

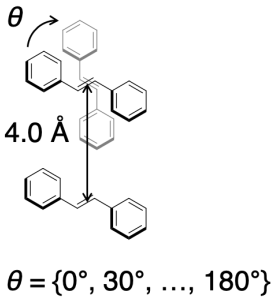

Figure 4.S3. Simplified one-dimensional molecular aggregates composed of **1** with various conformations for examination of accuracy of the Frenkel exciton model and performance of the present inverse design approach.

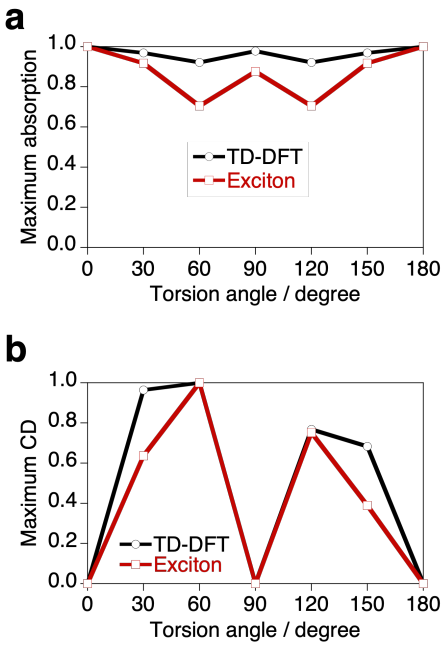

Figure 4.S4. Torsion angle dependence of calculated maximum positive a) absorption and b) CD intensities of **1** dimer by the Frenkel exciton model and TD-DFT. The absorption and CD intensities are normalized based on the calculated maximum.

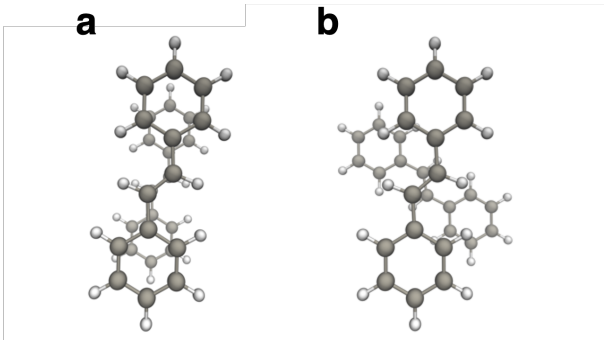

Figure 4.S5. Structures of **1** dimers with maximum positive a) absorption and b) CD intensities.

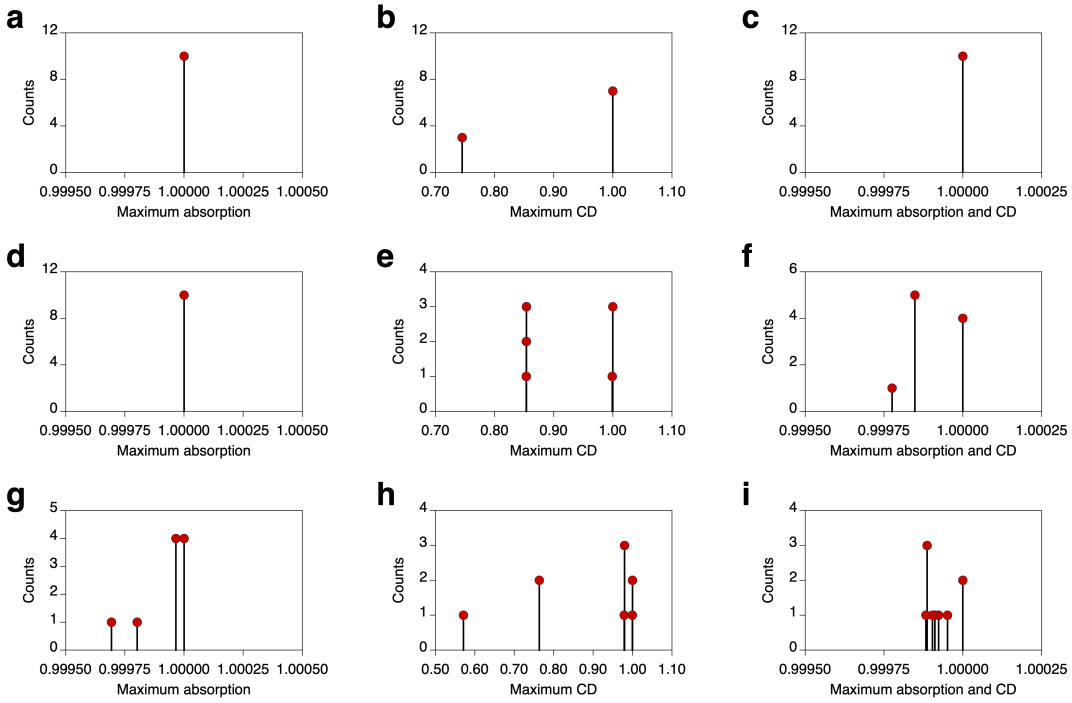

Figure 4.S6. Results of design using ten random-initial conditions. The resulting histograms with counts of locally maximized maximum absorption and CD intensity and both of them for (a–c) dimers, (d–f) pentamers, and (g–i) decamers. The target properties are normalized based on the obtained maximum.

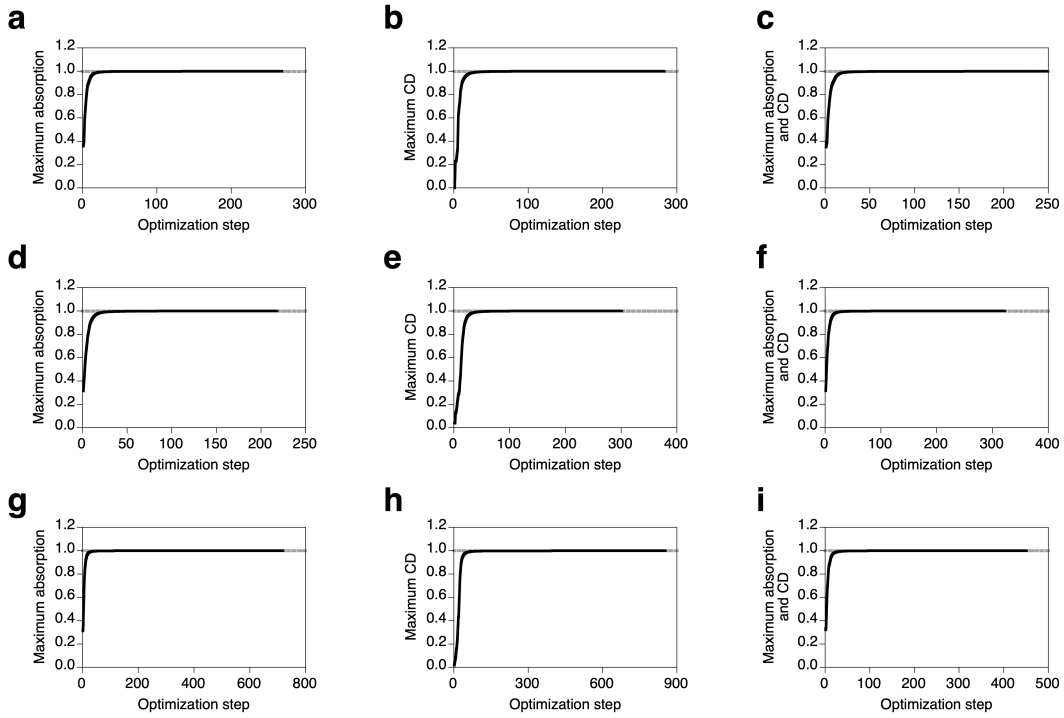

Figure 4.S7. Optimization histories of maximum positive absorption and CD intensities and both of them for (a–c) dimers, (d–f) pentamers, and (g–i) decamers. The gray dashed lines denote the objective function after rounding off the optimized participation coefficients. The target properties are normalized based on the obtained maximum.

Table 4.S1. Constituent molecules and structural parameters of designed dimers. The molecular site corresponds to the order of the stacking

Molecular site	Molecular species	Torsion angle (°)
Absorption		
1	**4**	0
2	**4**	0
CD		
1	**4**	0
2	**4**	66
Absorption and CD		
1	**4**	0
2	**4**	0

Table 4.S2. Constituent molecules and structural parameters of designed pentamers. The molecular site corresponds to the order of the stacking

Molecular site	Molecular species	Torsion angle (°)
Absorption		
1	**4**	0
2	**4**	0
3	**4**	0
4	**4**	0
5	**4**	0
CD		
1	**4**	0
2	**4**	12
3	**4**	51
4	**4**	90
5	**4**	102
Absorption and CD		
1	**4**	0
2	**4**	0
3	**4**	0
4	**4**	0
5	**4**	0

Table 4.S3. Constituent molecules and structural parameters of designed decamers. The molecular site corresponds to the order of the stacking.

Molecular site	Molecular species	Torsion angle (°)
Absorption		
1	**2**	0
2	**4**	0
3	**4**	0
4	**4**	0
5	**4**	0
6	**4**	0
7	**4**	0
8	**4**	0
9	**4**	0
10	**2**	0
CD		
1	**4**	0
2	**4**	9
3	**4**	24
4	**4**	42
5	**4**	57
6	**4**	72
7	**4**	87
8	**4**	105
9	**4**	120
10	**4**	129
Absorption and CD		
1	**2**	0
2	**4**	0
3	**4**	0
4	**4**	0
5	**4**	3
6	**4**	354
7	**4**	357
8	**4**	357
9	**4**	357
10	**2**	357

Analysis results of the absorption strength distribution of the designed systems

In this work, the author restricts myself to the Frenkel exciton model that includes the lowest intense excitation of each molecule for simplicity. Therefore, the objective function of the design is the maximum values of the spectra in the limited excitation energy range. To examine the true maximum across the entire spectral region, the authro analyzed the distribution of the oscillator strength which is related to the absorption strength. Following Ref. [65], the analysis was performed based on the Thomas–Reiche–Kuhn sum rule. The author employed the Frenkel exciton model for the analysis. For the dimer, the author also simulated the excited states in the same excitation energy region by TD-CAM-B3LYP/6-311+G(d). The TD-DFT reproduced the analysis result by the excitonic calculation. The author found that all the designed systems for the strong absorption have a few percent of the total oscillator strength in the calculated energy region, which means that the remaining part lies in the higher spectral range. This result shows that the present design only targets the excited state composed by the lowest excitation of each molecule that is practically important; *i.e.*, the global maximum peak may not have been captured in the present design.

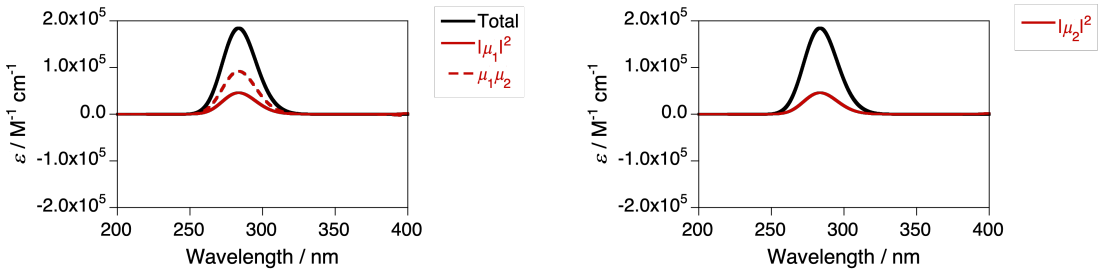

Figure 4.S8. FEDA result of the absorption spectrum of the designed dimer for strong absorption. $|\mu_i|^2$ is the intrinsic contribution from the molecule *i*. $\mu_i\mu_j$ is the exciton ETDM interaction between the molecules *i* and *j*. The indices of the molecules are in the order of the stacking.

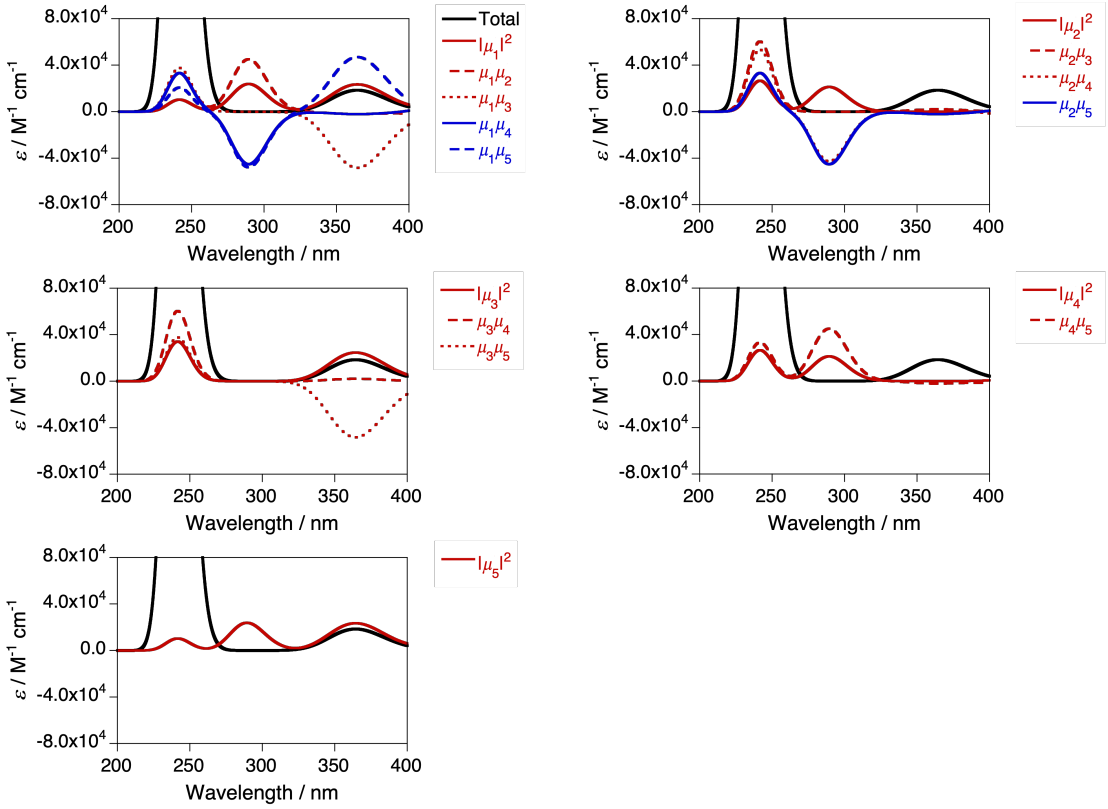

Figure 4.S9. FEDA result of the absorption spectrum of the designed pentamer for strong absorption. $|\mu_i|^2$ is the intrinsic contribution from the molecule *i*. $\mu_i\mu_j$ is the exciton ETDM interaction between the molecules *i* and *j*. The indices of the molecules are in the order of the stacking.

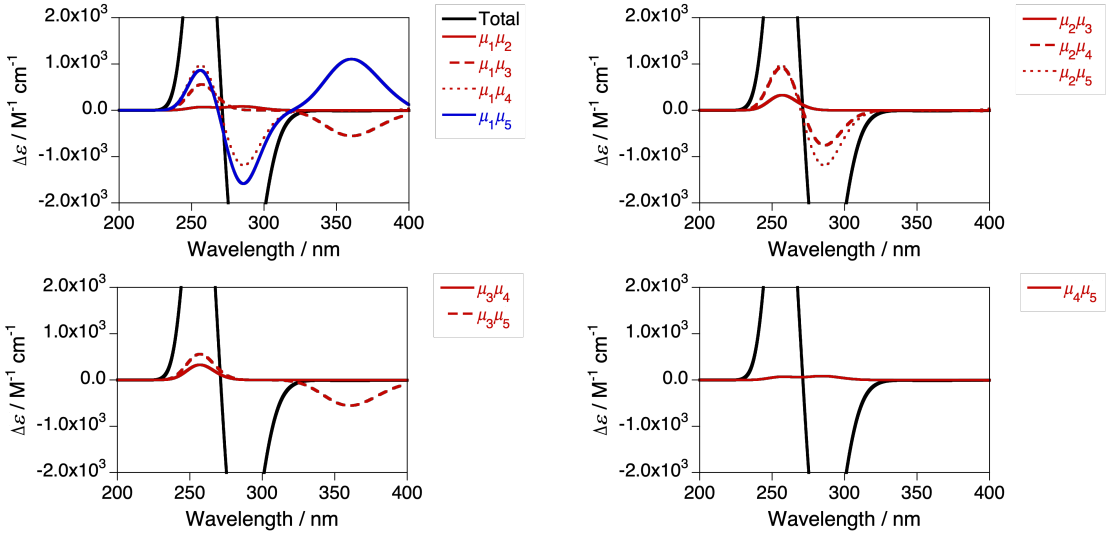

Figure 4.S10. FEDA result of the CD spectrum of the designed pentamer for strong CD. $\mu_i\mu_j$ is the exciton ETDM interaction between the molecules i and j. The indices of the molecules are in the order of the stacking.

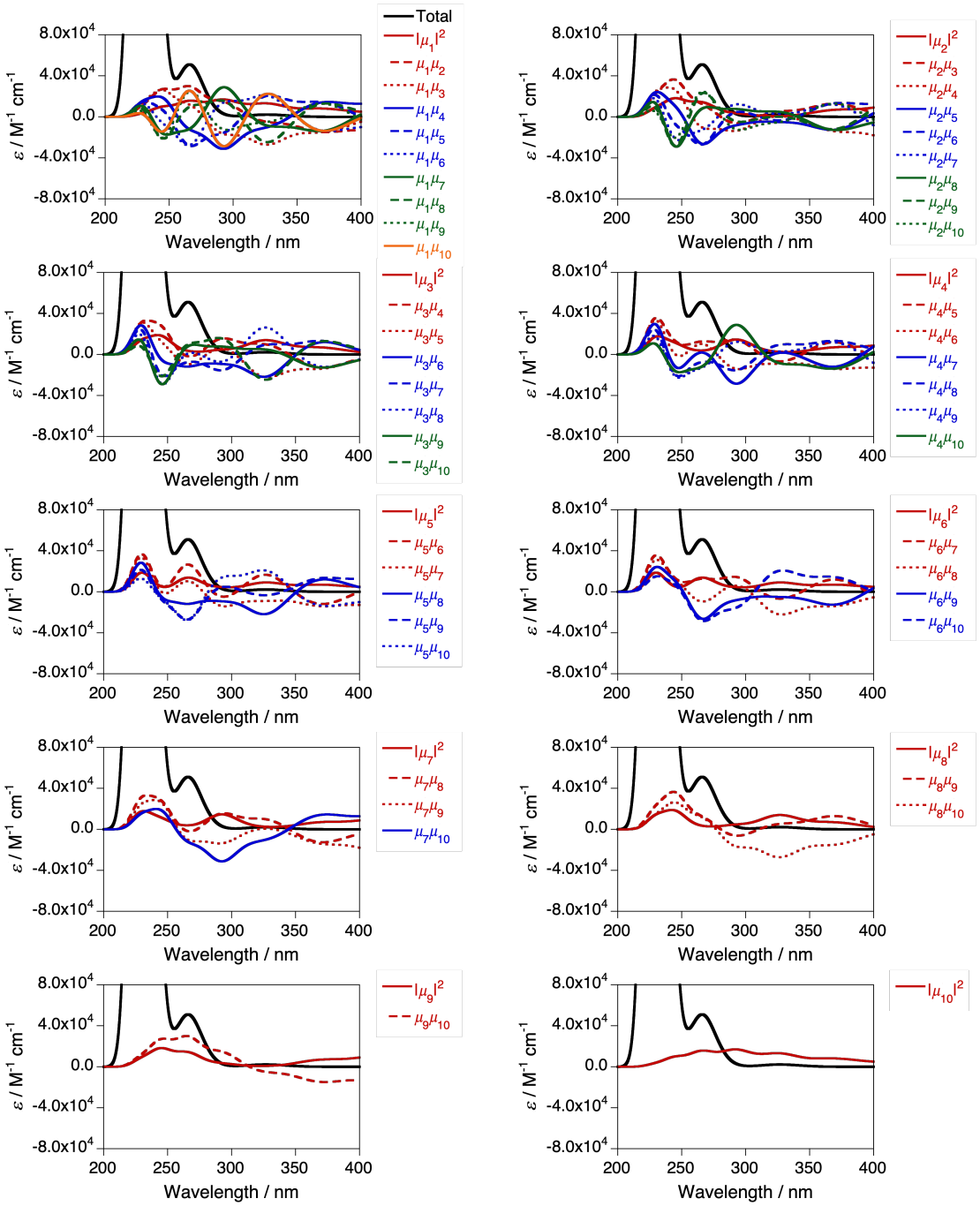

Figure 4.S11. FEDA result of the absorption spectrum of the designed decamer for strong absorption. $|\mu_i|^2$ is the intrinsic contribution from the molecule *i*. $\mu_i\mu_j$ is the exciton ETDM interaction between the molecules *i* and *j*. The indices of the molecules are in the order of the stacking.

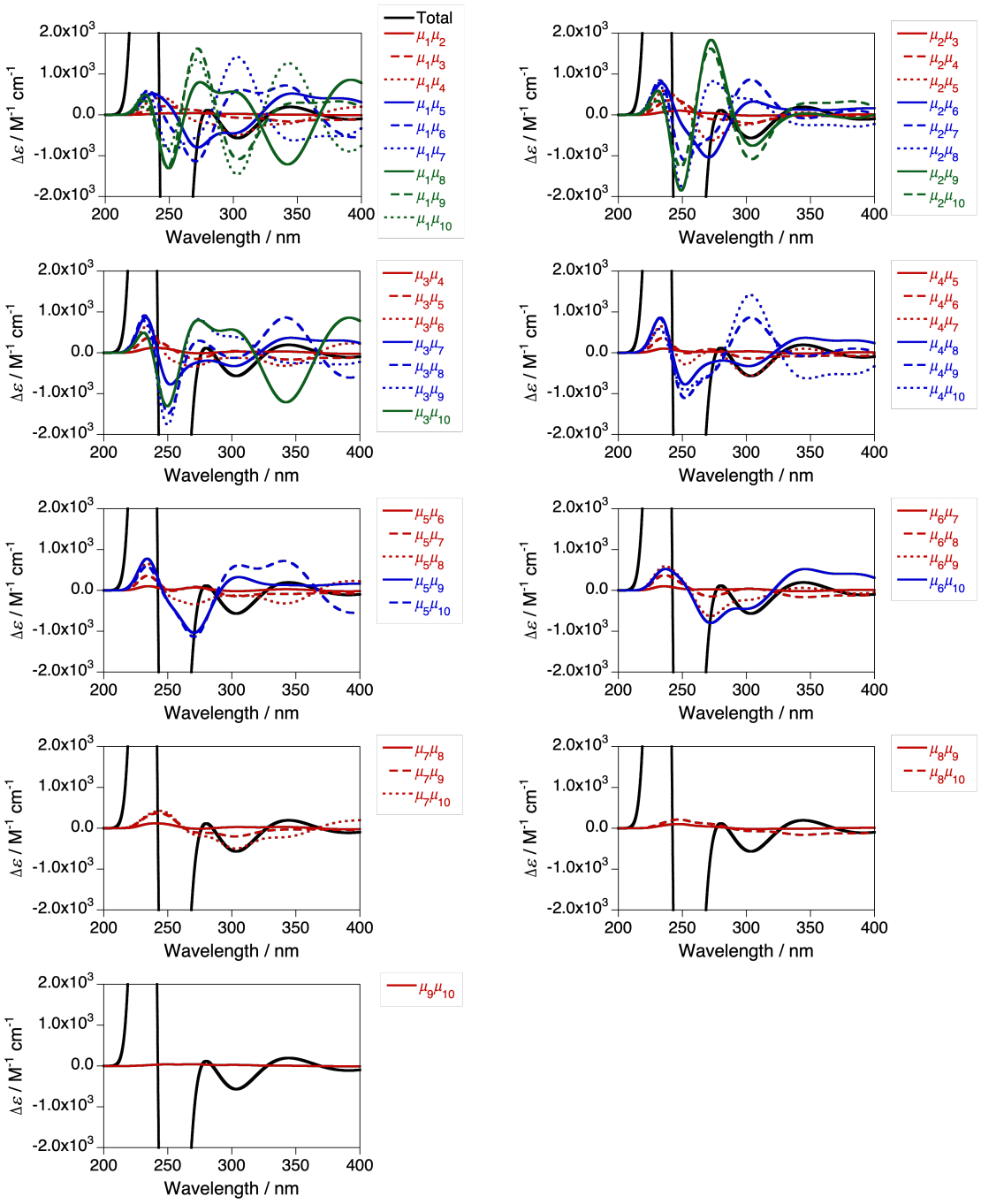

Figure 4.S12. FEDA result of the CD spectrum of the designed decamer for strong CD. $\mu_i\mu_j$ is the exciton ETDM interaction between the molecules i and j. The indices of the molecules are in the order of the stacking.

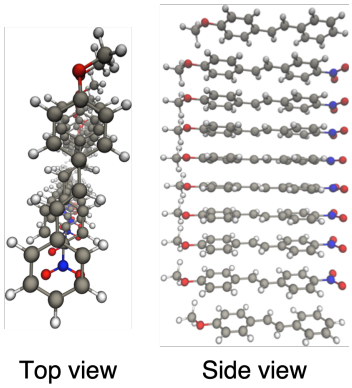

Figure 4.S13. Designed decamer with locally maximized both of maximum positive absorption and CD intensities.

References

[1] B. L. Feringa, R. A. van Delden, N. Koumura, E. M. Geertsema, *Chem. Rev.*, **2000**, *100*, 1789–1816.

[2] C. Petermayer, H. Dube, *J. Am. Chem. Soc.*, **2018**, *140*, 13558–13561.

[3] L. You, D. Zha, E. V. Anslyn, *Chem. Rev.*, **2015**, *115*, 7840–7892.

[4] M. Matuschek, D. P. Singh, H. H. Jeong, M. Nesterov, T. Weiss, P. Fischer, F. Neubrech, N. Liu, *Small*, **2018**, *14*, 1702990.

[5] B. L. Feringa, R. A. van Delden, *Angew. Chem. Int. Ed.*, **1999**, *38*, 3418–3438.

[6] P. K. Hashim, N. Tamaoki, *ChemPhotoChem*, **2019**, *3*, 347–355.

[7] C. C. Lee, C. Grenier, E. W. Meijer, A. P. Schenning, *Chem. Soc. Rev.*, **2009**, *38*, 671–683.

[8] E. Mattia, S. Otto, *Nat. Nanotechnol.*, **2015**, *10*, 111–119.

[9] A. Sorrenti, J. Leira-Iglesias, A. J. Markvoort, T. F. A. de Greef, T. M. Hermans, *Chem. Soc. Rev.*, **2017**, *46*, 5476–5490.

[10] M. Wehner, F. Würthner, *Nat. Rev. Chem.*, **2019**, *4*, 38–53.

[11] O. Ohmori, M. Kawano, M. Fujita, *CrystEngComm*, **2005**, *7*, 255–259.

[12] O. Ohmori, M. Kawano, M. Fujita, *Angew. Chem. Int. Ed.*, **2005**, *44*, 1962–1964.

[13] N. Yanai, T. Uemura, S. Kitagawa, *Chem. Mater.*, **2012**, *24*, 4744–4749.

[14] S. Tashiro, T. Umeki, R. Kubota, M. Shionoya, *Angew. Chem. Int. Ed.*, **2014**, *53*, 8310–8315.

[15] K. Matyjaszewski, J. Spanswick, *Mater. Today*, **2005**, *8*, 26–33.

[16] N. ten Brummelhuis, *Polym. Chem.*, **2015**, *6*, 654–667.

[17] J. De Neve, J. J. Haven, L. Maes, T. Junkers, *Polym. Chem.*, **2018**, *9*, 4692–4705.

[18] S. Mochizuki, T. Kitao, T. Uemura, *Chem. Commun.*, **2018**, *54*, 11843–11856.

[19] S. M. Risser, D. N. Beratan, S. R. Marder, *J. Am. Chem. Soc.*, **1993**, *115*, 7719–7728.

[20] C. Kuhn, D. N. Beratan, *J. Phys. Chem.*, **1996**, *100*, 10595–10599.

[21] A. Zunger, *Nat. Rev. Chem.*, **2018**, *2*, 0121.

[22] T. Shiraogawa, M. Ehara, *ChemPhotoChem*, **2019**, *3*, 707–718.

[23] S. Molesky, Z. Lin, A. Y. Piggott, W. Jin, J. Vucković, A. W. Rodriguez, *Nat. Photonics*, **2018**, *12*, 659–670.

[24] M. Wang, X. Hu, D. N. Beratan, W. Yang, *J. Am. Chem. Soc.*, **2006**, *128*, 3228–3232.

[25] O. A. von Lilienfeld, *Int. J. Quantum Chem.*, **2013**, *113*, 1676–1689.

[26] T. Weymuth, M. Reiher, *Int. J. Quantum Chem.*, **2014**, *114*, 823–837.

[27] B. Sanchez-Lengeling, A. Aspuru-Guzik, *Science*, **2018**, *361*, 360–365.

[28] J. G. Freeze, H. R. Kelly, V. S. Batista, *Chem. Rev.*, **2019**, *119*, 6595–6612.

[29] M. Foscato, V. R. Jensen, *ACS Catalysis*, **2020**, *10*, 2354–2377.

[30] A. Franceschetti, A. Zunger, *Nature*, **1999**, *402*, 60–63.

[31] O. A. von Lilienfeld, R. D. Lins, U. Rothlisberger, *Phys. Rev. Lett.*, **2005**, *95*, 153002.

[32] O. A. von Lilienfeld, M. E. Tuckerman, *J. Chem. Phys.*, **2006**, *125*, 154104.

[33] S. Keinan, X. Hu, D. N. Beratan, W. Yang, *J. Phys. Chem. A*, **2007**, *111*, 176–181.

[34] D. Xiao, W. Yang, D. N. Beratan, *J. Chem. Phys.*, **2008**, *129*, 044106.

[35] D. Balamurugan, W. Yang, D. N. Beratan, *J. Chem. Phys.*, **2008**, *129*, 174105.

[36] X. Hu, D. N. Beratan, W. Yang, *J. Chem. Phys.*, **2008**, *129*, 064102.

[37] S. Keinan, M. J. Therien, D. N. Beratan, W. Yang, *J. Phys. Chem. A*, **2008**, *112*, 12203–12207.

[38] S. Keinan, W. D. Paquette, J. J. Skoko, D. N. Beratan, W. Yang, S. Shinde, P. A. Johnston, J. S. Lazo, P. Wipf, *Org. Biomol. Chem.*, **2008**, *6*, 3256–3263.

[39] D. Xiao, L. A. Martini, R. C. Snoeberger, III, R. H. Crabtree, V. S. Batista, *J. Am. Chem. Soc.*, **2011**, *133*, 9014–9022.

[40] A. M. Chang, B. Rudshteyn, I. Warnke, V. S. Batista, *Inorg. Chem.*, **2018**, *57*, 15474–15480.

[41] T. Callahan, D. Masi, D. Xiao, *J. Phys. Chem. B*, **2019**, *123*, 10252–10259.

[42] M. d'Avezac, A. Zunger, *J. Phys.: Condens. Matter*, **2007**, *19*, 402201.

[43] M. Kasha, *Radiat. Res.*, **1963**, *20*, 55–71.

[44] N. J. Hestand, F. C. Spano, *Chem. Rev.*, **2018**, *118*, 7069–7163.

[45] A. Okamoto, *Chem. Soc. Rev.*, **2011**, *40*, 5815–5828.

[46] T. Shiraogawa, G. Candel, R. Fukuda, I. Ciofini, C. Adamo, A. Okamoto, M. Ehara, *J. Comput. Chem.*, **2019**, *40*, 127–134.

[47] N. Harada, K. Nakanishi. Circular Dichroic Spectroscopy—Exciton Coupling in Organic Stereochemistry; University Science Books: Mill Valley, CA, 1983.

[48] B. Mennucci, S. Corni, *Nat. Rev. Chem.*, **2019**, *3*, 315–330.

[49] T. Shiraogawa, M. Ehara, S. Jurinovich, L. Cupellini, B. Mennucci, *J. Comput. Chem.*, **2018**, *39*, 931–935.

[50] S. Jurinovich, G. Pescitelli, L. Di Bari, B. Mennucci, *Phys. Chem. Chem. Phys.*, **2014**, *16*, 16407–16418.

[51] J. H. Burroughes, D. D. C. Bradley, A. R. Brown, R. N. Marks, K. Mackay, R. H. Friend, P. L. Burnst, A. B. Holme, *Nature*, **1990**, *347*, 539–541.

[52] B. C. Akinwumi, K. M. Bordun, H. D. Anderson, *Int. J. Mol. Sci.*, 2018, *19*, 792.

[53] A. D. Becke, *J. Chem. Phys.*, **1993**, *98*, 5648–5652.

[54] T. Yanai, D. P. Tew, N. C. Handy, *Chem. Phys. Lett.*, **2004**, *393*, 51–57.

[55] D. Bousquet, R. Fukuda, D. Jacquemin, I. Ciofini, C. Adamo, M. Ehara, *J. Chem. Theory Comput.*, **2014**, *10*, 3969–3979.

[56] D. Bousquet, R. Fukuda, P. Maitarad, D. Jacquemin, I. Ciofini, C. Adamo, M. Ehara, *J. Chem. Theory Comput.*, **2013**, *9*, 2368–2379.

[57] D. Robinson, *J. Chem. Theory Comput.*, **2018**, *14*, 5303–5309.

[58] M. J. Frisch, G. W. Trucks, H. B. Schlegel, G. E. Scuseria, M. A. Robb, J. R. Cheeseman, G. Scalmani, V. Barone, G. A. Petersson, H. Nakatsuji, X. Li, M. Caricato, A. V. Marenich, J. Bloino, B. G. Janesko, R. Gomperts, B. Mennucci, H. P. Hratchian, J. V. Ortiz, A. F. Izmaylov, J. L. Sonnenberg, Williams, F. Ding, F. Lipparini, F. Egidi, J. Goings, B. Peng, A. Petrone, T. Henderson, D. Ranasinghe, V. G. Zakrzewski, J. Gao, N. Rega, G. Zheng, W. Liang, M. Hada, M. Ehara, K. Toyota, R. Fukuda, J. Hasegawa, M. Ishida, T. Nakajima, Y. Honda, O. Kitao, H. Nakai, T. Vreven, K. Throssell, J. A. Montgomery, Jr., J. E. Peralta, F. Ogliaro, M. J. Bearpark, J. J. Heyd, E. N. Brothers, K. N. Kudin, V. N. Staroverov, T. A. Keith, R. Kobayashi, J. Normand, K. Raghavachari, A. P. Rendell, J. C. Burant, S. S. Iyengar, J. Tomasi, M. Cossi, J. M. Millam, M. Klene, C. Adamo, R. Cammi, J. W. Ochterski, R. L. Martin, K. Morokuma, O. Farkas, J. B. Foresman, D. J. Fox., *Gaussian 16*, Rev. B01; Gaussian, Inc.: Wallingford, CT, 2016.

[59] W. Humphrey, A. Dalke, K. Schulten, *J. Molec. Graphics*, **1996**, *14*, 33–38.

[60] R. H. Byrd, P. H. Lu, J. Nocedal, C. Y. Zhu, *Siam J. Sci. Comput.*, **1995**, *16*, 1190–1208.

[61] C. Zhu, R. H. Byrd, J. Nocedal, *ACM Trans. Math. Softw.*, **1997**, *23*, 550–560.

[62] J. L. Morales, J. Nocedal, *ACM Trans. Math. Softw.*, **2011**, *38*.

[63] J. Kiefer, *Proc. Amer. Math. Soc.*, **1953**, *4*, 502–506.

[64] M. Matsumoto, T. Nishimura, *ACM Trans. Model. Comput. Simul.*, **1998**, *8*, 3–30.

[65] L. Zheng, N. F. Polizzi, A. R. Dave, A. Migliore, D. N. Beratan, *J. Phys. Chem. A*, **2016**, *120*, 1933–1943.

Chapter 5

Inverse Design of Molecule Close to the Metal Nanoparticle and Incident Light for the Desired Photophysical Property

5.1. Introduction

Light-response properties of molecules in the close vicinity of a metal nanoparticle (NP) surface are strongly modulated by the localized surface plasmon resonance (LSPR). For example, surface-enhanced Raman scattering (SERS),[1,2] modulation of the molecular fluorescence,[3,4] and plasmon-mediated chemical reactions[5,6] are observed. Making use of the plasmonic phenomena is promising for realizing desired photophysical properties of molecules and manipulations of (photo)chemical events.

The molecule−NP systems have huge potential for the design in terms of the designability of their components. Regarding the molecule, more than 8 million molecules have been already synthesized and are available.[7] From a practical point of view, it is often important to adjust the properties of a molecule by introducing substituents. The properties of the NP, including LSPR, are determined by its nature, size, shape, and environment. The NPs of coinage metals such as gold and silver have the LSPR characters. For the precise control of the NP structures, colloidal synthesis methods and nanofabrication techniques enable these controls. The relative position and orientation of the molecule and NP also affect the properties of the whole system. The control of the distance between molecule and NP is experimentally realized, and the changes of the plasmonic phenomena were observed.[8,9] The incident electromagnetic field, which produces the LSPR and mediates molecule−plasmon interaction, is highly controllable with respect to the time profile and intensity. Thus, the molecule−plasmon systems have a wealth of design possibilities and are promising for nanophotonics

applications. The appropriate design guidelines of the tunable parameters of the system are important for exploiting the potential of the plasmonic systems.

For the design of the electronic dynamics, the population transfer from a specific state to a target state is important to manipulate the subsequent photochemical phenomena. The nuclear motion is negligible for the interaction of the molecule with the ultrashort laser pulse in a time scale of a few femtoseconds. In practice, minimizing fluence of the incident field is required in addition to maximization of the population of a specific electronic state.

Design approaches of molecular systems can be categorized into direct and inverse design from the relation between the system and its desired property.[10,11] Conceptually, inverse design that starts from the desired performance and predicts the molecular structure is in a straightforward fashion in contrast to the direct approach by "guess and check." However, in practice, it is difficult to obtain a realizable molecular system from the desired property by directly solving the inverse problem of the Schrödinger equation.[12,13] Thus, commonly, the inverse design indicates a design strategy driven by information on functional space corresponding to chemical space.[13-18]

Converting discrete chemical space of candidate molecular systems into continuous one makes it possible to use gradients of the desired property with respect to characteristics of molecular systems for finding optimal systems. In alchemical transformation methods, the continuous chemical space is interpolated by alchemical systems which are not realizable. The variational particle approach[12,19,20] and the linear combination of atomic potentials (LCAP)[21] are the alchemical transformation methods

based on quantum chemical models. In this work, we used the LCAP flamework based on the effective Hamiltonian[22,23] for designing molecule−NP systems.

In addition to the design of molecular systems, the inverse design of a suitable perturbing agent (e.g., an incident laser pulse) is widely applied to the studies of molecular electronic states.[24] The quantum optimal control theory (QOCT) is often used to refer to inverse design of an electromagnetic field applied to a molecule, but they are the same in principle. Such a design by theoretical means requires the time-domain description of the phenomena involving light such as the LSPR.

To theoretically describe molecule−plasmon systems, combining the quantum chemical description of the molecule, often referred to as "QM", with a (semi)classical model of the metal NP is effective since the applicability of full QM methods is computationally limited for the large NPs.[25,26] In particular, the boundary element method (BEM), which treats the metal NP as a homogeneous and continuous dielectric described through PCM-NP[27-29] based on the polarizable continuum model (PCM),[30] is useful for interfacing with the QM description of the molecules. This is because the numerical procedure of the BEM only requires a two-dimensional calculation of charges distributing on the discretized NP surface. Furthermore, the PCM-NP method can model complex-shaped metal NPs. Recent developments in the BEM in the time domain allow simulations of real-time plasmonic phenomena.[29,31-34]

For the inverse design based on the theoretical description, it is necessary to represent continuous chemical space of possible molecular−NP systems. As described above, the QM/BEM method can simulate photophysical properties of molecular−NP systems based

on its design variables: nature, size, shape, and environment of the NP; molecular species; mutual conformation and distance between the molecule and NP; time profile and intensity of the applied electromagnetic field. Therefore, the QM/BEM is well suited to the inverse design. Indeed, the BEM was recently utilized in the design toward optimal mechanical control of a plasmonic NP by incident light.[35]

In this work, we develop an inverse design method of molecule−NP system and incident light for the desired photophysical property based on the QM/BEM method. For the molecule−NP system, the inverse design method enables the design of the molecular species and the relative molecule−NP distance and conformation. We applied this method to the design of the system with the maximized population of a target electronic state of the molecule at the desired time. The design of the molecule, incident electric field, and both of them was performed on several metal NPs with different metal natures and NP shapes. The results were assessed in terms of the design performance.

5.2. Methods

Here, we describe the proposed inverse design method of the molecule−NP systems and incident electric fields. Firstly, we describe the real-time description of the electronic dynamics of a molecule near a metal NP in order to establish some notations. Secondly, we present the inverse design method based on this theoretical model. Then, the chemical space and incident field for the present design are described. Finally, the computational details are given.

5.2.1. TD-CI coupled with TD-BEM

We briefly summarize the theoretical description of molecule−NP systems by the time-dependent configuration interaction (TD-CI) method for the molecule coupled with the TD-BEM for the metal NP, developed in Ref. [32]. The effective Hamiltonian of the molecule near the NP includes the field-free electronic Hamiltonian $\hat{H}_0$ of the molecule, molecule−radiation interactions, and molecule−NP interactions:

$$\hat{H}_S(t) = \hat{H}_0 - \hat{\mu} \cdot \vec{E}_{\text{inc}}(t) + \left(\mathbf{q}_{\text{ref}}(t) + \mathbf{q}_{\text{pol}}(t)\right) \cdot \hat{\mathbf{V}} \tag{1}$$

where $\hat{\mu}$ is the electric dipole operator and $\vec{E}_{\text{inc}}(t)$ is the time-dependent incident electric field. The molecule−radiation interaction is modeled in the dipole approximation in the length gauge. In the BEM, the metal NP is described as a continuum body characterized by a dielectric function of the metal. The TD-BEM describes the response of the metal NP to the incident field and molecule as time-dependent polarization charges $\mathbf{q}_{\text{ref}}(t)$ and $\mathbf{q}_{\text{pol}}(t)$, respectively, located on geometrical centers of each mesh of the discretized NP surface. The portion of the discretized surface is called tesserae. $\hat{\mathbf{V}}$ is the electrostatic potential operator acting at the same positions with these charges. In this work, the employed BEM model is in the integral equation formalism[36] and within the quasi-static approximation.

The wavefunction $\left|\Psi(t)\right\rangle$ of the molecule near the NP is propagated based on the time-dependent Schrödinger equation with the incident field

$$i\frac{\partial}{\partial t}\left|\Psi(t)\right\rangle = \hat{H}_S\left|\Psi(t)\right\rangle. \tag{2}$$

$\left|\Psi(t)\right\rangle$ is expanded using reference ground and excited states $\left|\Phi_I\right\rangle$ with $I = 0$ and $I > 0$, respectively, of the molecule in the CI theory as

$$\left|\Psi(t)\right\rangle = \sum_I C_I(t)\left|\Phi_I\right\rangle \tag{3}$$

where $C_I(t)$ is the time-dependent coefficient for the reference Ith electronic state. The reference ground state $\left|\Phi_0\right\rangle$ is the Hartree−Fock wavefunction of the molecule equilibrated with the NP. The excited states obtained by the CI singles (CIS) are used as $\left|\Phi_I\right\rangle$ with $I > 0$. The corresponding time-independent Schrödinger equation for the molecule in the presence of the fixed polarization charge $\mathbf{q}_{\text{pol}}\left(\left|\Phi_0\right\rangle\right)$ evaluated with $\left|\Phi_0\right\rangle$ is

$$\left[\hat{H}_0 + \mathbf{q}_{\text{pol}}\left(\left|\Phi_0\right\rangle\right)\cdot\hat{\mathbf{V}}\right]\left|\Phi_I\right\rangle = E_I\left|\Phi_I\right\rangle \tag{4}$$

where E_I is the electronic energy of the Ith electronic state. By using equation (3), equation (2) becomes

$$i\frac{\partial \mathbf{C}}{\partial t} = \mathbf{H}\mathbf{C} \tag{5}$$

where **H** is the Hamiltonian matrix having the elements

$$H_{IJ}(t) = E_I\delta_{IJ} - \vec{\mu}_{IJ}\cdot\vec{E}_{\text{inc}}(t) + \left(\mathbf{q}_{\text{ref}}(t) + \Delta\mathbf{q}_{\text{pol}}(t)\right)\cdot\mathbf{V}_{IJ} \tag{6}$$

with

$$\Delta\mathbf{q}_{\text{pol}}(t) = \mathbf{q}_{\text{pol}}(t) - \mathbf{q}_{\text{pol}}\left(\left|\Phi_0\right\rangle\right), \tag{7}$$

$$\vec{\mu}_{IJ} = \left\langle\Phi_I\right|\hat{\mu}\left|\Phi_J\right\rangle, \tag{8}$$

$$\mathbf{V}_{IJ} = \left\langle \Phi_I \middle| \hat{\mathbf{V}} \middle| \Phi_J \right\rangle . \tag{9}$$

In the TD-BEM, the time evolution of $\mathbf{q}_{\mathrm{ref}}(t)$ and $\mathbf{q}_{\mathrm{pol}}(t)$ can be computed using the arbitrary dielectric function (e.g., experimentally observed one) in the frequency domain.[34] Although effective simplification of the equation of motion of the polarization charges is proposed in Ref. [34], it was not used in this work.

5.2.2. Inverse design of the molecule near the NP and the incident field

The present inverse design uses the Hamiltonian matrix of equation (6) to represent continuous chemical space of candidate molecule−NP systems, which allows the gradient-directed design by continuous optimization. The optimal molecule and molecule−NP configuration can be efficiently predicted among the candidates by the inverse design. For the molecule and its conformation relative to the NP, the Hamiltonian matrix of the TD-CI/TD-BEM approach reads the electronic state energies (E_I), electric dipole moments ($\vec{\mu}_{IJ}$), and molecular potentials on tesserae of the NP (V_{IJ}). Therefore, in the inverse design of the molecule−NP systems with respect to the molecular species and its spatial arrangement, we express these molecular characteristics as

$$E_I = \sum_{i,j,k} b_i c_j d_k E_{I,i,j,k} , \tag{10}$$

$$\vec{\mu}_{IJ} = \sum_{i,j,k} b_i c_j d_k \vec{\mu}_{IJ,i,j,k} , \tag{11}$$

$$V_{IJ} = \sum_{i,j,k} b_i c_j d_k V_{IJ,i,j,k} \tag{12}$$

where $E_{I,i,j,k}$, $\vec{\mu}_{IJ,i,j,k}$, and $V_{IJ,i,j,k}$ are E_I, $\vec{\mu}_{IJ}$, and V_{IJ} of the molecule of the *i*th candidate molecular species with the *j*th candidate conformation and *k*th candidate distance with respect to the NP, respectively. b_i, c_j, and d_k are the corresponding participation coefficients, which are treated as optimization variables to tailor the system. The participation coefficients take a value between 0 and 1, and its sum for all the corresponding candidates is 1:

$$\sum_i b_i = \sum_i c_i = \sum_i d_i = 1. \tag{13}$$

When all the participation coefficients are 0 or 1, the Hamiltonian matrix and time evolution of the system are identical to those of the real system. To find the optimal molecule−NP system in the chemical space, the participation coefficients are rounded off after the optimization. Moreover, for the designed system, rounded-off values of the optimized participation coefficients need to satisfy the condition of equation (13). The participation coefficients widely distributed among the candidates do not meet this requirement. Thanks to the continuous chemical space represented by the participation coefficients, the derivative of the design target property *P* of the molecule−NP system with respect to the participation coefficients can be defined. Therefore, the inverse design of the molecule near the NP can be implemented by the efficient gradient-based optimization of the participation coefficients. By further expanding equations (10)−(12) for the other elements of the candidate molecules, it is possible to more efficiently represent the chemical space by the combination of the different participation

coefficients; for example, candidate derivatives of the molecular species can be expressed by the difference in the substituents and grouped arbitrarily.

In the design, the incident electric field irradiated to the molecule−NP system is represented by a sum over different harmonics having the frequency $\omega = \frac{\pi}{T}$ with the time duration T of the light irradiation:[37]

$$\vec{E}_{\text{inc}}(t) = \sum_{A}\sum_{j}^{M} a_{j,A} \sin(j\omega t)\vec{d}_{A} . \tag{14}$$

where $\vec{d}_{A}$ is 1.0 a.u. for all the directions specified by the index A running over the three Cartesian coordinates. The intensity of the field is zero at the start and end of the illumination (t = 0 and T, respectively) and thus more easily obtained in the experiments. The amplitudes $\{a_{j,A}\}$ of the sine wave components are treated as optimization variables to design the optimal incident field that drives the desired time evolution of the molecule−NP system. In the design of both the incident field and the molecule of the molecule−NP system, the tailored field is further optimized for the designed molecule after rounding-off the participation coefficients.

The design of the molecule−NP system and incident electric field is achieved by maximizing the objective function J defined as a sum of the desired property P of the system and the penalty term to the high fluence of the incident field:

$$J = P - \alpha \int_{0}^{T} \left|\vec{E}_{\text{inc}}(t)\right|^{2} dt \tag{15}$$

where α is a dimensionless penalty factor and constant over the time. The larger α, the more negative the penalty term and the smaller J becomes. In this work, the target

property is the population of the first excited state of the molecule near the NP at the end of the molecule− and NP−radiation interactions. For the target property, to steer the intermediate participation coefficients $\{b_i\}$, $\{c_i\}$, and $\{d_i\}$ to the discrete values (0 or 1) in the optimization, by introducing a dimensionless penalty factor γ, we represent the target property as

$$P = \sum_{i,j,k} b_i^{\gamma} c_j^{\gamma} d_k^{\gamma} P_0 \tag{16}$$

where P_0 is the original target property evaluated with $\{b_i\}$, $\{c_i\}$, and $\{d_i\}$. When γ is equal to 1.0, P is identical to P_0. Using γ that is larger than 1.0, P and J become smaller in the intermediate regime of the participation coefficients, while larger when closer to 1 or 0. As such, the proper γ can be used so that the optimized participation coefficients satisfy the condition of equation (13).

5.2.3. Chemical space

As the candidate molecular species, *N*-methyl-6-quinolone (MQ) and its derivatives (EMQ and 3tBu-MQ) shown in Figure 5.1 were adopted as an example. This choice enables us to investigate substituent effects in the design, which is important from a practical point of view in making use of the plasmon to modulate properties of a molecule possessing a specific motif. MQ has been well studied in terms of its peculiar photophysical properties[38] and adopted in the inverse design studies of the incident field.[39,40] EQ and 3tBu-MQ were used to investigate the substituent effects.[41,42] We considered two types of distances and conformations of the molecule relative to the NP

as the candidates. The molecular plane is located on the *xy* or *yz* plane in the Cartesian coordinates shown in Figure 5.1. The candidate distances between the mass center of the molecule and the closest NP surface are 5 and 8 Å.

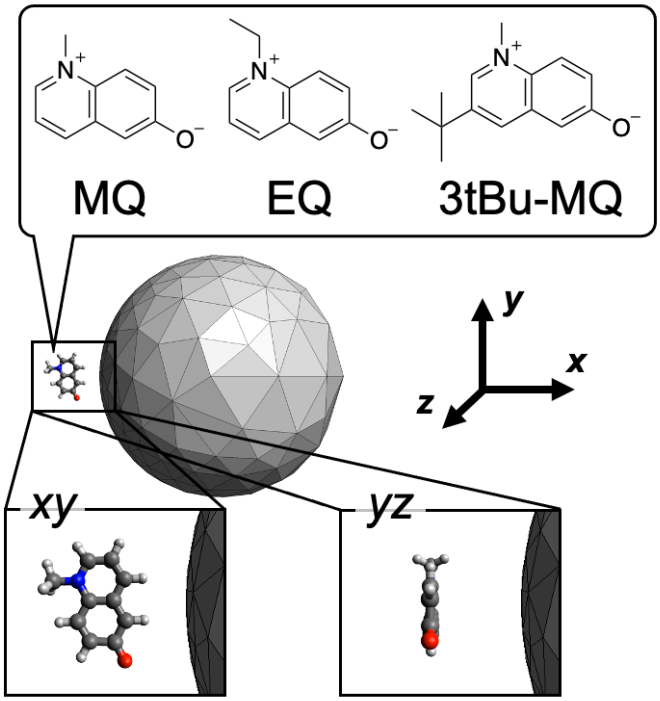

Figure 5.1. Schematic representation of the candidate molecule + metal NP system. The chemical structures are of the candidate molecular species. The candidate conformation *xy* and *yz* indicate that the molecular planes are located on the *xy* and *yz* planes of the Cartesian coordinates, respectively. Drawing out of scale.

In this work, the inverse design was performed on the NPs with cubic, ellipsoidal, rod, and spherical shapes. The nanocube has a side length of 10 nm and a curvature radius at the edges of 1 nm. The ellipsoidal NP has a semi-major axis length of 8 nm and two semi-

minor axes of 5 nm. The nanorod is 10 nm long and has a cylinder radius of 1.5 nm. The spherical NP has a 5 nm radius. These NPs have a similar surface area. The surface was divided into 664 triangular tesserae and refined near the molecule (Figure 5.2) by using the Gmsh software.[43] The metal NPs considered in this work do not have a small diameter (<3 nm) where the non-local effects of the dielectric function are significant. In addition, the quasi-static approximation used in the BEM is validated in the wavelength range of the calculated electronic states because of the small object size.

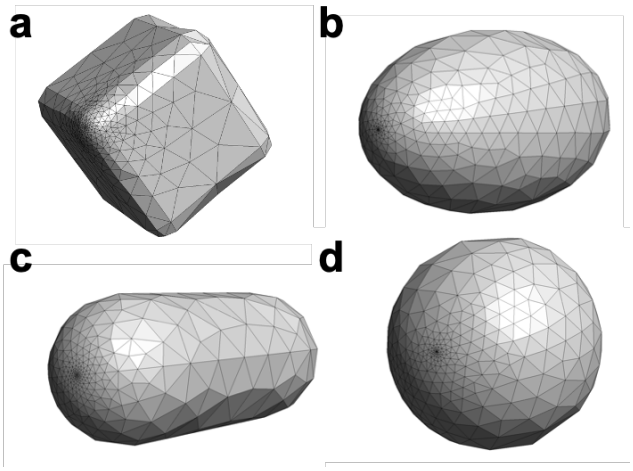

Figure 5.2. Metal NPs of (a) cubic, (b) ellipsoidal, (c) rod, and (d) spherical shapes. The visualization was performed by Gmsh.[43] The structures from the other views can be found in Figures 5.S1 and 5.S2.

As the metal natures of the NPs, gold and silver were adopted. The parametrization of the Drude–Lorentz (DL) expansion for the TD-BEM was performed using experimentally observed dielectric functions of the bulk metals.[34] We used six DL terms

in the expansion. The experimental data were taken from Refs. [44] and [45] for gold and silver, respectively.

The BEM calculations in the frequency domain were performed to check the TD-BEM scheme for the nanoparticles employed in this work. For this purpose, we computed the dynamic polarizability of the NPs, which is related to the photo-absorption. The applied field to the NP for the TD calculations is the same as that adopted in Ref. [34] and propagating in the *x* direction. The TD-BEM results are in almost perfect agreement with those obtained by the frequency-domain calculations, which validates the modeling of the TD-BEM method.

5.2.4. Computational details

We optimized geometries of the candidate molecules under the C_S symmetry at the Hartree−Fock level of theory by using the Gaussian 16 software.[46] The Hartree−Fock and CIS calculations of the molecules equilibrated with the metal NP were performed by a locally modified version of Gamess.[47,48] The 6-31G(d) basis set was employed for these calculations.

The real-time simulation and design of the molecule−NP system and incident electric field were performed using a locally modified version of WaveT.[32,33] The ground and low-lying 10 excited states of the molecule were included in the Hamiltonian. We adopted a time step of 2.42 as (0.10 a.u.) in the time evolution of the system. The wavefunction of the molecule was propagated by the Euler algorithm. The time duration of the incident field was chosen to 250 a.u. (≈ 6 fs) to focus on the ultrafast electron dynamics and its

related functions. In the design of the optimal incident field, all the initial amplitudes $\left\{a_{j,A}\right\}$ of the sine wave components in equation (14) were set to 1.0 × 10^{-7} a.u. The Gaussian sinusoidal wave was adopted as a fixed incident field used to demonstrate the inverse design of the molecular part of the molecule−NP system:

$$\vec{E}_{\text{inc}}\left(t\right)=\vec{E}_{\text{max}}\exp\left(-\frac{\left(t-t_0\right)^2}{\sigma^2}\right)\sin\left(\omega_{\text{pulse}}t\right) \tag{17}$$

where the central t_0 is 125 a.u., the pulse width σ is 49.61 a.u., and the pulse frequency ω_{pulse} is 3.0 eV, similar to the excitation energy for the first excited state of the MQ molecule and its derivatives. The maximum value of the electric field $\vec{E}_{\text{max}}$ is (1.0 × 10^{-6}, 0.0, 0.0) a.u. for the (*x*, *y*, *z*) directions. The time profile of this incident field along the *x* direction is shown in Figure 5.3(a). Figure 5.3(b) displays the Fourier transform (FT) of the incident field.

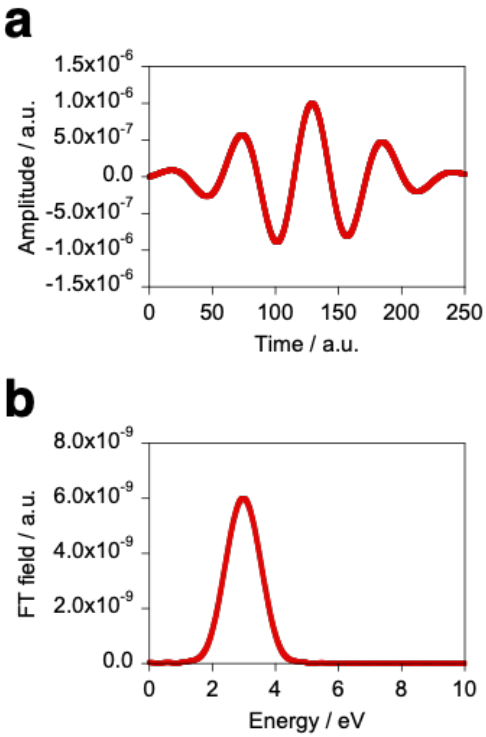

Figure 5.3. a) Time profile of the fixed incident field used in the design of the optimal molecule along the *x* direction and b) its FT.

The continuous optimization of the participation coefficients and the amplitudes of the incident field in equation (14) was performed by the quasi-Newton method with the limited-memory Broyden–Fletcher–Goldfarb–Shanno (L-BFGS) algorithm[49] implemented in the L-BFGS-B code version Lbfgsb.3.0.[50,51] The derivatives of the target property with respect to the participation coefficients and the amplitudes of the field were computed as numerical differentials in the forward-finite difference formulation with the small number of 1.0×10^{-5} and 1.0×10^{-11} for the molecule and incident field, respectively. To tailor the incident field, well-established approaches such as the Rabitz algorithm[52] can be used. However, in this work, the simple gradient-based optimization

was adopted to combine the design of the molecule and incident field. In each design for the molecule, using the different randomized initial participation coefficients, the design was performed five times. The optimization stopped when the difference of the objective function was smaller than a small number ε in the line search. ε was set to 2.2×10^{-13} and 2.2×10^{-7} for the design with the fixed and optimal fields, respectively. In the first ten optimization steps, ε was set to zero in order to suppress the termination of the design.

5.3. Results and Discussion

5.3.1. Design of the molecule near the metal NP

The performance of the inverse design of the molecule of the molecule−NP system was assessed by comparing results of the screening and design. Here, the objective function of the design is the population of the first excited state of the molecule because the incident field (and its fluence) is fixed to the Gaussian sinusoidal pulse (equation (17) and Figure 5.3). In the screening, we performed calculations of all the possible systems of the design of the molecule near the silver spherical NP with the irradiation of the fixed incident field. The calculation results given in Table 5.1 show that the various target properties are obtained depending on the substituents of MQ and the relative distance and conformation between the molecule and NP. The target state population of the molecules in the *xy* conformation is larger than that in the *yz* one. In the same distance and molecular species, the population differs by about 10^2–10^5 in these conformations. This is possibly related to the direct transition from the ground state because the incident field directs along the *x* direction and the *z* component of the electric transition dipole moment for the

ground and first excited states of the candidate molecules is null, although the other pathways of the population transfer are possible. The MQ or EQ molecule on the *xy* plane and at a distance of 5 Å from the nearest silver NP surface has the largest target property. In the inverse design, the MQ system with the largest population was designed in all the trials. In this design, the optimized participation coefficients for the relative orientation and distance of the molecule with respect to the NP are localized. On the other hand, these for the molecular species are 0.57 and 0.43 for MQ and EQ, respectively. The difference between the optimized and designed target properties is about 1% of the designed one. This gap can be large in the design of both the optimal molecule and incident field. In contrast, using the penalty factor $\gamma = 1.05$ for the widely distributed participation coefficients, the optimized participation coefficients were fully localized on the MQ or EQ molecule; the MQ and EQ systems were obtained three and two times in the five trials of the design with $\gamma = 1.05$, respectively. The typical optimization history of the target property obtained in the design of the MQ system is shown in Figure 5.4. The design results suggest that the target property is smooth as a function of the participation coefficients.

Table 5.1. Population of the first excited state of the candidate molecules near the silver spherical NP at the end of the incident field illumination. The possible molecule−NP systems are classified according to the molecular species and the relative molecule−NP conformation and distance

Species	Conformation	Distance (Å)[a)]	Population
MQ	*xy*	5	3.64×10^{-8}
EQ	*xy*	5	3.64×10^{-8}
3tBu-MQ	*xy*	5	3.53×10^{-8}
MQ	*yz*	5	3.35×10^{-13}
EQ	*yz*	5	1.67×10^{-13}
3tBu-MQ	*yz*	5	1.51×10^{-10}
MQ	*xy*	8	2.90×10^{-8}
EQ	*xy*	8	2.96×10^{-8}
3tBu-MQ	*xy*	8	2.84×10^{-8}
MQ	*yz*	8	1.02×10^{-13}
EQ	*yz*	8	2.54×10^{-13}
3tBu-MQ	*yz*	8	1.02×10^{-10}

[a)]Distance between the mass center of the molecule and the nearest NP surface.

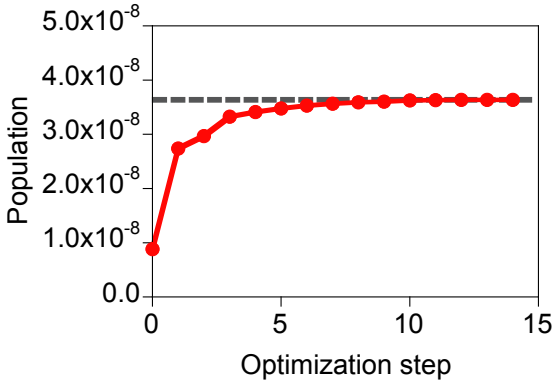

Figure 5.4. Optimization history of the target property obtained in the design of the MQ molecule near the silver spherical NP with the penalty factor $\gamma = 1.05$. The gray dashed line denotes the target property after rounding off the optimized participation coefficients.

5.3.2. Design of the incident electric field

The inverse design of the incident electric field was performed using the 13 sine wave components with different harmonics (i.e., M = 13 in equation (14)). To observe the dependence of the design results on the incident field fluence, we employed α = 1, 10, and 100 since the larger α imposes the larger penalty on the fluence. The results are shown in Table 5.2. When α is equal to 1, we designed the incident light that realizes the perfect population transfer with the target state population of 1.00, an upper limit. The more limited the fluence and the smaller the population of the first excited state of MQ were obtained with the larger α. This means that a high-intensity electric field is needed to realize the highly populated target excited state of MQ. Figure 5.S3 displays the time profiles of the optimal incident fields. The x and y components of the incident field have large amplitudes in comparison with the z component under the restriction on the total field fluence in the optimization. As discussed above, the direct transition from the ground state by the z direction field is suppressed since the z component of the electric transition dipole moment of MQ between the ground and target excited states is null. Not only the intensity of the incoming light but also the shape of the pulse differs depending on α. The optimization histories of the objective function of the design with the different penalty factors are shown in Figure 5.5, along with variations of the target state population and total fluence. The outcome value of the design decreases in the order of α = 1, 10, and 100. The optimization takes more steps to satisfy the optimization condition when the penalty becomes loose, i.e., the fluence is high. The value of the objective function smoothly increases with the optimization step; the objective function is smooth as a

function of the amplitudes of the sine wave components. The results indicate that the optimal control of the incident field is effective in realizing designing the desired photophysical property of molecule−NP systems.

Table 5.2. Objective function (J), target property (P), and total fluence of the incident field obtained in the design with the penalty factor α for the incident field

α	J	P	Fluence (a.u.)
1	0.991	1.000	8.56×10^{-3}
10	0.933	0.990	5.68×10^{-3}
100	0.653	0.862	2.09×10^{-3}

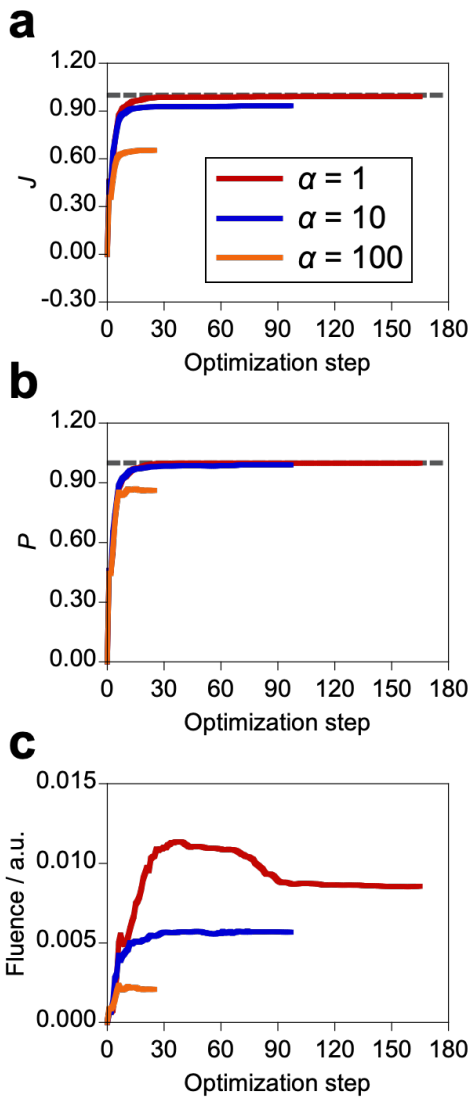

Figure 5.5. (a) Optimization histories of the objective function in the design of the optimal incident field with the different penalty factors α for the field fluence, along with variations of (b) population of the target state and (c) total fluence of the incident field. The gray dashed line denotes the value of 1.00. The individual data are shown in Figure 5.S4.

5.3.3. Design of both the molecule and incident electric field

We conducted the inverse design of both the optimal molecule close to the metal NP and incident electric field. The design was performed on several types of metal NPs with different metal natures and NP shapes. According to the results obtained at the last section, the penalty factor of α = 100 for the incident field, which provided non-saturated population in the design of the molecular part of the system, was adopted to investigate the influence of the metal NP features on the design results. As the penalty factor for the intermediate participation coefficients, we adopted γ = 1.05 which made the optimized participation coefficients localized on the candidates after the optimization in the molecule design. In the five trials of each design, the obtained system with the best objective function is referred to as the designed system here. When the optimized participation coefficients did not satisfy the condition of equation (13) by using the penalty factor γ = 1.05, we used the larger γ = 1.20 as shown in Table 5.S1. Table 5.3 shows the designed systems and properties. Two trials of the design on the silver nanorod terminated because the calculation time exceeded 100 hours. Figures 5.S5 and 5.S6 display the designed molecule + metal NP systems designed on the silver and gold NPs, respectively. The corresponding optimal incident fields are shown in Figures 5.S7 and 5.S8. All the designed molecules have the *xy* conformation regardless of the NP type, and therefore the amplitude of the *z* component of the optimal incident field is small, as discussed in the last section. Comparing with the design of the electric field applied to the MQ + silver spherical NP system (Table 5.2, α = 100), by the design on the same metal NP, the larger objective function (+0.022) was obtained with the EQ molecule

possessing the *xy* conformation at 5 Å distance from the silver spherical NP surface (Table 5.3). This indicates that the design of both the substituents of the molecule and the incident field is effective for realizing the desired property of the molecule–NP system. Furthermore, this designed system has the largest objective function in all the obtained systems.

In the design, the objective function, population of the target state, and field fluence take various values depending on the metal nature and NP shape but also the optimal molecule and incident field. As such, the control of the metal NP is important for the design of the photophysical property of the molecule. Figure 5.6 shows the optimization history and deviations of the target property and field fluence of the designed system with the largest objective function. All the data of the optimization for the designed systems are shown in Figures 5.S9 and 5.S10. The optimization histories suggest that the objective function is relatively smooth as a function of the participation coefficients.

Table 5.3. Results of the design of both the optimal molecule and incident field on the various metal NPs[a)]

Metal NP		Optimal molecule			Designed properties		
Nature	Shape	Species	Conformation	Distance (Å)	J	P	Flunece (a.u.)
Ag	Cube	3tBu-MQ	*xy*	8	0.575	0.726	1.51×10^{-3}
	Ellipsoid	EQ	*xy*	8	0.652	0.895	2.42×10^{-3}
	Rod	3tBu-MQ	*xy*	5	0.582	0.873	2.92×10^{-3}
	Sphere	EQ	*xy*	5	0.675	0.881	2.06×10^{-3}
Au	Cube	3tBu-MQ	*xy*	5	0.647	0.917	2.70×10^{-3}
	Rod	EQ	*xy*	5	0.557	0.874	3.17×10^{-3}
	Sphere	MQ	*xy*	5	0.394	0.757	3.63×10^{-3}

[a)]In the design on the gold ellipsoidal NP, the requirements for the design (equation (13)) were not fulfilled with γ = 1.05, 1.20, 1.50, and 2.00, and the designed system was not obtained in the five trials with the randomized initial participation coefficients.

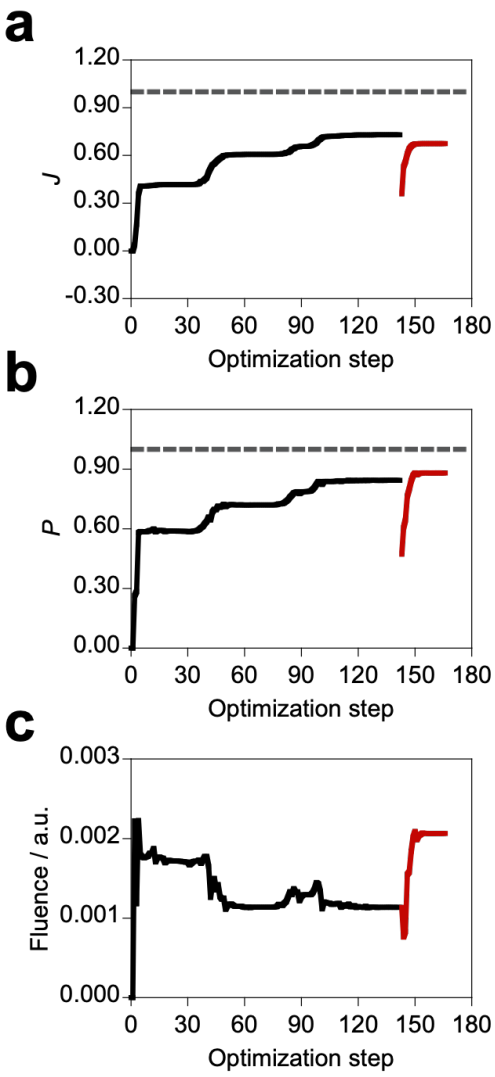

Figure 5.6. Optimization history of the objective function in both the optimal molecule and incident field design, along with variations of population of the target state and total fluence of the incident field. The design was performed on the silver spherical NPs, and the EQ molecule possessing the *xy* conformation at 5 Å distance from the silver spherical NP surface (Figure 5.S5(d)) and the incident electric field (Figure 5.S7(d)) were obtained. The red lines are of the design of optimal incident field for the optimal molecule. The gray dashed lines denote the value of 1.00.

5.4. Summary

In summary, we proposed an inverse design method of optimal molecule near the metal NP and incident electric field based on the time-dependent QM/BEM approach. In this method, the molecule is designed for the molecular species and spatial arrangements with respect to the NP. The design of each component and both of them was performed to maximize the population of the target excited state. MQ and its derivatives were examined as the candidate molecules to design the substituents. For the molecule, the design successfully proposed the optimal molecule whose target state population is the largest in the proximity of the silver spherical NP under the illumination of the electric pulse of the Gaussian sinusoidal wave. It was found that the optimal incident field can achieve the almost perfect population transfer to the target excited state in the molecule near the metal NP. The design of both the molecule and incident electric filed of the molecule−NP systems was successfully demonstrated. It was shown that the design and precise control of the molecule−NP systems and the incident field are important to realize the desired photophysical properties. The present inverse design approach gives the basis for the design of molecule−NP systems and incident fields and for the manipulation photochemical events.

Supporting Information

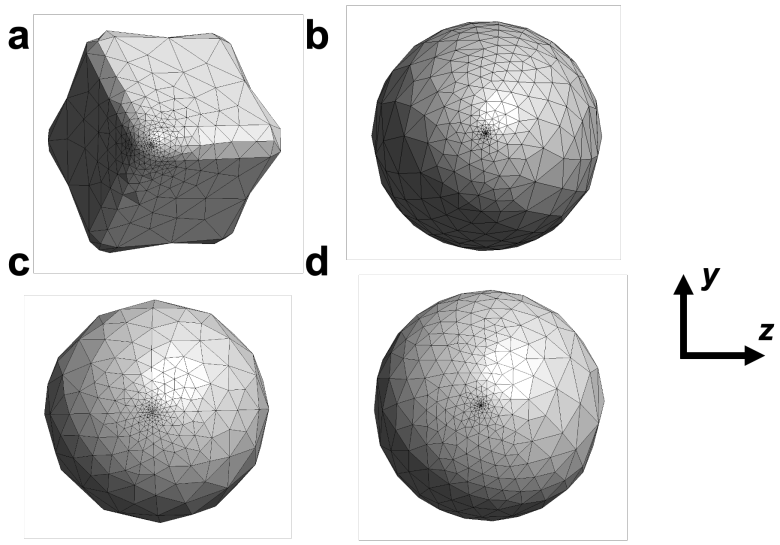

Figure 5.S1. Candidate metal NPs of (a) cubic, (b) ellipsoidal, (c) rod, and (d) spherical shapes. The view from the *x* axis.

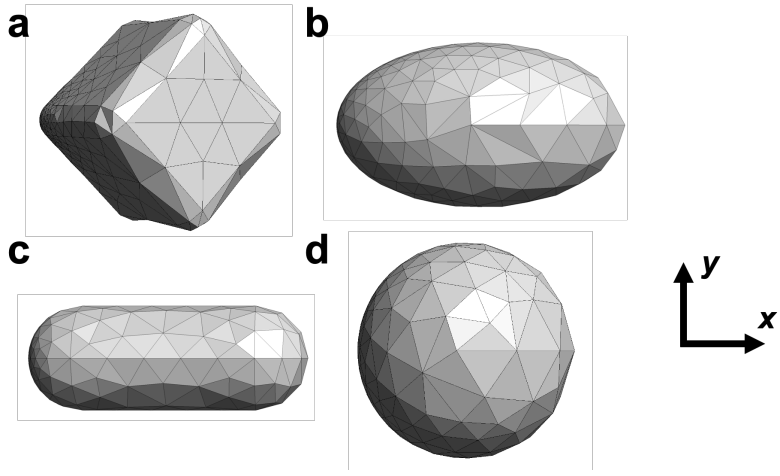

Figure 5.S2. Candidate metal NPs of (a) cubic, (b) ellipsoidal, (c) rod, and (d) spherical shapes. The view from the *z* axis.

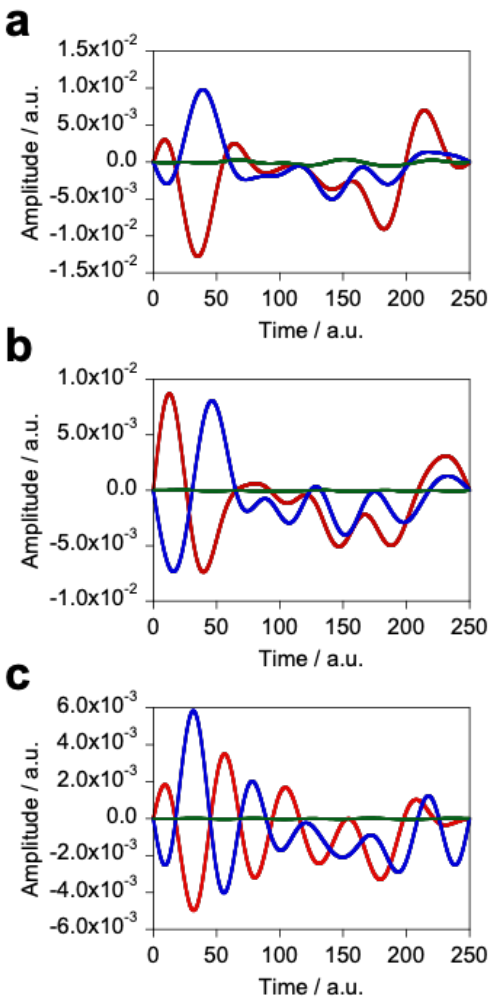

Figure 5.S3. Time profiles of the optimal incident fields designed with the penalty factor α of (a) 1, (b) 10, or (c) 100 for the field fluence.

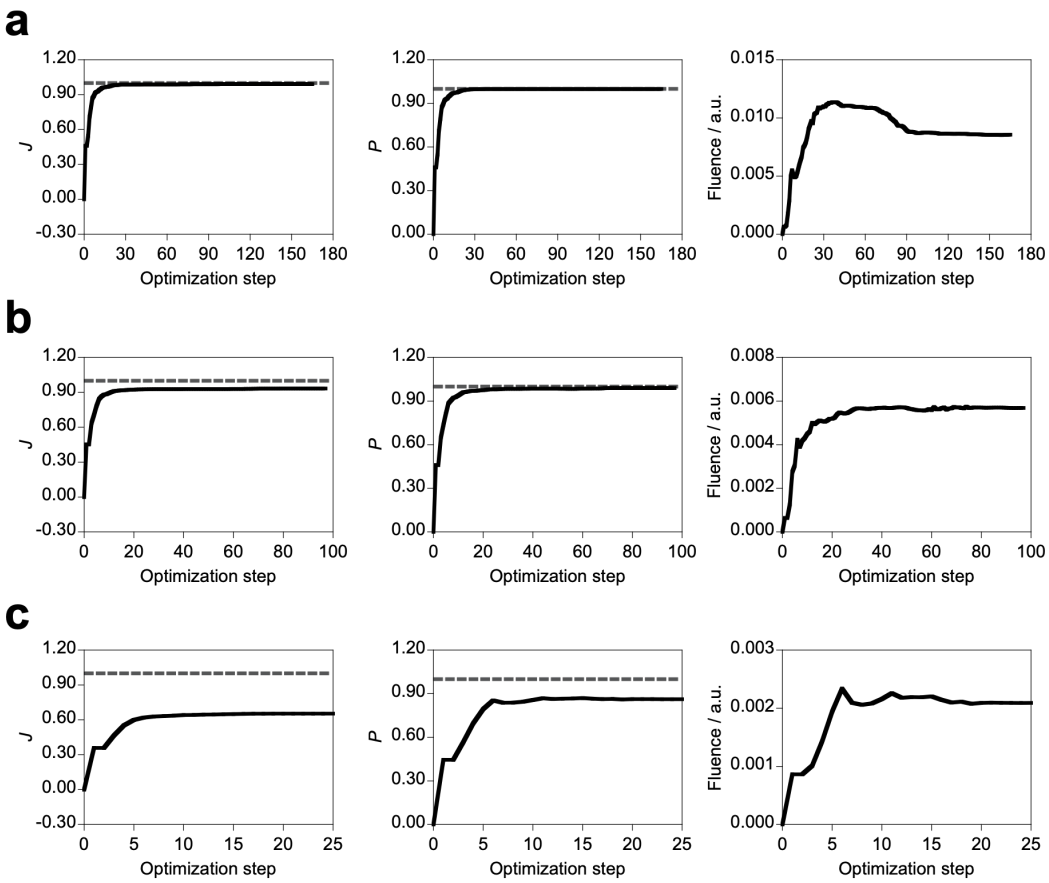

Figure 5.S4. Optimization histories of the objective function in the design of the optimal incident field with the different penalty factors α of (a) 1, (b) 10, and (c) 100 for the field fluence, along with variations of population of the target state and total fluence of the incident field. The gray dashed lines denote the value of 1.00.

Table 5.S1. Penalty factor γ used in the design of both the molecule and incident field on the various metal NPs

NP shape	Metal nature	
	Ag	Au
Cube	1.05	1.05
Ellipsoid	1.05	-
Rod	1.20	1.05
Sphere	1.20	1.20

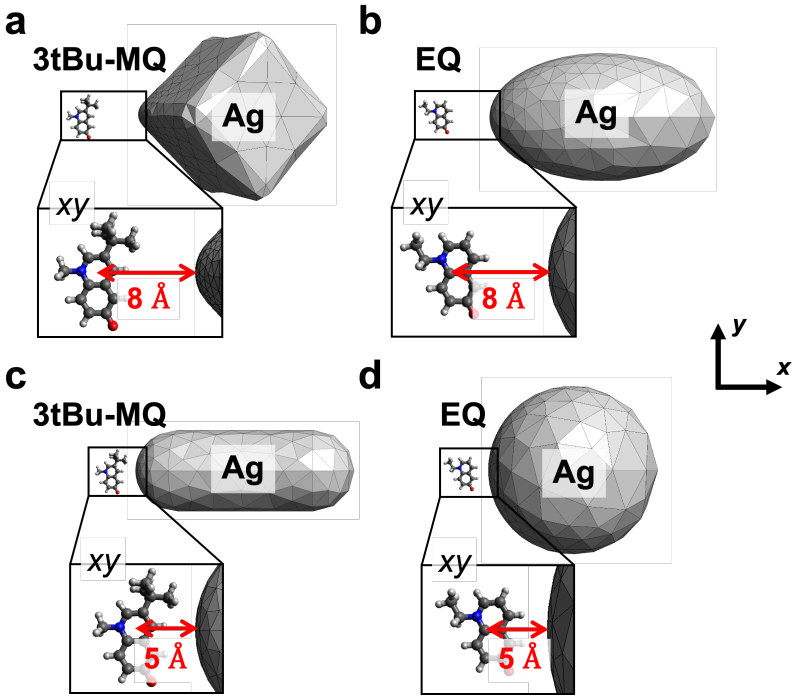

Figure 5.S5. Schematic representations of the designed molecule + metal NP systems obtained in the design of both the molecule and incident electric field. The design was performed on the silver NPs with (a) cubic, (b) ellipsoidal, (c) rod, and (d) spherical shapes. Drawing out of scale.

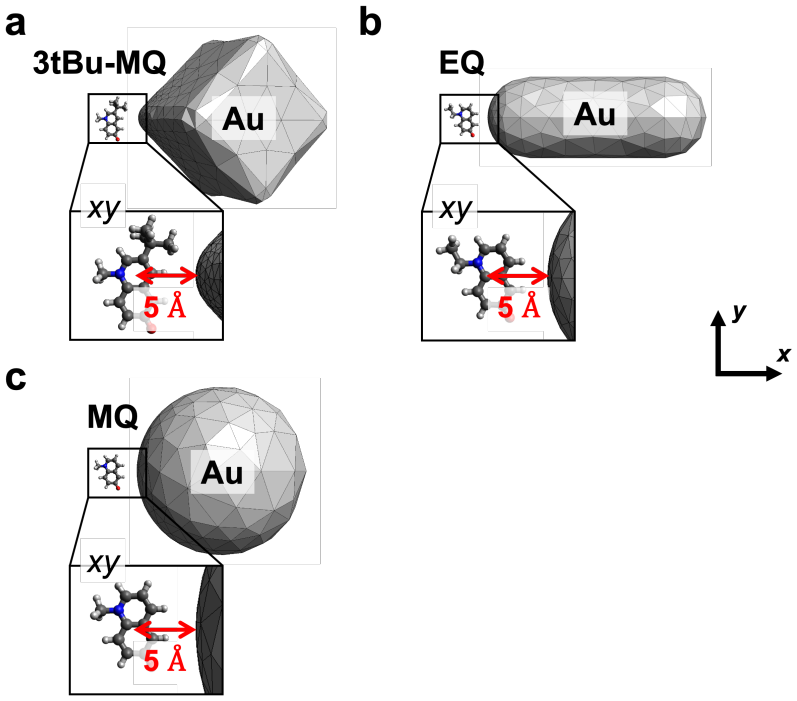

Figure 5.S6. Schematic representations of the designed molecule + metal NP systems obtained in the design of both the molecule and incident electric field. The design was performed on the gold NPs with (a) cubic, (b) rod, and (c) spherical shapes. Drawing out of scale.

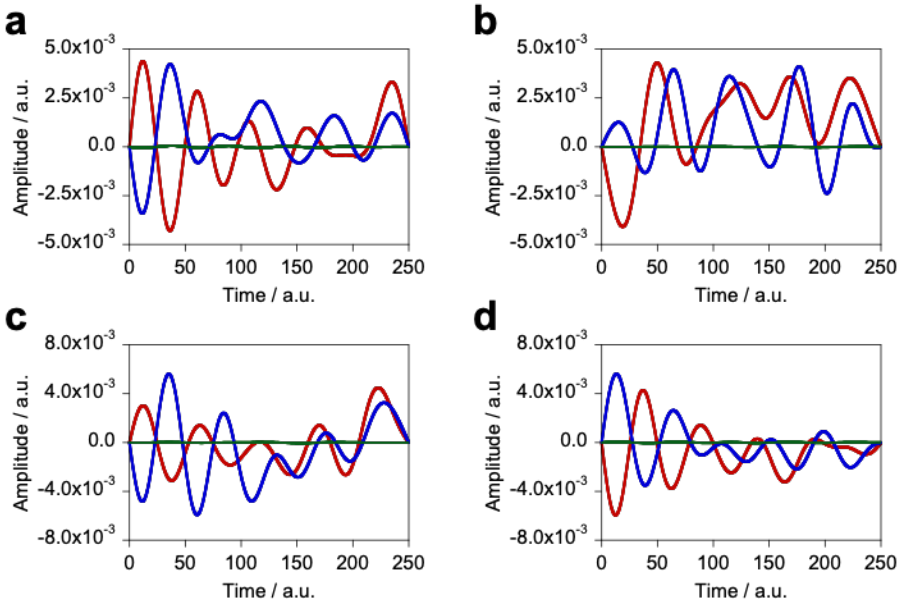

Figure 5.S7. Time profiles of the optimal incident fields obtained in the design of both the molecule and incident electric field. The design was performed on the silver NPs with (a) cubic, (b) ellipsoidal, (c) rod, and (d) spherical shapes. The red, blue, and green lines are the *x*, *y*, and *z* components, respectively.

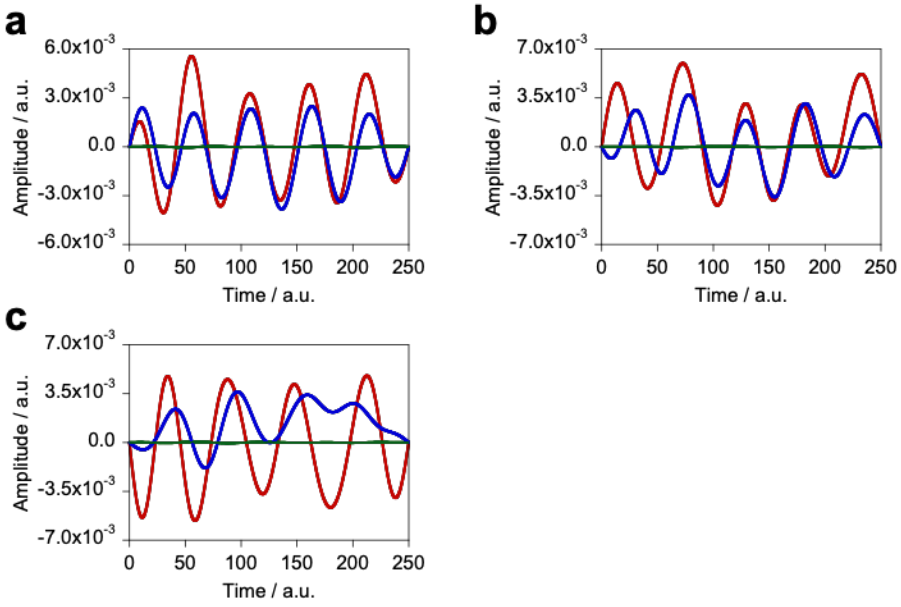

Figure 5.S8. Time profiles of the optimal incident fields obtained in the design of both the molecule and incident electric field. The design was performed on the gold NPs with (a) cubic, (b) rod, and (c) spherical shapes. The red, blue, and green lines are the *x*, *y*, and *z* components, respectively.

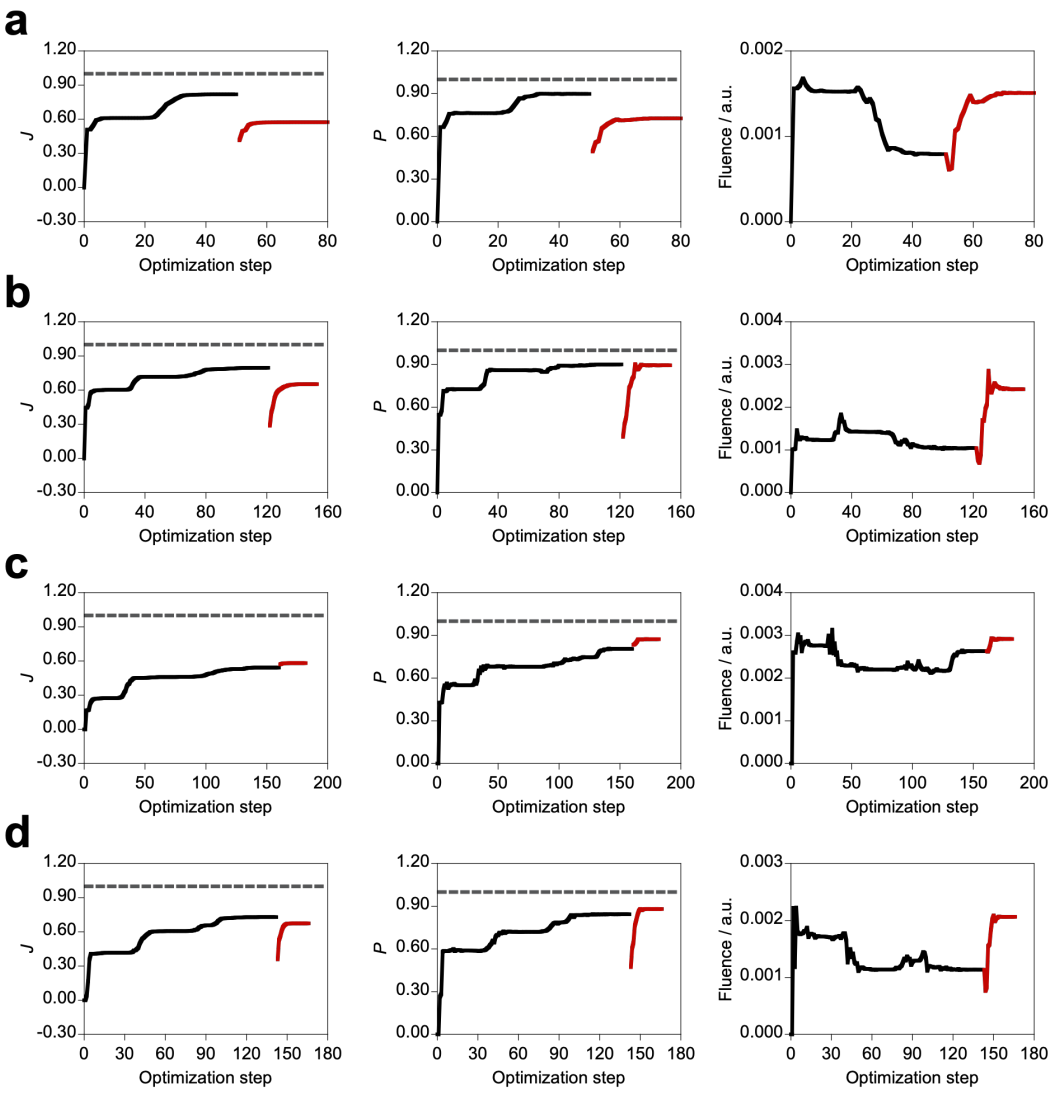

Figure 5.S9. Optimization histories of the objective function in both the optimal molecule and incident field design, along with variations of population of the target state and total fluence of the incident field. The design was performed on the silver NPs with (a) cubic, (b) ellipsoidal, (c) rod, and (d) spherical shapes. The red lines are of the design of the optimal incident field for the optimal molecule. The gray dashed lines denote the value of 1.00.

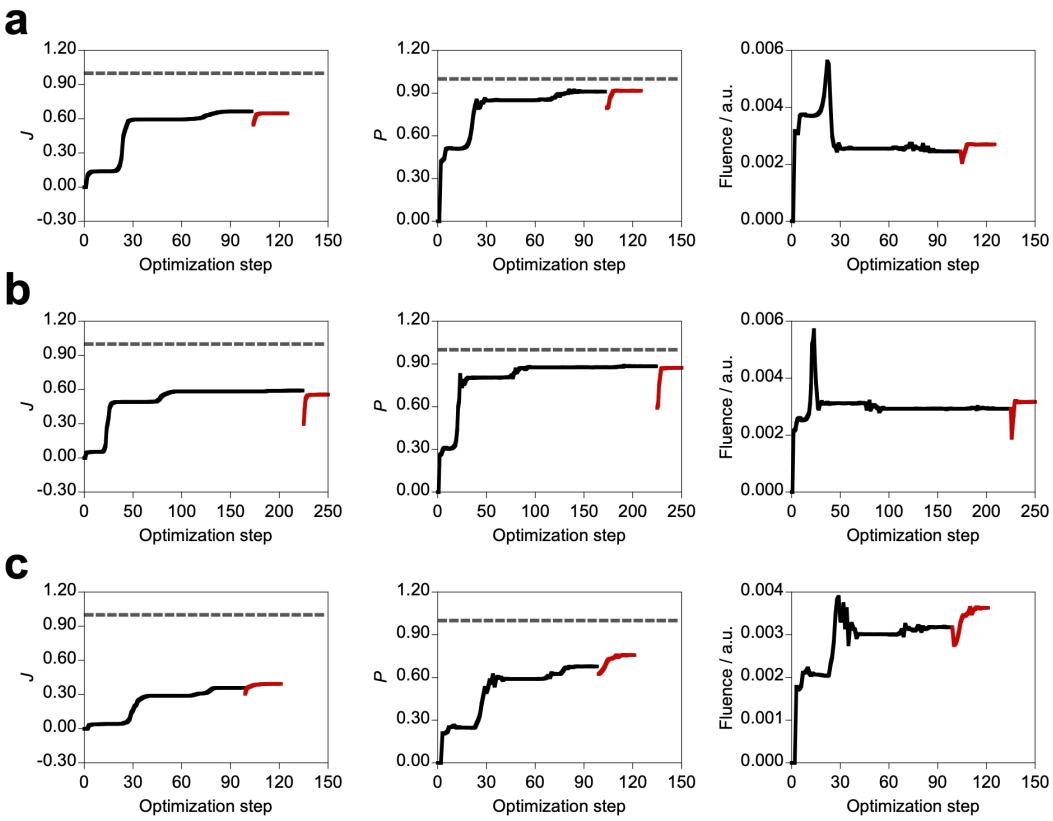

Figure 5.S10. Optimization histories of the objective function in both the optimal molecule and incident field design, along with variations of population of the target state and total fluence of the incident field. The design was performed on the gold NPs with (a) cubic, (b) rod, and (c) spherical shapes. The red lines are of the design of the optimal incident field for the optimal molecule. The gray dashed lines denote the value of 1.00.

References

[1] S. Schlucker, *Angew. Chem. Int. Ed.*, **2014**, *53*, 4756–4795.

[2] A. B. Zrimsek, N. Chiang, M. Mattei, S. Zaleski, M. O. McAnally, C. T. Chapman, A. I. Henry, G. C. Schatz, R. P. Van Duyne, *Chem. Rev.*, **2017**, *117*, 7583–7613.

[3] E. Dulkeith, M. Ringler, T. A. Klar, J. Feldmann, A. Munoz Javier, W. J. Parak, *Nano. Lett.*, **2005**, *5*, 585–589.

[4] J. F. Li, C. Y. Li, R. F. Aroca, *Chem. Soc. Rev.*, **2017**, *46*, 3962–3979.

[5] S. Linic, U. Aslam, C. Boerigter, M. Morabito, *Nat. Mater.*, **2015**, *14*, 567–576.

[6] C. Zhan, X.-J. Chen, J. Yi, J.-F. Li, D.-Y. Wu, Z.-Q. Tian, *Nat. Rev. Chem.*, **2018**, *2*, 216–230.

[7] M. M. Hann, T. I. Oprea, *Curr. Opin. Chem. Biol.*, **2004**, *8*, 255–263.

[8] R. A. Sperling, W. J. Parak, *Philos. Trans. A Math. Phys. Eng. Sci.*, **2010**, *368*, 1333–1383.

[9] M. Swierczewska, S. Lee, X. Chen, *Phys. Chem. Chem. Phys.*, **2011**, *13*, 9929–9941.

[10] S. M. Risser, D. N. Beratan, S. R. Marder, *J. Am. Chem. Soc.*, **1993**, *115*, 7719–7728.

[11] C. Kuhn, D. N. Beratan, *J. Phys. Chem.*, **1996**, *100*, 10595–10599.

[12] O. A. von Lilienfeld, R. D. Lins, U. Rothlisberger, *Phys. Rev. Lett.*, **2005**, *95*, 153002.

[13] A. Zunger, *Nat. Rev. Chem.*, **2018**, *2*, 0121.

[14] O. A. von Lilienfeld, *Int. J. Quantum Chem.*, **2013**, *113*, 1676–1689.

[15] T. Weymuth, M. Reiher, *Int. J. Quantum Chem.*, **2014**, *114*, 823–837.

[16] B. Sanchez-Lengeling, A. Aspuru-Guzik, *Science*, **2018**, *361*, 360–365.

[17] J. G. Freeze, H. R. Kelly, V. S. Batista, *Chem. Rev.*, **2019**, *119*, 6595–6612.

[18] M. Foscato, V. R. Jensen, *ACS Catalysis*, **2020**, *10*, 2354–2377.

[19] O. A. von Lilienfeld, M. E. Tuckerman, *J. Chem. Phys.*, **2006**, *125*, 154104.

[20] G. F. von Rudorff, O. A. von Lilienfeld, *Phys. Rev. Res.*, **2020**, *2*, 023220.

[21] M. Wang, X. Hu, D. N. Beratan, W. Yang, *J. Am. Chem. Soc.*, **2006**, *128*, 3228–3232.

[22] D. Xiao, W. Yang, D. N. Beratan, *J. Chem. Phys.*, **2008**, *129*, 044106.

[23] T. Shiraogawa, M. Ehara, *J. Phys. Chem. C*, **2020**, *124*, 13329–13337.

[24] C. Brif, R. Chakrabarti, H. Rabitz, *New J. Phys.*, **2010**, *12*, 075008.

[25] S. Malola, L. Lehtovaara, J. Enkovaara, H. Hakkinen, *ACS Nano*, **2013**, *7*, 10263–10270.

[26] K. Iida, M. Noda, K. Ishimura, K. Nobusada, *J. Phys. Chem. A*, **2014**, *118*, 11317–11322.

[27] S. Corni, J. Tomasi, *J. Chem. Phys.*, **2001**, *114*, 3739–3751.

[28] B. Mennucci, S. Corni, *Nat. Rev. Chem.*, **2019**, *3*, 315–330.

[29] E. Coccia, J. Fregoni, C. A. Guido, M. Marsili, S. Pipolo, S. Corni, *J. Chem. Phys.*, **2020**, *153*, 200901.

[30] J. Tomasi, B. Mennucci, R. Cammi, *Chem. Rev.*, **2005**, *105*, 2999–3093.

[31] S. Corni, S. Pipolo, R. Cammi, *J. Phys. Chem. A*, **2015**, *119*, 5405–5416.

[32] S. Pipolo, S. Corni, *J. Phys. Chem. C*, **2016**, *120*, 28774–28781.

[33] E. Coccia, S. Corni, *J. Chem. Phys.*, **2019**, *151*, 044703.

[34] G. Dall'Osto, G. Gil, S. Pipolo, S. Corni, *J. Chem. Phys.*, **2020**, *153*, 184114.

[35] Y. E. Lee, O. D. Miller, M. T. Homer Reid, S. G. Johnson, N. X. Fang, *Opt. Express*, **2017**, *25*, 6757–6766.

[36] E. Cancès, B. Mennucci, J. Tomasi, *J. Chem. Phys.*, **1997**, *107*, 3032.

[37] D. Castaldo, M. Rosa, S. Corni, *arXiv:2007.00368*, 2020.

[38] J. L. Perez Lustres, S. A. Kovalenko, M. Mosquera, T. Senyushkina, W. Flasche, N. P. Ernsting, *Angew. Chem. Int. Ed.*, **2005**, *44*, 5635–5639.

[39] T. Klamroth, *J. Chem. Phys.*, **2006**, *124*, 144310.

[40] M. Rosa, G. Gil, S. Corni, R. Cammi, *J. Chem. Phys.*, **2019**, *151*, 194109.

[41] M. Gerecke, C. Richter, M. Quick, I. N. Ioffe, R. Mahrwald, S. A. Kovalenko, N. P. Ernsting, *J. Phys. Chem. B*, **2017**, *121*, 9631–9638.

[42] E. Heid, C. Schroder, *J. Phys. Chem. B*, **2017**, *121*, 9639–9646.

[43] C. Geuzaine, J.-F. Remacle, *Int. J. Numer. Methods Eng.*, **2009**, *79*, 1309–1331.

[44] P. B. Johnson, R. W. Christy, *Phys. Rev. B*, **1972**, *6*, 4370–4379.

[45] A. D. Rakic, A. B. Djurisic, J. M. Elazar, M. L. Majewski, *Appl. Opt.*, **1998**, *37*, 5271–5283.

[46] M. J. Frisch, G. W. Trucks, H. B. Schlegel, G. E. Scuseria, M. A. Robb, J. R. Cheeseman, G. Scalmani, V. Barone, G. A. Petersson, H. Nakatsuji, X. Li, M. Caricato, A. V. Marenich, J. Bloino, B. G. Janesko, R. Gomperts, B. Mennucci, H. P. Hratchian, J. V. Ortiz, A. F. Izmaylov, J. L. Sonnenberg, Williams, F. Ding, F. Lipparini, F. Egidi, J. Goings, B. Peng, A. Petrone, T. Henderson, D. Ranasinghe, V. G. Zakrzewski, J. Gao, N.

Rega, G. Zheng, W. Liang, M. Hada, M. Ehara, K. Toyota, R. Fukuda, J. Hasegawa, M. Ishida, T. Nakajima, Y. Honda, O. Kitao, H. Nakai, T. Vreven, K. Throssell, J. A. Montgomery, Jr., J. E. Peralta, F. Ogliaro, M. J. Bearpark, J. J. Heyd, E. N. Brothers, K. N. Kudin, V. N. Staroverov, T. A. Keith, R. Kobayashi, J. Normand, K. Raghavachari, A. P. Rendell, J. C. Burant, S. S. Iyengar, J. Tomasi, M. Cossi, J. M. Millam, M. Klene, C. Adamo, R. Cammi, J. W. Ochterski, R. L. Martin, K. Morokuma, O. Farkas, J. B. Foresman, D. J. Fox., *Gaussian 16*, Rev. B.01; Gaussian, Inc.: Wallingford, CT, 2016.

[47] M. W. Schmidt, K. K. Baldridge, J. A. Boatz, S. T. Elbert, M. S. Gordon, J. H. Jensen, S. Koseki, N. Matsunaga, K. A. Nguyen, S. Su, T. L. Windus, M. Dupuis, J. A. Montgomery, Jr., *J. Comput. Chem.*, **1993**, *14*, 1347–1363.

[48] M. S. Gordon, M. Schmidt. In Theory and Applications of Computational Chemistry: the first forty years; C. Dykstra, G. Frenking, K. Kim, G. E. Scuseria, Eds.; Elsevier: Amsterdam, 2005; pp 1167−1189.

[49] R. H. Byrd, P. H. Lu, J. Nocedal, C. Y. Zhu, *SIAM J. Sci. Comput.*, **1995**, *16*, 1190–1208.

[50] C. Zhu, R. H. Byrd, J. Nocedal, *ACM Trans. Math. Softw.*, **1997**, *23*, 550–560.

[51] J. L. Morales, J. Nocedal, *ACM Trans. Math. Softw.*, **2011**, *38*.

[52] W. Zhu, J. Botina, H. Rabitz, *J. Chem. Phys*, **1998**, *108*, 1953–1963.

Chapter 6

Final Remarks

The main purpose of this thesis is to investigate theoretical and computational design approaches of photofunctional composite systems containing molecules. This thesis is focused on the design of the photofunctional systems because of their designability and the strong dependence of the photofunctions on their structure and constituents. The proposed design approaches were developed within the theoretical descriptions of the system based on the design variables.

For molecular aggregates composed of organic chromophores, direct and inverse design approaches were investigated based on the Frenkel exciton model. To perform the direct design, the author developed a Frenkel-exciton decomposition analysis (FEDA) method (Chapter 2) which reveals contributions from the design variables (chromophores) to the optical spectra of the whole system. Based on the analysis results, the modification guidelines of the multichromophoric system for improving the photofunctions were proposed (Chapter 3). This strategy only requires the calculation and analysis of a reference system, and the applicability is limited to the modification. Moreover, this approach can not propose the real system without *a priori* knowledge of the design variables. The inverse design predicts optimal systems with the desired photophysical properties in the predefined chemical space. The inverse design methods of molecular aggregates (Chapter 4) and molecule−metal nanostructure systems (Chapter 5) were proposed. These approaches continuously interpolate the chemical space within the theoretical descriptions, allowing the design in a predictive manner by the continuous optimization-based search.

In conclusion, in this thesis, the design approaches of photofunctional composite

systems containing molecules were studied. The performance of these approaches and the photophysical properties of the designed systems were investigated. The present approaches, with their own limitations, can be utilized to help guiding developments of photofunctional systems and materials and be the basis for further developments of the theoretical and computational design methodologies.

List of Publications

Chapter 2. "Frenkel-Exciton Decomposition Analysis of Circular Dichroism and Circularly Polarized Luminescence for Multichromophoric Systems,"
T. Shiraogawa, M. Ehara, S. Jurinovich, L. Cupellini, B. Mennucci,
J. Comput. Chem. **2018**, *39*, 931–935.

Chapter 3. "Theoretical Study on the Optical Properties of Multichromophoric Systems Based on an Exciton Approach: Modification Guidelines,"
T. Shiraogawa, M. Ehara,
ChemPhotoChem **2019**, *3*, 707–718.

Chapter 4. "Theoretical Design of Photofunctional Molecular Aggregates for Optical Properties: An Inverse Design Approach,"
T. Shiraogawa, M. Ehara,
J. Phys. Chem. C **2020**, *124*, 13329–13337.

The other publications not included in the thesis:

(1) "Photophysical Properties of Fluorescent Imaging Biological Probes of Nucleic Acids: SAC-CI and TD-DFT Study,"
T. Shiraogawa, G. Candel, R. Fukuda, I. Ciofini, C. Adamo, A. Okamoto, M. Ehara,
J. Comput. Chem. **2019**, *40*, 127–134.

(2) "Mechanistic Studies on Photoinduced Catalytic Olefin Migration Reactions at the Pd(II) Centers of a Porous Crystal, Metal-Macrocycle Framework,"
H. Yonezawa, T. Shiraogawa, M. Han, S. Tashiro, M. Ehara, M. Shionoya,
Chem. Asian J. **2021**, *16*, 202−206.

(3) “Preferential Photoreaction in a Porous Crystal, Metal–Macrocycle Framework: Pd^{II}-Mediated Olefin Migration over [2+2] Cycloaddition,”
H. Yonezawa, S. Tashiro, T. Shiraogawa, M. Ehara, R. Shimada, T. Ozawa, M. Shionoya,
J. Am. Chem. Soc. **2018**, *140*, 16610−16614.

(4) “The Direct Observation of the Doorway $^1n\pi^*$ State of Methylcinnamate and Hydrogen-Bonding Effects on the Photochemistry of Cinnamate-Based Sunscreens,”
S. Kinoshita, Y. Inokuchi, Y. Onitsuka, H. Kohguchi, N. Akai, T. Shiraogawa, M. Ehara, K. Yamazaki, Y. Harabuchi, S. Maeda, T. Ebata,
Phys. Chem. Chem. Phys. **2019**, *21*, 19755–19763.

(5) “Light-driven Molecular Switch for Reconfigurable Spin Filters,”
M. Suda, Y, Thathong, V. Promarak, H. Yokogawa, H. Kojima, M. Nakamura, T. Shiraogawa, M. Ehara, H. M. Yamamoto,
Nat. Commun. **2019**, *10*, 1−10.

(6) “Different Photoisomerization Routes Found in the Structural Isomers of Hydroxy Methylcinnamate,”
S. Kinoshita, Y. Miyazaki, M. Sumida, Y. Onitsuka, H. Kohguchi, Y. Inokuchi, N. Akai, T. Shiraogawa, M. Ehara, K. Yamazaki, Y. Harabuchi, S. Maeda, T. Taketsugu, T. Ebata,
Phys. Chem. Chem. Phys. **2018**, *20*, 17582–17598.

Acknowledgements

My heartfelt appreciation goes to my supervisor, Prof. Masahiro Ehara for his patient guidance, valuable discussions, and constant encouragement. Moreover, thanks to his coordination, the author was able to collaborate with many research groups, which broadened the author's horizons.

He would like to thank Drs. Kazuya Ishimura, Hiroaki Nishizawa, Yoshiharu Mori, Soichi Ito, Pei Zhao, Ryo Inoue, Archana Velloth, and Yuki Kanazawa for valuable discussions on computational chemistry. He is also grateful to Mr. Masataka Yamauchi for a number of discussions on theoretical and computational chemistry and for teaching the author programming techniques.

The author had many opportunities for valuable collaborations with other research groups. He is obliged to Prof. Benedetta Mennucci and Drs. Sandro Jurinovich and Lorenzo Cupellini for providing their computer code and insightful comments and suggestions in research presented in Chapter 2. The author wishes to express his appreciation to Profs. Stefano Corni and Roberto Cammi and Miss Giulia Dall'Osto for providing their computer code, fruitful discussions and suggestions, coding, and calculations in a study presented in Chapter 5. For studies not presented in this thesis, the author would like to thank the collaborators; Profs. Adamo Carlo and Akimitsu Okamoto, Drs. Ciofini Iralia and Ryoichi Fukuda, and Miss Gaële Candel for collaborative research on biological probes; Prof. Mitsuhiko Shionoya and Drs. Shohei Tashiro and Hirotaka Yonezawa for collaborative research on pseudo-heterogeneous catalysis; Prof. Takayuki

Ebata, Dr. Yu Harabuchi, and Mr. Shin-nosuke Kinoshita for collaborative research on photoisomerization routes of cinnamates; Prof. Hiroshi Yamamoto and Dr. Masayuki Suda for collaborative research on reconfigurable spin filters.

Finally, the author expresses his sincere gratitude to his parents, Mr. Yoshitaka Shiraogawa and Mrs. Yoko Shiraogawa, for their continuous understanding and financial supports. He also would like to thank the Japan Society for the Promotion of Science for financial supports and research fund.